VILNIUS UNIVERSITY

CENTER FOR PHYSICAL SCIENCES AND TECHNOLOGY

VYTENIS PRANCULIS

CHARGE TRANSFER DYNAMICS IN BULK-HETEROJUNCTION ORGANIC SOLAR CELLS

Doctoral dissertation

Physical sciences, physics (02P)

Vilnius, 2017

Doctoral dissertation was prepared at the Center for physical sciences and technology in 2012-2016.

Scientific supervisor – prof. habil. dr. Vidmantas Gulbinas (Center for physical sciences and technology, physical sciences, physics – 02P).

VILNIAUS UNIVERSITETAS

NACIONALINIS FIZINIŲ IR TECHNOLOGIJOS MOKSLŲ CENTRAS

VYTENIS PRANCULIS

KRŪVIO PERNAŠOS DINAMIKA ORGANINIUOSE TŪRINĖS HETEROSANDŪROS SAULĖS ELEMENTUOSE

Daktaro disertacija

Fiziniai mokslai, fizika (02P)

Vilnius, 2017

Disertacija rengta 2012-2016 metais Fizinių ir technologijos mokslų centre.

Mokslinis vadovas – prof. habil. dr. Vidmantas Gulbinas (Fizinių ir technologijos mokslų centras, fiziniai mokslai, fizika – 02P).

Table of Contents

Abstract

The work presented in this thesis focuses on the extraction of charges photogenerated in organic bulk-heterojunction solar cells. Charge migration dynamics were observed experimentally on a vast time range – from sub-ps to ms – as well as in a variety of devices in order to form a comprehensive view.

Role of coherence and delocalization on charge transfer at donor-acceptor interface and the initial electron migration was analyzed by measuring the electric field drop in the solar cell after the ultrafast photoexcitation. Time-resolved electric field induced second harmonic generation (TREFISH) method was used to obtain sub-ps time resolution. Experimental data was then used as a basis for the Stochastic Schrödinger Equation (SSE) simulations, which indicate that even a relatively weak coupling between PCBM molecules is sufficient to facilitate electron delocalization and efficient charge separation.

Subsequent electron and hole migration was investigated using TREFISH method combined with integrated photocurrent (IPC) measurements on a vast pool of devices. Experimental results over different donor-acceptor ratio devices in combination with time dependent mobility modelling and Monte-Carlo calculations enabled the separation of extraction of electrons and holes. It was found that charge extraction strongly depends on the fraction of the corresponding material in the blend. Balanced carrier mobility did not ensure the most efficient extraction. Rather, fast motion of electrons was found to be essential for efficient charge carrier separation helping to avoid geminate recombination. Mobility of the photogenerated charges was observed to decrease over orders of magnitude in the time span from their generation to extraction. This drop in mobility was found to originate from carrier relaxation within their respective density of states (DOS). Morphology optimization using the solvent additive 1,8-diiodooctane (DIO) was found to double the charge pair separation efficiency and the short-circuit current. Carrier extraction at low internal electric field was slightly faster from the cells prepared with DIO, which can reduce recombination losses and enhance fill factor.

1. Introduction

1.1. Solar power and photovoltaic effect

The Sun is unarguably the most important power source for life on earth. Energy available to us from non-solar sources, namely tidal, geothermal and nuclear dwarf in comparison to 162 PW that our planet continuously receives via solar radiation.[1] Depending on the atmospheric conditions, part of the incident sunlight is reflected to space or scattered throughout the atmosphere yet on average 86 PW reach the surface. It then should come as no surprise that direct solar radiation conversion to electricity is considered as one of the best approach to fulfill global electricity needs of several TW. Photovoltaic technology not only has the potential to quench our ever-growing thirst for electricity but can do so without any moving parts, long-term radiation contamination or environmental emissions.[2]

The basic process of generating electricity from incident light in a solar cell is known as photovoltaic effect. When photons are absorbed by a photovoltaic cell, which contains a semiconducting material, the energy from the photon is transferred to an electron in an atom of the solar cell. The energized electron is then able to escape its bond with the atom and generates an electric current. This also leaves behind a hole. The collection of light-generated carriers, however, does not by itself give rise to power generation. In order to generate power, a

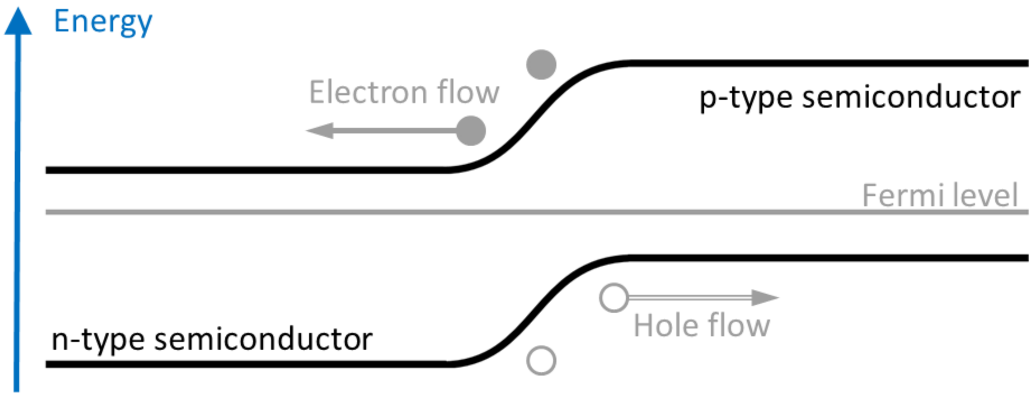

Figure 1.1 Formation of a potential barrier in a p-n junction due to equalization of Fermi levels.

voltage must be generated as well as a current. If n- and p-type semiconductors are brought together, a p-n junction with a potential barrier is formed due to the thermodynamic principle which requires that the average energy of the carriers (the Fermi level) be the same in the two materials (Figure 1.1). Photogenerated free electrons then can cross the junction more easily in one direction (from p-type to n-type) than in the other, giving one side of the junction a negative charge and, therefore, a negative voltage with respect to the other side. The same is also true for holes. The photovoltaic effect can continue to provide voltage and current as long as light continues to fall on the two materials.

Discovery of the photovoltaic effect in 1839 by E. Becquerel marked the slow start of solar cell research. First functioning device was presented only in 1877 when William Grylls Adams along with his student Richard Day discovered that selenium, when exposed to light, produced electricity.[3] Although selenium cells were far from efficient they demonstrated the proof-of-concept that light could be converted into electricity.

1954 saw a new type of solar cell – silicon. In May of that year Journal of Applied Physics issued an article by Daryl Chapin, Calvin Fuller and Gerald Pearson from the Bell Labs titled *"A New Silicon p-n Junction Photocell for Converting Solar Radiation into Electrical Power"* where the authors reported 6% power conversion efficiency.[4] The New York Times praised it as a device that *"may mark the beginning of a new era, leading eventually to the realization of one of mankind's most cherished dreams – the harnessing of the almost limitless energy of the sun for the uses of civilization"*.[5]

1.2. Solar cell types

Since these first attempts to harness the energy of the sun, the field of photovoltaics saw a mass of researchers working on the problem of increasing the power conversion efficiency of solar cells. A vast number of researchers not only ensured steady increase in device efficiency. Multiple types of solar cells emerged as a result of differing approaches. One can crudely divide the resulting technologies into five categories, namely crystalline silicon, GaAs, multi-junction, thin film and organic.

Current PV production is dominated by single-junction solar cells based on silicon wafers including mono-crystalline (c-Si) and poly-crystalline silicon (pc-Si). These types of single-junction, silicon-wafer devices are now commonly referred to as the first-generation (1G) technology and comprise more than 80% of the world PV industry.[6] Originally built using single-crystal wafer silicon (c-Si) and processing technology from the integrated circuit (IC) manufacturing, it is clear that 1G silicon PV benefited greatly from its symbiosis with the IC industry which provided the materials, processing know-how, and manufacturing tools necessary to allow a rapid move to large-scale production. In the beginning of the “semiconductor era” (after the discovery of the bipolar transistor in 1948), the rapid progress of silicon technology echoed in the efficiency of silicon solar cells as well – boosting it up to 15%. In the second stage (1970s), 17% efficiency Si solar cells were fabricated due to achievements in microelectronics (e.g., photolithography). The most significant results have been obtained in the third (1980s) and fourth (2000+) stages when Si cell efficiencies close to 25% have been achieved. These efficiencies were due to improved contact and surface passivation of the cell along the front and rear surfaces as well as an improved understanding of the significant role of light-trapping in Si devices. Optically, the inverted pyramids on the top surface significantly reduce reflection loss while the metal rear contact serves as an efficient reflector. Consequently, light is very effectively trapped within the cell.[7]

According to the Shockley-Queisser (S-Q) detailed-balance model, the limiting photovoltaic energy conversion efficiency for a single-junction solar cell is 33.7%, for an optimum semiconductor band gap of 1.34 eV (although there have been proposals on ways to overcome this limit).[8,9] Better efficiencies could be obtained with more efficient use of the solar spectrum. Combining two or more cells of different bandgaps into a multi-junction arrangement enables better utilization of photon energy over wide solar spectrum. In order to achieve increase in power, the cells should be current matched and joined in series – separated, for example, by a tunnel diode. An obvious way to increase the efficiency is to construct cells having ever bigger number of materials with different bandgaps. The best multi-junction cells have already reached an efficiency of more than 44%;[10] however, the technology is very expensive therefore today such solar cells are used mainly for space applications.

In terms of space power applications, the Si cells have too low efficiency and are susceptible to radiation damage. In the late 1980s, GaAs cells were used to fabricate flat-plate arrays due to high efficiencies and lower radiation-induced degradation than Si cells. GaAs single-junction solar cells with efficiencies of ≈25% were reported as early as 1990.[11] Unfortunately, little progress has been made since, with current research only being able to nudge it up to 27.6%.[12]

Half of the cost of first-generation photovoltaics is the cost of the 200..250 µm thick silicon wafer – a cost incurred for largely mechanical reasons since the majority of solar absorption occurs in the top few tens of microns and while 24% power conversion efficiency is possible to achieve in cells only 1 µm thick.[7] The obvious next step in the evolution of PV and reduced €/W is to remove the unnecessary material from the cost equation by using thin-film devices. Second-generation (2G) technologies are single-junction devices that aim to use less material while maintaining the efficiencies of 1G PV. 2G solar cells use amorphous-Si (a-Si), copper indium gallium selenide CIGS, CdTe or polycrystalline-Si (pc-Si) deposited on low-cost substrates such as glass or plastic via chemical vapor deposition. Research results from leading laboratories have provided ample evidence of the potential of thin-film PV with power conversion efficiencies reaching 16.2% for CdTe cells[13] and surpassing 20% for CIGS.[14,15] However, PV based on CdTe and CIGS has been slow to scale up. This is partly due to the gap between lab efficiencies and the best module efficiencies that are considerably lower as a result of unresolved issues relating to poor material reproducibility and uniformity over large areas.[16] Though perhaps the fundamental issue for both CdTe and CIGS technologies is the historical absence of symbiosis with a highly profitable IC industry.

1.3. Organic solar cells

As 2G technology progressively reduces the active material cost with thinner films, eventually even the low-cost substrate will become the cost limit and higher efficiency or even lower material and manufacturing cost will be needed to maintain the €/W cost-reduction trend. Enter the current research into third-generation (3G) devices. The term 3G encompass various emerging PV technologies, most of which are organic-based. Dye-sensitized cells (DSC) were the first to satisfy 3G criteria. Although, first introduced in 1991 with power conversion efficiency >7% DSC did not break efficiency records,[17] it was shown that low to medium purity materials and low cost manufacturing process can produce commercially valid €/W ratio despite lower efficiencies. Exploitation of almost limitless variations of organic compounds[18] led to an increase of DSC efficiencies up to 13%.[19]

All-polymer, polymer-fullerene and its derivatives (PCBM) and small molecule solar cells are often grouped together due to the similarity of device physics and processes taking place following an absorption of a photon. Unlike DSC, polymer based PV cells do not require an electrolyte for the charge transfer, thus avoiding the common problem of DSC "drying-out" and losing its efficiency over time. Such solar cells not only enjoy the vast pool of organic compounds for fine-tuning and optimization, but crucially enable all-solution processing with no vacuum steps and full roll-to-roll (R2R) processing – drastically driving down the price of manufacturing.[20] A promise of thin, flexible, lightweight, non-toxic and cheap photovoltaic technology attracted scores of research to the field leading to a steady growth of efficiency. At the moment, all three technologies produce solar cells with power conversion efficiencies of >10% [21–26] – a limit which is considered the €/W ratio suitable for commercial applications.

Leading drivers of increase of the performance of organic photovoltaic devices were development of new materials and refining of the production processes. Tailoring of the materials of the active layer and its morphology to increase the mobility of the charges hasn't been overlooked as well. However, recent breakthrough of perovskite solar cells not only demonstrates that disordered architecture is indeed a viable approach when designing organic-based solar cells but also reiterates that charge mobility is one of the key factors limiting their efficiency.

THE MAIN GOAL OF THIS THESIS IS THEREFORE TO INVESTIGATE CHARGE TRANSFER DYNAMICS IN BULK HETEROJUNCTION ORGANIC SOLAR CELLS IN DETAIL.

NOVELTY AND IMPORTANCE

The thesis aims to capture the complete image of charge migration and shed light on the possible hindrances. Initial charge transfer at the donor-acceptor interface was studied using TREFISH experimental technique and analyzed by performing Stochastic Schrödinger equation calculations. Results reveal that electron delocalization occurs on a femtosecond time scale, during which the electron wavefunction spreads in acceptor phase. Coherent propagation also shapes the initial electron-hole distance distribution. Subsequent migration was then observed using TREFISH and conventional transient photocurrent techniques and charge mobility was found to decrease over time. Carrier drift and extraction was also found to be strongly dependent on the stoichiometry of polymer-PCBM solar cells.

A more in depth analysis of the reasons behind charge carrier mobility time dependence was then performed using kinetic Monte Carlo modelling in combination with TREFISH and transient photocurrent measurements. Drop in charge mobility was found to originate from carrier relaxation within their respective density of states (DOS). Furthermore, a remarkable distribution of the photocurrent over energy was found, in which the most relaxed charge carriers in fact counteract the net photocurrent.

Influence of morphology on charge extraction kinetics was also investigated. It was found that short-circuit current of organic solar cells is determined by the separation of charge pairs into free carriers, which is strongly influenced by blend composition. This separation was found to be efficient in fullerene-rich blends where high electron mobility is observed during the first 10 ps after excitation. Morphology optimization using the solvent additive 1,8-diiodooctane (DIO) was found to double the charge pair separation efficiency and the short-circuit current. Carrier extraction at low internal electric field was slightly faster from the cells prepared with DIO, which can reduce recombination losses and enhance a fill factor.

Charge extraction and mobility dynamics have been experimentally observed over extensive time range from hundreds of fs up to several μs in multiple different types of organic solar cells. These results in combination with analytical and statistical modeling allowed for the separation of electron and hole motion in the bulk heterojunction organic solar cells. Such separation uncovers true behavior of both types of charge carriers in-situ, overcoming the drawbacks of most other methods that either produce averaged electron-hole mobility values or rely on idealized single-charge devices.

THE MAIN STATEMENTS

1. Balanced carrier extraction does not ensure the best solar energy conversion. Rather, fast motion of electrons is essential for efficient charge carrier separation preventing geminate recombination.
2. High non-equilibrium electron mobility determines their extraction rate which is orders of magnitude faster than that of holes in typical polymer-PCBM solar cells.
3. Increase in PTB7:$PC_{71}BM$ solar cell efficiencies achieved via morphology optimization using DIO agent originates from increased free carrier generation yield rather than their extraction efficiency.

LIST OF PUBLICATIONS THAT CONSTITUTE THE BASIS OF THIS THESIS

V. Abramavicius, V. Pranculis, A. Melianas, O. Inganäs, V. Gulbinas, D. Abramavicius, “Role of coherence and delocalization in photo-induced electron transfer at organic interfaces”, *Sci. Rep.*, **6**, 32914 (2016).

V. Pranculis, Y. Infahsaeng, Z. Tang, A. Devižis, D. A. Vithanage, C. S. Ponseca Jr., O. Inganäs, A. P. Yartsev, V. Gulbinas, V. Sundström, “Charge Carrier Generation and Transport in Different Stoichiometry APFO3:PC_{61}BM Solar Cells”, *J. Am. Chem. Soc.*, **136** (32), 11331–11338 (2014).

A. Melianas, V. Pranculis, A. Devižis, V. Gulbinas, O. Inganäs, M. Kemerink, “Dispersion-Dominated Photocurrent in Polymer:Fullerene Solar Cells”, *Adv. Funct. Mater.*, **24**, 4507–4514 (2014).

V. Pranculis, A. Ruseckas, D. A. Vithanage, G. J. Hedley, I. D. W. Samuel, V. Gulbinas, “The Influence of Blend Ratio and Processing Additive on Free Carrier Yield and Mobility in PTB7:PC_{71}BM Photovoltaic Solar Cells”, *J. Phys. Chem. C*, **120** (18), 9588–9594, (2016).

A. Melianas, V. Pranculis, Y. Xia, N. Felekidis, O. Inganäs, V. Gulbinas, M. Kemerink, “Photogenerated Carrier Mobility Significantly Exceeds Injected Carrier Mobility in Organic Solar Cells”, *Adv. Energy Mater.*, 1602143, (2017).

LIST OF CONFERENCE THESES

V. Pranculis, A. Melianas, V. Gulbinas, O. Inganäs, "Ultrafast charge dynamics in various polymer/PCBM solar cells". 13th European Conference on Organised Films & Roll-to-Roll Workshop (Cork, Ireland, 2013).

V. Pranculis, A. Melianas, V. Gulbinas, O. Inganäs, "Charge generation, separation and migration dynamics in polymer/PCBM solar cells probed with fs time resolution". NANOTECHNOLOGY: from fundamental research to innovations (Bukovel, Ukraine, 2013).

V. Pranculis, Y. Infahsaeng, Z. Tang, A. Devižis, D. A. Vithanage, C. S. Ponseca Jr., O. Inganäs, A. P. Yartsev, V. Gulbinas, V. Sundström, "Charge carrier generation and transport in different stoichiometry APFO3:$PC_{61}BM$ solar cells". 11th Nordic Femtochemistry Conference 2014 (Vilnius, Lithuania, 2014).

V. Pranculis, Y. Infahsaeng, Z. Tang, A. Devižis, D. A. Vithanage, C. S. Ponseca Jr., O. Inganäs, A. P. Yartsev, V. Gulbinas, V. Sundström, "Ultrafast probing of charge carrier generation and transport in APFO3:$PC_{61}BM$ solar cells". ERPOS - 13th International conference on electrical and related properties of organic solids (Swieradow Zdroj, Poland, 2014).

V. Pranculis, A. A. Paraecattil, M. Franckevicius, V. Gulbinas, J.-E. Moser, "Hole transport material influence on charge migration in $CH_3NH_3PbBr_3$ perovskite solar cells investigated by ultrafast pump-probe and Stark spectroscopy". 41-oji Lietuvos Nacionalinė Fizikos Konferencija (Vilnius, Lietuva, 2015).

V. Pranculis, A. A. Paraecattil, M. Franckevicius, V. Gulbinas, J.-E. Moser, "Skylių transportavimo medžiagų įtakos krūvininkų migracijai $CH_3NH_3PbBr_3$ perovskitiniuose saulės elementuose tyrimas ultrasparčiosios spektroskopijos metodais". 2015 Doktorantų mokslinė konferencija FizTech (Vilnius, Lietuva, 2015).

LIST OF AUTHOR’S PUBLICATIONS NOT INCLUDED IN THIS THESIS

V. Pranculis, R. Karpicz, A. Medvids, V. Gulbinas, “Fluorescence quenching in porous silicon/conjugated polymer composites”, *Phys. Status Solidi A*, **209**, 565–569, (2012).

V. Pranculis, I. Šimkienė, M. Treideris, V. Gulbinas, “Excitation energy transfer in porous silicon/laser dye composites”, *Phys. Status Solidi A*, **210**, 2617–2621, (2013)

A. A. Paraecattil, J. De Jonghe-Risse, V. Pranculis, J. Teuscher, J.-E. Moser, “Dynamics of Photocarrier Separation in $MAPbI_3$ Perovskite Multigrain Films under a Quasistatic Electric Field”, *J. Phys. Chem. C,* **120** (35), 19595–19602, (2016).

A. Melianas, V. Pranculis, D. Spoltore, J. Benduhn, O. Inganäs, V. Gulbinas, K. Vandewal, M. Kemerink, “Charge Transport in Pure and Mixed Phases in Organic Solar Cells”, *Adv. Energy Mater.*, Submitted.

AUTHOR’S CONTRIBUTION

Most of the technical experimental work was performed by the author including experimental setup and automation control adaptations. Time dependent mobility $\mu(t) = \mu^0 t^{-\alpha}$ modelling was implemented and carried out by the author. Stochastic Shrödinger equation calculations and Monte-Carlo modelling were performed by V. Abramavicius and A. Melianas respectively and are included in the thesis as they were used to model the experimental data obtained by the author and constitute integral part of presented investigations. Some of the supporting experimental data was also obtained by the author (pump-probe, CELIV, TDCF experiments). Author contributed to the data analysis and preparation of manuscripts that form the core of the thesis.

2. Major processes in organic solar cells

2.1. Light absorption and exciton generation

Converting light into electrical energy in a photovoltaic cell is a multi-step process. There is generally a good understanding and more or less a consensus of what the main steps of free charge formation are. Initial step, is the absorption of a photon by the active layer of the solar cell. Energy of the incident photon must be equal to or greater than the bandgap of the absorbing semiconductor in order to promote one of its electrons from the ground state to one of the excited states. In a semiconducting material, electron excitation is followed by ultrafast electron relaxation to an excited state with lowest energy: lowest unoccupied molecular orbital [LUMO] in an organic or bottom of conduction band in inorganic semiconductor. Vacancy left by the electron in the ground state behaves as a particle with a positive charge and is called “electron hole” or more commonly simply – hole.

Being of opposite charges electron and hole attract each other electrostatically via Coulomb interaction with the force (F):

$$F = \frac{q^2}{4\pi\varepsilon_0\varepsilon_r r^2} \qquad (1)$$

where q is the elementary charge, ε_0 is the vacuum dielectric constant, ε_r is the relative dielectric constant of the material and r is the distance between electron and hole. Coulomb potential (V) is given by:

$$V = \frac{q^2}{4\pi\varepsilon_0\varepsilon_r r} \qquad (2)$$

and can be considered as a rough estimate of the binding energy of the two charges. Inorganic semiconductors usually have quite high dielectric constant which leads to binding energies from several meV to about 100 meV.[27] These values are comparable to the energy of thermal vibrations of the host material and result in a very fast electron-hole pair dissociation into free charge carriers.

Organic semiconductors, on the other hand, have significantly lower dielectric constants ($\varepsilon_r \approx 2..4$) and considerably higher electron-hole binding energies as a result.[28,29] These tightly bound charge pairs usually undergo a series of further steps before charges can be separated and extracted from the solar cell and thus are considered as quasi-particles – “excitons” or more specifically “Frenkel excitons”.[30] Weakly bound electron-hole pairs in inorganic semiconductors are referred to as “Mott-Wannier excitons”.

2.2. Exciton migration

Exciton, as a quasi-particle composed of negatively charged electron and positively charged hole, has no net electrical charge and thus can transport energy without transporting charge. Although initially exciton can propagate through the host material as a coherent excitation, high disorder in organic materials limits this type of energy migration to only a few lattice spacings.[31] Any further exciton transport is governed by exciton diffusion dynamics – internal field of the solar cell does not interact with a quasiparticle with no charge eliminating any migration due to drift.

Exciton diffusion is most often described as a random-walk or hopping between molecules.[32–36] Hopping occurs as a Forster resonant energy transfer (FRET) via Coulombic dipole-dipole coupling of molecules [37–39] and strongly depends on the lowest possible energetic states of the exciton on the molecules in question (overlap integral between emission and absorption spectra), as well as the molecule separation distances. Highly disordered nature of organic layers leads to a broad distribution of exciton energies throughout the layer [40] and can lead to a situation where excitonic states of all the surrounding molecules have considerably higher energies than the molecule where an exciton is located. Exciton in such configuration is referred to as being in a “trap” state. If it cannot escape such trap via interactions with thermal vibrations or other excitons a trapped exciton will eventually recombine.

Excitons might also recombine spontaneously with a lifetime τ on the order of several nanoseconds.[41–43] Given exciton lifetime and diffusion coefficient D from Einstein relation:

$$D = \frac{k_B T}{q} \mu \tag{3}$$

where k_B is Boltzmann constant, T is temperature, q is elementary charge and μ – mobility. The root mean square displacement of a particle from its initial position due to the diffusion process is called diffusion length, which is given by:

$$L_D = \sqrt{\frac{\sum dL_i^2}{N}} = \sqrt{2ZD\tau} \tag{4}$$

where dL_i is the displacement of an exciton i from its original position, N is total number of excitons, and Z is equal to 1, 2 or 3 in case of one-, two- or three-dimensional diffusion, respectively. However, in the majority of scientific publications on exciton diffusion in organic semiconductors, the factor of two is omitted in Equation (4):

$$L_D = \sqrt{ZD\tau} \tag{5}$$

In this case the value L_D is approximately equal to the average displacement of a particle from its initial position. Typical exciton diffusion lengths in organic materials is on the order of 10 nm.[40,43–45]

2.3. Exciton dissociation and bulk heterojunction concept

To achieve substantial energy-conversion efficiencies, photo-generated excitons need to be dissociated into free charge carriers with a high yield. Thus exciton dissociation needs to be on the order of ps – considerably faster than competing radiative and nonradiative recombination times. Excitons can be dissociated at interfaces of materials with different electron affinities or by electric field, or the dissociation can be trap or impurity assisted.[46]

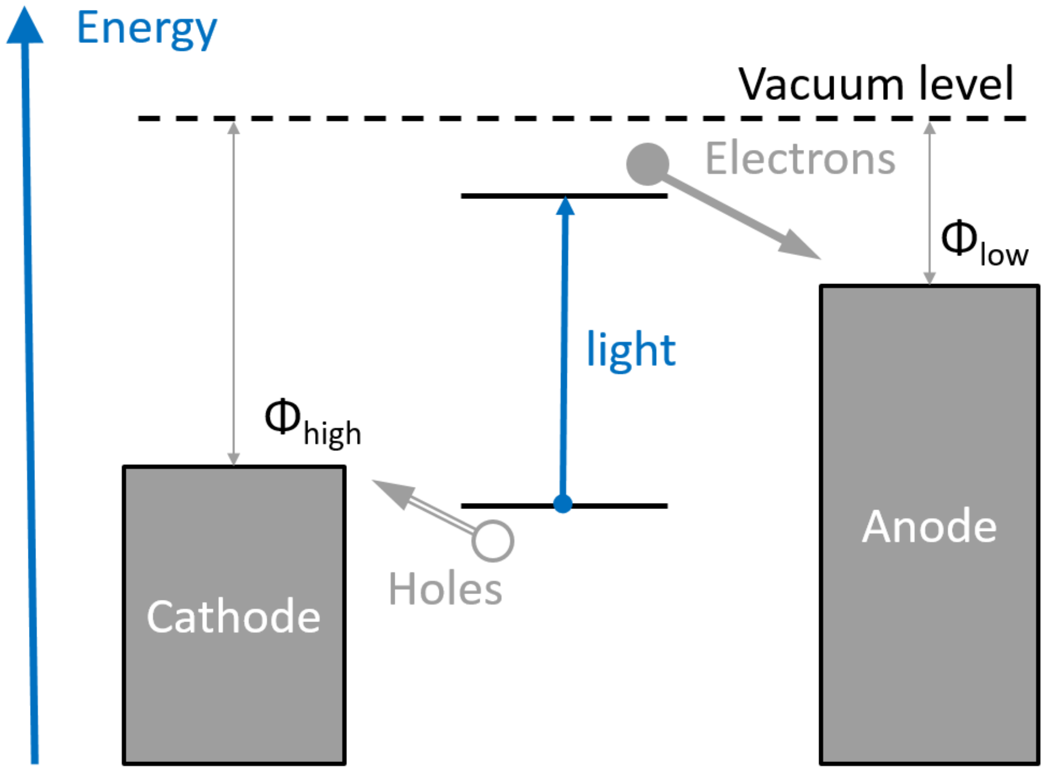

Figure 2.1 Schematic diagram of the band structure of single layer solar cell.

First organic solar cells consisted of a single layer of active material sandwiched between two metal electrodes of different work functions Φ (figure 2.1). As built-in electric field is not capable of efficient exciton dissociation, the vast majority of free charge carriers is generated at an interface between organic layer and one of the electrodes.[47–49] Given the typical exciton diffusion length of ≈10 nm and the thickness of the active layer needed to ensure proper absorption of incident light ≈100 nm one can easily spot the main weak point of such device architecture – majority of excitons never reach interface and eventually recombine. Moreover, metal-induced exciton quenching additionally reduces the exciton probability to reach the electrode and dissociate. Power conversion efficiencies of single layer organic solar cells are usually on the order of 1% or less.[48,50]

Next generation of organic PV cells tried to resolve exciton dissociation problem by introducing a second material which would have a strong electronegativity – so called “acceptor”. In such a bi-layer system (figure 2.2), exciton is produced

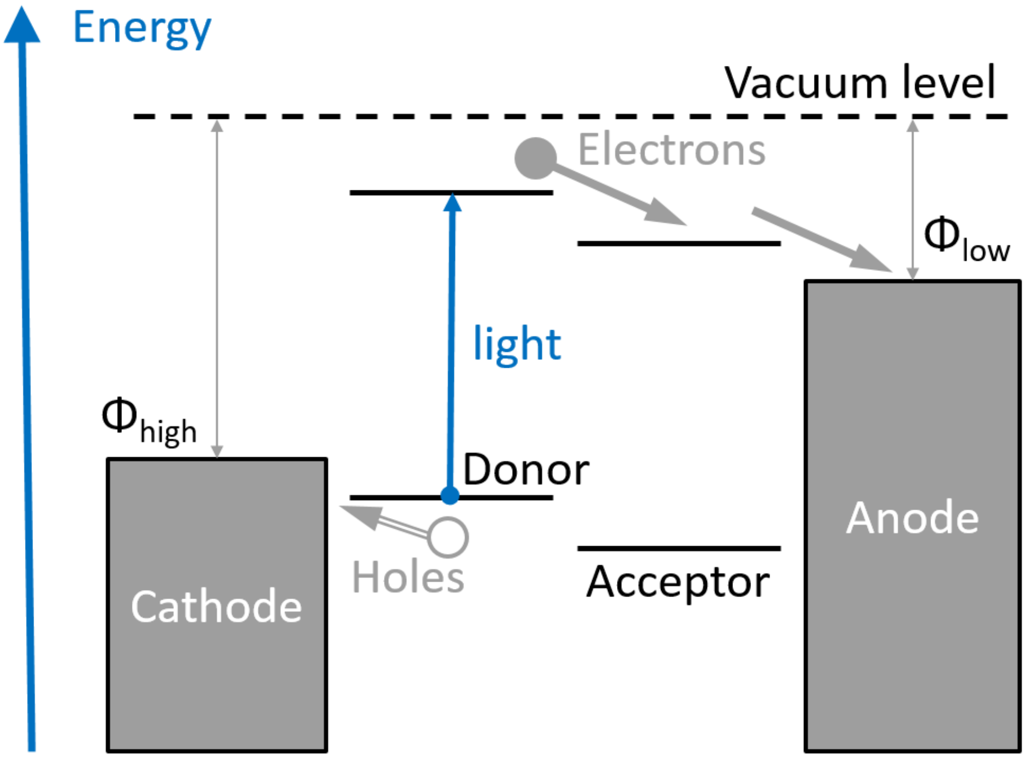

Figure 2.2 Schematic diagram of the band structure of a bi-layer solar cell.

in a “donor” layer upon absorption of a photon. This exciton consequently can diffuse within the donor layer and encounter the interface with the “acceptor”. Tailoring the difference in energy levels for the electron in donor and acceptor materials to be greater than the exciton binding energy ensures electron transfer to the acceptor and thus dissociation of the exciton. Such charge transfer was found to occur on picosecond time scale – considerably faster than competing radiative and nonradiative recombination processes and resulting in quantum efficiency close to unity.[48] Although such a planar heterojunction increased exciton dissociation efficiency it still suffered from the limitation of exciton diffusion length as compared to the thickness of the light absorbing layer.

A new concept – bulk heterojunction – addressed this issue with remarkable results.[51] Co-evaporating or spin-coating donor and acceptor materials as a mixed blend produces an interconnected network with a spatially distributed junction. Bulk heterojunction morphology ensures that any exciton generated in the donor phase will encounter donor-acceptor junction within its diffusion length, thus ensuring exciton dissociation throughout the whole thickness of the active layer.

Such an approach, however, by its nature is quite intricate and disarrayed. Higher power conversion efficiencies can be achieved not only by tailoring donor and acceptor materials,[52] but even more so, by controlling the morphology of the heterojunction. Some rather simple methods of morphology optimization, such as blending ratio, solvent optimization and thermal annealing, have been successfully performed in the past.[53–57]

2.4. CT states

Only a part of excitons produce free charge carriers upon dissociation.[58,59] In majority of the cases it is thought that excitons do indeed transfer an electron to the acceptor upon encountering donor-acceptor interface. However, even though the electron and the hole now reside on two separate materials, these charges still experience strong Coulomb attraction and could still recombine. Such a state is called charge-transfer (CT) state or CT exciton.[60,61] A last step in order to generate free electron and hole which then can migrate towards their respective contacts and generate photocurrent is dissociation of the CT state.

It is believed, that immediately after the transfer charge separation is about 1 nm – roughly the distance between the donor and acceptor molecules.[62–64] As was the case for excitons residing in a single material (chapter 1.3), electron and hole of the CT exciton with a separation distance of 1 nm would experience a strong Coulomb attraction of $E_{CT} \approx 0.4\ \mathrm{eV}$. Assuming that exciton dissociation is driven only by the thermal vibrations of the surrounding media (approximately 25 meV at room temperature), the probability of CT pair dissociation:

$$P = \exp\left(-\frac{E_{CT}}{kT}\right) \qquad (6)$$

is extremely low. Indeed, a separation distance of ≈16 nm would be needed to reach the Coulomb radius – polaron pair distance at which binding energy is equal to kT. There are, however, several factors that can influence this process.

Excess energy of the charges once the CT pair forms is one of the sources that could help in dissociation. CT excitons usually have lower energy when compared to the singlet exciton in the donor. Thus, once the electron is transferred to the acceptor the excess energy is not wasted, but rather assists further charge separation. Some exponential increase in the separation yield vs the excess energy has been observed,[65] although there are studies questioning the role of excess energy[66]

Influence of the surrounding media of the CT pair has also been investigated. The simple fact that electron (or indeed the hole) is not isolated on a separate acceptor (or donor) molecule but rather on the edge of the aggregate of the corresponding molecules ensures that entropy favors charge migration away from CT generation point. According to some rough estimates by T. M. Clarke and J. R. Durrant, the entropy contribution is of similar magnitude to the CT binding energy.[67] Another driving force originating from the surroundings is the relaxation within the energetically disordered sites. Owing to the fact that molecules in organic solids have a distribution of energetic states due to difference in orientation, conjugation and immediate neighbors, a likely scenario is that where energetically favorable molecule is in close proximity to the molecule that the charge carrier resides on.[68] Such process effectively lowers the binding energy of CT pair by roughly the transport energy in a disordered system (≈100 meV).[69]

Widening the scope even further one should also take into account the effect of electric field – both intrinsic and applied. However, the voltage needed to effectively dissociate the CT states seems to be considerably higher than that under operational conditions of the solar cell.[70–72]

2.5. Carrier dynamics and extraction

Even though CT pair dissociation into free charges might be considered the end of excitation phase the process of converting the energy of the photon into electricity is not over. A whole new set of problems and challenges ensue as free charges need to be extracted efficiently from the cell and is the main subject of this work. A comprehensive analysis of the migration of free charge carriers as well as a number of experimental and mathematical methods for such analysis are presented in the following chapters, while the current state of the research into the field is briefly summarized here.

At the moment, it is generally agreed that initial charge migration is a coherent process whereby charges migrate through delocalized band-like states, much like the initial stages of exciton migration. However, the exact details are still under debate with no consensus on the mechanism or time and distance extents of such charge migration.[66,73–75]

Once the coherence is lost, charge carrier localizes on a single molecule and the hopping transport takes over.[76] Taking an ensemble of charge carriers at the beginning of the hopping stage, their energy distribution is most often described as Gaussian and somewhat above the thermal equilibrium. Owing to the fact that in a disordered system any single site is surrounded by multiple sites with varying energy levels there is often a neighboring site with a lower energy for the charge to migrate to. Distribution of the energies of available sites (density of states - DOS) is usually assumed to have a Gaussian shape as well, although exponential tail is often included for the low energy states.[68,77–80] Such migration is even possible if there is no site in the immediate vicinity of the charge with a lower energy due to a mix of thermal activation and tunneling (figure 2.3).[68,79] The hopping rate from an initial state i with energy E_i to a final state f with energy E_f is often described using the Miller-Abrahams formulation:

$$\nu_{if} = \begin{cases} \nu_0 exp\left(-\dfrac{E_f - E_i \pm q\vec{r}_{if} \cdot \vec{F} + \Delta E_C}{k_B T}\right) = \nu_0 exp\left(-\dfrac{\Delta E}{k_B T}\right) & (\Delta E > 0) \\ \nu_0 & (\Delta E \leq 0) \end{cases} \quad (7)$$

where F is the external electric field, r_{if} – the vector connecting initial and final states, ν_0 – the attempt frequency and ΔE_C is the change in Coulomb energy. ± sign refers to electron *(+)* or hole *(-)* hopping.

Charge carriers that are not extracted fast enough eventually relax to the quasi-equilibrium transport energy which depends mainly on temperature and disorder of the system. Part of the charges naturally reach some sites with energies so deep in the DOS distribution that they effectively become trapped – that is thermal activation energy is not sufficient for them to scale (or tunnel through) the barrier to the next available site. These charges do not contribute to the photocurrent but rather stay immobile and eventually recombine leading to decline in device efficiency.

Such complex charge transport in organic solar cells often lead to erroneous mobility evaluations. Probing the local movement on the polymer chain (intrachain) or fullerene aggregate provides mobility values that would only apply if the device was void of any traps and defects.[81,82] Although this value can be used as an indicator of the potential to improve the stoichiometry of the device it has little relevance to the actual charge transport in functioning devices. On the other end of the spectrum are mobility values obtained via near-equilibrium measurement.[83–85] These methods, however, overlook the contribution of the hot carriers and thus provide useful information on the disorder of the system rather than charge extraction. What is more, mobility measurements performed on a single material devices do not take into account the increase in spatial disorder once the material is incorporated into a bulk-heterojunction structure.

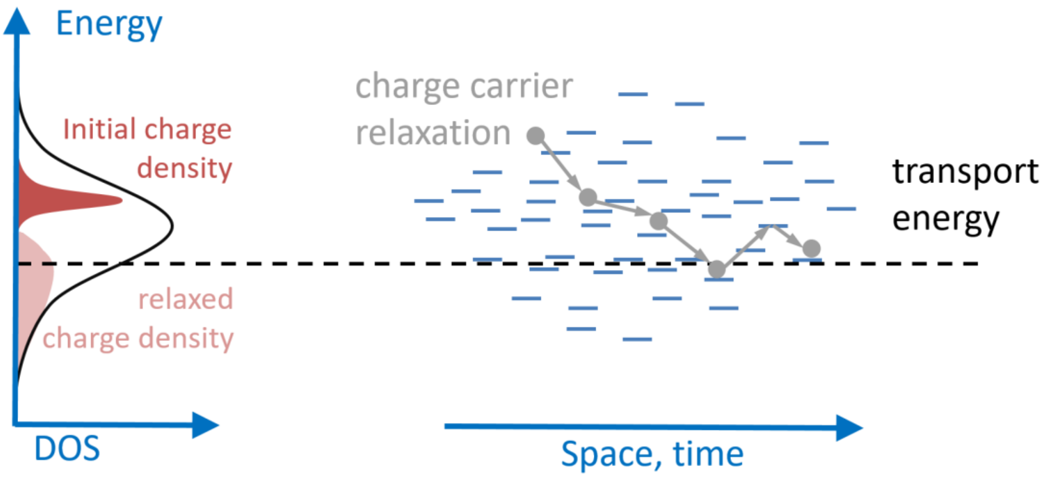

Figure 2.3 Charge carrier relaxation in organic solar cells.

3. Determining major solar cell parameters from the I-V curve

In the most basic approach PV cells are modeled as a current source in parallel with an ideal diode (Figure 3.1a). As a junction of two dissimilar semiconductors, the PV cell exhibits diode-like behavior under 'dark' conditions (red line in figure 3.1b). Upon illumination, PV cell starts to generate current and the $I - V$ curve is shifted along the I axis (green line in Figure 3.1b). Measured current in this case would be equal to the generated photo-current minus the 'dark' diode current:

$$I = I_L - I_D = I_L - I_0\left(e^{\frac{qV}{kT}} - 1\right) \qquad (8)$$

where I_0 is the diode dark saturation current, I_L is the current generated due to illumination of the solar cell, $q = 1.6\times10^{-19}\ C$ is the elementary charge, $k = 1.38\times10^{-23}\ J/K$ is the Boltzmann constant, T is the cell temperature in Kelvins, and V is applied voltage (bias). Although obtaining the I-V curve of an illuminated PV cell (green line in Figure 3.1b) is a rather simple measurement, it allows to determine some key parameters.

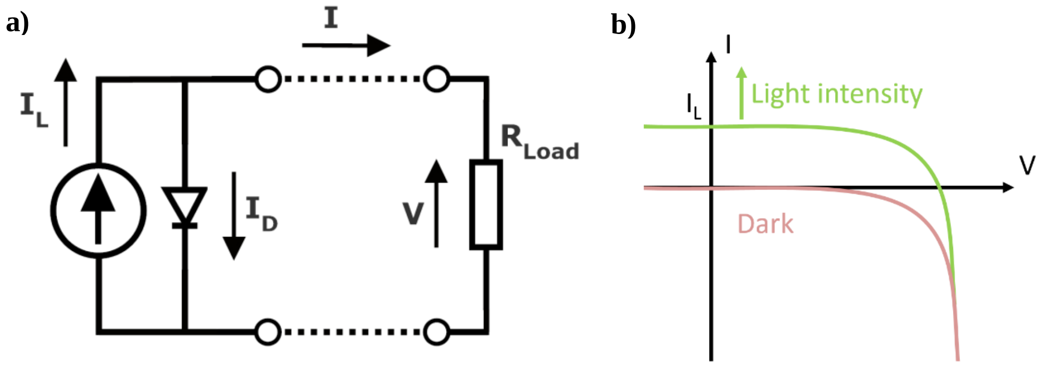

Figure 3.1 Simplified equivalent circuit model of a solar cell (a) and I-V curves (b).

3.1. Short Circuit Current

The short circuit current I_{SC} is the current measured with no applied voltage. As the name implies, at this point PV cell is in short-circuit condition – the only load on the cell is a low impedance ampermeter. For an ideal cell, this maximum current value is the total current produced in the solar cell by photon excitation.

I_{SC} strongly depends on the charge generation rate and diffusion lengths. The I_{SC} might be reduced due to recombination which results in loss of photo-generated charge carriers.

$$I\ (at\ V = 0) = I_{SC} \tag{9}$$

3.2. Open Circuit Voltage

As with the short circuit current, the open circuit voltage is a self-describing term. Open-circuit voltage, V_{OC}, is voltage on the cell when there is no current passing through it. It is the maximum voltage available from a solar cell. Generally, V_{OC} increases logarithmically with intensity, and then saturates when intensity is large enough.[47]

$$V\ (at\ I = 0) = V_{OC} \tag{10}$$

3.3. Maximum Power Point

The electric power (P) produced by the cell can be easily calculated from the Ohm's law as $P = IV$. At the I_{SC} and V_{OC} the power will be zero and the maximum value for power (Maximum Power Point – MPP) will occur between

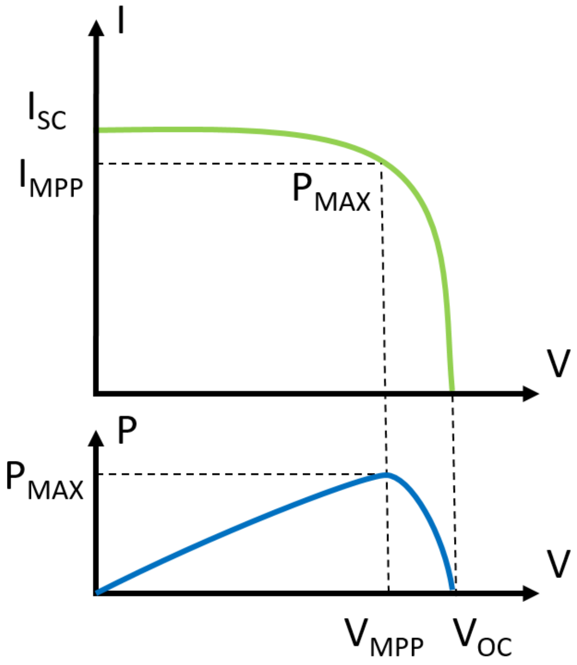

Figure 3.2 Power obtainable at different points along the I-V curve.

the two points along the $I - V$ curve. The voltage and current at this maximum power point are denoted V_{MPP} and I_{MPP} respectively.

3.4. Fill Factor

The Fill Factor (FF) is essentially a measure of the quality of the solar cell. It is defined as the ratio of the maximum power from the solar cell to the product of V_{OC} and I_{SC} (also known as theoretical power P_T). FF can also be interpreted graphically as the ratio of the rectangular areas depicted in figure 3.3. PV cells with a high fill factor have a low equivalent series resistance and a high equivalent shunt resistance, so less of the current produced by the cell is dissipated in internal losses. Fill factor most often is represented as a percentage.

$$FF = \frac{P_{MAX}}{P_T} = \frac{I_{MPP} \cdot V_{MPP}}{I_{SC} \cdot V_{SC}} \qquad (11)$$

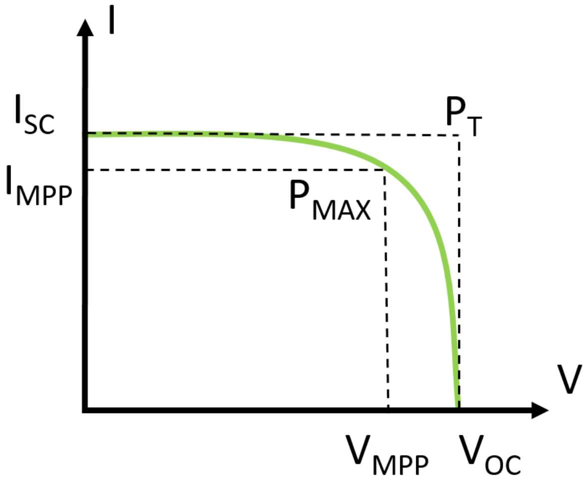

Figure 3.3 Graphical representation of the Fill Factor.

3.5. Efficiency

Photovoltaic cell efficiency is the most commonly used parameter to compare the performance of different cells for it is efficiency that indicates how much power solar cell produces. Efficiency of a photovoltaic cell is defined as the ratio of the electrical power output P_{out}, compared to the solar power input, P_{in}. As the solar cell can be operated at its maximum power point (MPP) P_{out} can be taken to be P_{MAX} to get the maximum efficiency:

$$\eta = \frac{P_{out}}{P_{in}} \Rightarrow \eta_{MAX} = \frac{P_{MAX}}{P_{in}} \tag{12}$$

Solar power input, P_{in}, is taken as the product of the irradiance of the incident light [W/m^2], with the surface area of the solar cell [m^2]. As is the case with all $I - V$ parameters, PV cell efficiency can be affected by ambient conditions such as spectrum and intensity of the incident light and temperature. Therefore, it is recommended to test all PV cells using similar conditions in order to be able to compare different cells accurately. Terrestrial solar cells are measured under AM1.5 irradiance conditions and at a temperature of 25°C.

3.6. Series and Shunt Resistance

Efficiency of an operating solar cell might be reduced due to parasitic resistances, of which series resistance (R_S) and shunt resistance (R_{SH}) are the most common. Thus, for a non-ideal solar cell equation (8) and the corresponding circuit diagram (figure 3.1) should be modified to include R_S and R_{SH} (figure 3.4) as well as a diode ideality factor n:

$$I = I_L - I_0\left(e^{\frac{q(U+IR_S)}{nkT}} - 1\right) - \frac{U + IR_s}{R_{SH}} \tag{13}$$

Series resistance originate mainly from the resistance of the electrodes and contact resistance between the different layers of the cell. The main impact of

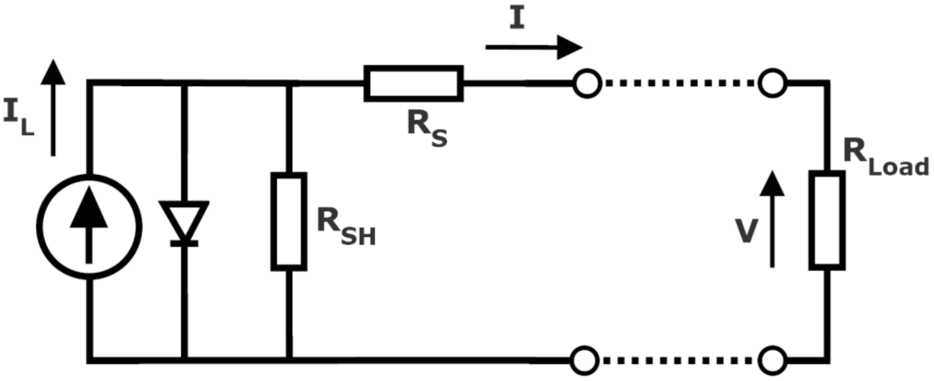

Figure 3.4 Equivalent circuit model of a solar cells including series and shunt resistances.

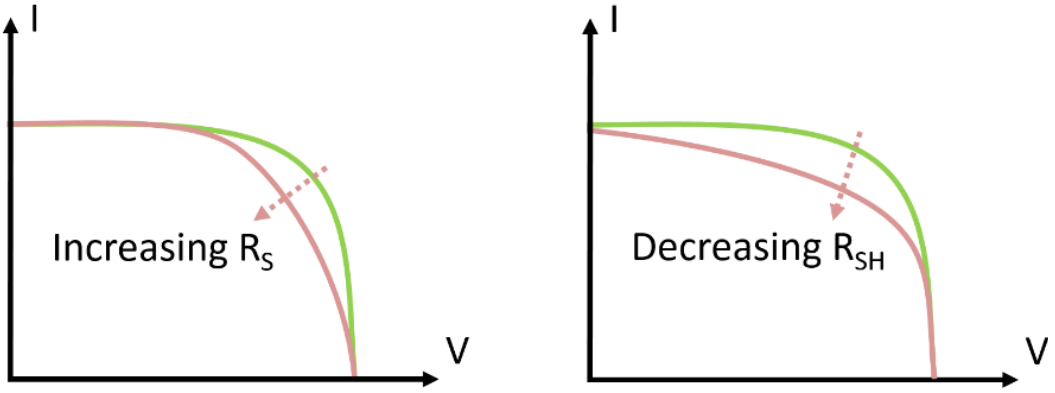

Figure 3.5 Effect of series and shunt resistances on a performance of a solar cell.

series resistance is to reduce the fill factor, although excessively high values may also reduce the short-circuit current. V_{OC} on the other hand, is not affected by the series resistance since at open circuit there is no current flow through the cell and R_S.

Low shunt resistance is typically caused by manufacturing defects. Shunt resistance provide photo-generated current an alternative path thus reducing current extracted from the solar cell. If R_{SH} is very low, V_{OC} will also be affected. In an ideal cell, R_{SH} should be infinite.

An estimate for the value of the shunt and series resistances of a PV cell can be determined from the slopes of the $I - V$ curve at V_{OC} and I_{SC}, respectively (figure 3.5).

4. Experimental and mathematical methods

4.1. Pump-Probe

Pump-Probe (figure 4.1) is a well-established method to measure transient absorption. The sample under investigation is excited by the “pump” pulse at time $t = 0$. Changes in the absorption spectra of the sample are then detected using a broad spectrum (usually white light supercontinuum) “probe” pulse after some delay Δt. Optical delay line is used to change delay between pump and probe pulses (Δt) in order to map the evolution of absorption spectra over time. By blocking every second pump pulse one can determine the excitation induced change in sample absorbance (ΔA) at a given delay time Δt using Beer-Lambert law:

$$A_{np}(\Delta t) = -\log\left(\frac{I_{np}}{I_0}\right) \tag{14}$$

$$A_p(\Delta t) = -log\left(\frac{I_p}{I_0}\right) \tag{15}$$

$$\Delta A(\Delta t) = A_p(\Delta t) - A_{np}(\Delta t) = log\left(\frac{I_{np}}{I_p}\right) \tag{16}$$

where A_{np} and I_{np} are sample absorbance and probe pulse intensity with no pump pulse present, A_p and I_p are sample absorbance and probe pulse intensity with pump pulse and I_0 is probe pulse intensity before entering the sample.

Transient absorption measurements can also be performed in a reflection mode. In such case pump and probe beams enter the sample from the transparent side, pass through the entire sample and are reflected by the back reflective side. Reflected beams then pass the sample a second time and are registered by the detector. The same approach can be used to calculate differential absorption with only a minor difference of a longer optical path.

Pump-probe measurement presented here were performed in reflection mode in two different time windows, 100 fs – 10 ns and 10 ns – 10 μs. For the shorter time frame, pump pulses with 30 fs duration were produced by a 1 kHz non-

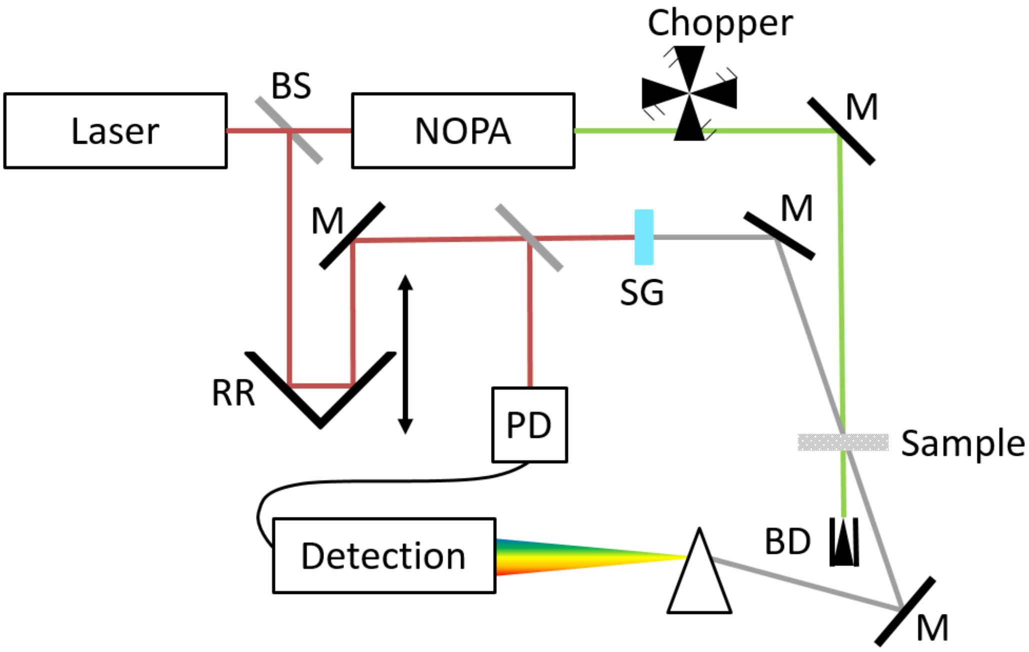

Figure 4.1 Schematic representation of a Pump-Probe experiment.

collinear parametric amplifier at 550 nm (TOPAS-White, Light Conversion Ltd). The long time frame measurements used 1-ns Nd-YAG laser (ACE) pump pulses at 532 nm. The probe pulses at 900 nm were generated by a non-collinear parametric amplifier (NOPA, Clark MXR, Inc) for all measurements. The probe pulses were optically and electronically delayed for the shorter and longer time frames, respectively.

4.2. Streak camera

The streak camera is an ultra-fast detector used to capture fluorescence of the sample. A typical experimental streak camera setup is shown in figure 4.2. The sample under investigation is excited by an ultrafast laser system producing light pulses of duration less than 100 fs. The fluorescence of the sample is collected by parabolic mirrors and focused to the slit of the spectrograph. Fluorescence spectrum is then projected as a line on the photocathode inside the streak camera and converted into photoelectrons. The resulting electron flux is then collimated and accelerated while simultaneously being deflected by an electric field which is varied with an ultrahigh speed by the sweep unit. This results in the transformation of the photon arrival time into the spatial coordinate along the

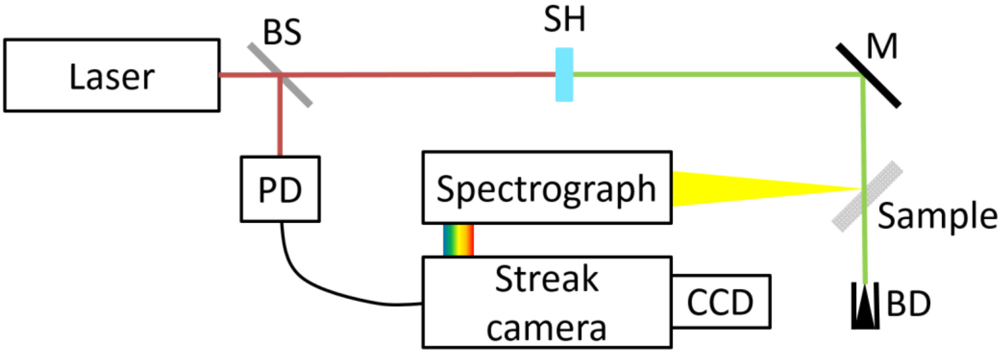

Figure 4.2 Schematic representation of fluorescence measurement using streak camera.

deflecting field and perpendicular to the spectral coordinate. After amplification in micro-channel plate, electrons are projected onto phosphor screen and a CCD camera then records resulting image. The light intensity detected by the CCD camera reflects the electron density generated by the initial fluorescence while two spatial axes are used to obtain spectral and temporal resolutions.

For any measurements presented below, samples were excited with a second harmonic (515 nm) of a femtosecond (pulse duration 70 fs) Yb:KGW oscillator (Pharos, Light Conversion Ltd.) working at 76 MHz repetition rate. Hamamatsu C5680 streak camera was used to detect and register fluorescence dynamics. The maximum time resolution of the system was about 3 ps.

4.3. Charge extraction by linearly increasing voltage

Charge extraction by linearly increasing voltage (CELIV) and photo-induced CELIV (photo-CELIV) are simple yet powerful methods used to measure charge carrier mobility and recombination in organic solar cell.[86,87] Illustrative traces of voltage applied during a typical photo-CELIV experiment and the sample response curves are shown in figure 4.3.

Linearly increasing reverse biased voltage with the rise speed $A' = dV/dt = V_{pulse}/t_{pulse}$ is applied to the device under test and the current is recorded by an oscilloscope. Typical electrical response is a rectangular-shaped current transient with a plateau value corresponding to the capacitive displacement current:

$$j(0) = \frac{A'\varepsilon_0\varepsilon_r}{d} \tag{17}$$

where ε_r and ε_0 are the dielectric constants of the material and vacuum, respectively, and d is the thickness of the active layer. A short laser pulse (results presented in this work were obtained using nanosecond laser pulses at a wavelength of 500 nm) creates a number of charge carriers in the device at a time delay t_{delay} before extraction. A forward bias voltage U_{offset} is applied to compensate for the built-in potential of the device and force the photogenerated charge to remain in the device and recombine. After t_{delay}, non-recombined charge is extracted with linearly increasing voltage. Integrating the area under the CELIV traces provides the photo-generated carrier density (from trace captured with light pulse) and equilibrium carrier density (from trace captured with no light pulse). Non-recombined charge then can be calculated as:

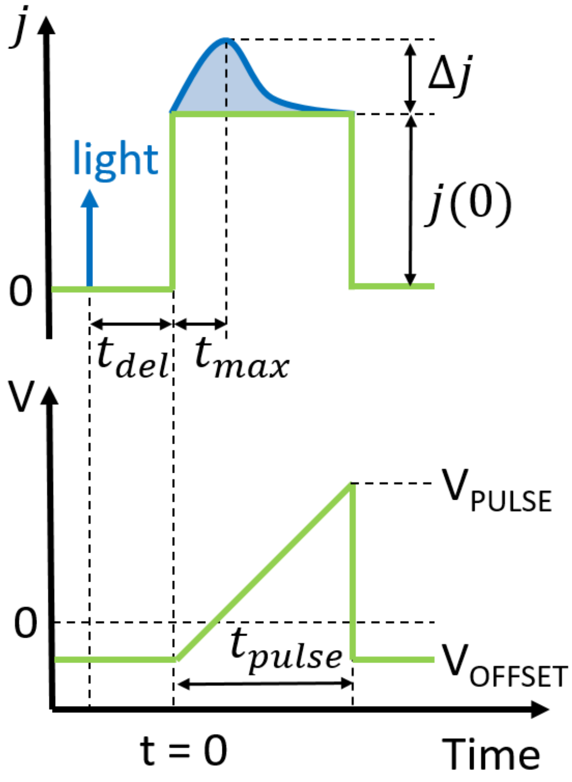

Figure 4.3 Applied voltage kinetic (bottom) during CELIV experiment and corresponding current (top) after photoexcitation (blue) and when no light is present (green).

$$Q_e = A \int_0^{t_{pulse}} \Delta j \, dt \tag{18}$$

where A is the area of the electrode and Δj is the current density obtained as the difference between the current measured after the photoexcitation j and the capacitive current measured with no illumination $j(0)$, which is assumed to be constant over the whole pulse duration. The carrier mobility can be estimated from the time t_{max} at which current reaches a peak value [87] :

$$\mu = \frac{2d^2}{3A' t_{max}^2 \left(1 + 0.36 \frac{\Delta j}{j(0)}\right)} \quad if\ \Delta j \leq j(0) \tag{19}$$

4.4. Time delayed collection field

A somewhat similar method employed recently to investigate the role of the electric field is the Time-Delayed-Collection-Field (TDCF) technique.[88,89] In TDCF, charges are generated by a laser pulse and extracted by a rectangular voltage pulse with height V_{coll}. This pulse is delayed with respect to the excitation pulse by the delay time $t = t_{del}$, which can be varied. Produced current is then measured with an oscilloscope. As was the case in the photo-CELIV measurements, forward bias voltage V_{pre} is applied before the collection pulse in order to compensate the built-in potential of the solar cell. Schematic representations of the traces are shown in figure 4.4. Current measured with the laser pulse blocked consists of two pulses of opposite direction on the onset and end of V_{coll}. This response is capacitive in origin and enables one to estimate the RC constant of the device. Once the excitation pulse is unblocked and allowed to reach the device measured current is augmented with a third small pulse at the time of excitation $t = 0$ and an increase in the signal at the time $t = t_{del}$ (light blue shaded area in figure 4.4). Photocurrent measured at $t = 0$ is caused by the carriers which are driven out of the active layer by the internal electric field of the device and should be minimized by adjusting V_{pre}. Increase in the signal at $t = t_{del}$ is caused by the photo-carriers that survived for the

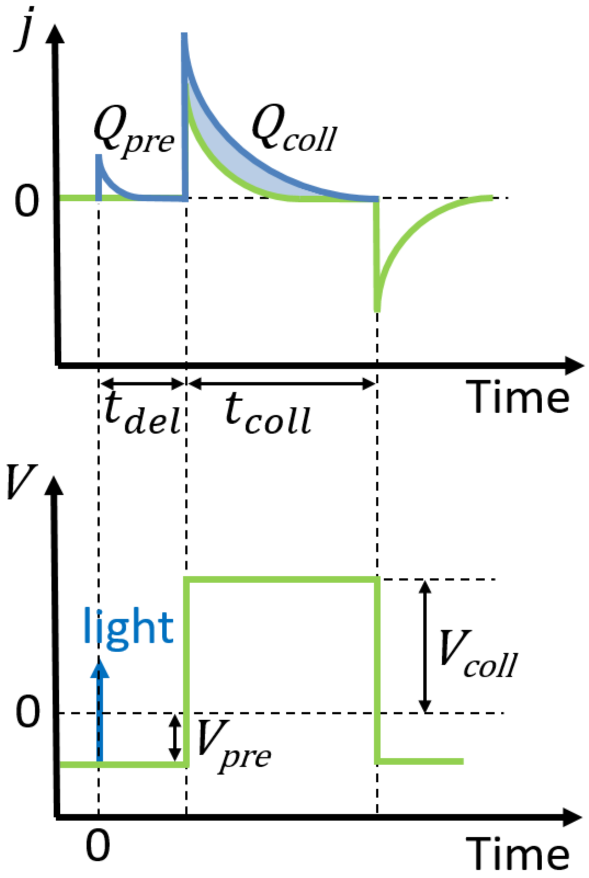

Figure 4.4 Applied voltage kinetic during TDCF experiment (bottom) and corresponding current (top) after photoexcitation (blue) and when no light is present (green).

duration of the delay of the collection pulse. Total photogenerated charged that was extracted can be calculated using the same method as is used in the photo-CELIV measurements (equation 18). Thereby, by varying the delay between photoexcitation and collection field allows one to probe the temporal evolution of the photogenerated charges and quantify recombination losses. What is more, varying the strength of pre-bias voltage allows to study field dependence of charge generation while varying the collection field intensity reveals its influence on charge extraction and recombination.

4.5. Time-Resolved Mobility Measurements

Most of the classical models used to describe organic solar cells are based on an extreme assumption that mobility is constant and equal to that measured in steady (or quasi-steady) state conditions,[90–93] e.g. mobility values obtained by using the photo-CELIV method described above. A unique Time-Resolved

Electric Field Induced Second Harmonic generation (TREFISH) method [94] in combination with integrated photocurrent measurements allows for the probing of mobility in the time range from sub-picosecond to tens of micro-seconds. Insight into mobility dynamics over such a vast temporal range enables one to defeat the shortcomings of classical device models that use steady-state mobility values and gain insight into charge transport on molecular and ultrafast scales.

4.5.1. Integrated Photocurrent

Integrated Photocurrent (IPC) was measured simultaneously with any TREFISH measurement by connecting high impedance oscilloscope input across the load resistor (figure 4.5). This allowed to extend the time range of measured voltage drop due to extraction of charges after photoexcitation to over 10 microseconds.

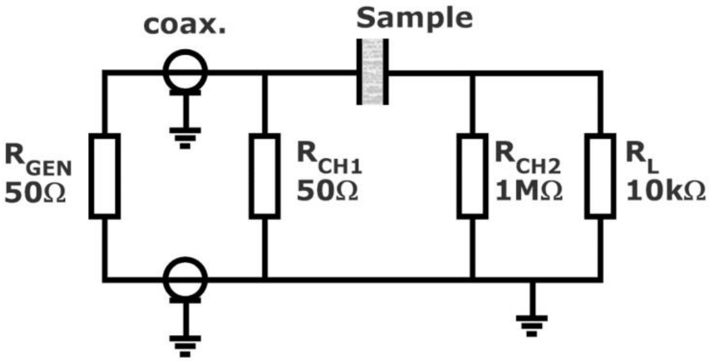

Figure 4.5 Circuit diagram of integrated photocurrent measurement.

Sample with a typical capacitance of about 1 nF and the 10 kΩ load resistor R_L constitute RC differentiator (figure 4.6) with time constant of approximately 10 microseconds. It is therefore important to take this into account when analyzing data. Voltage measured on the output of RC differentiator is given by:

$$U_{out} = RC\frac{dU_{in}}{dt} \tag{20}$$

True voltage on the sample can then be calculated by adding the ‘correction’ term to the original signal which accounts for RC differentiator:

$$U_{sample}(t) = U_{osc}(t) + \int_{0}^{t} \frac{U_{osc}(t)}{RC} dt \tag{21}$$

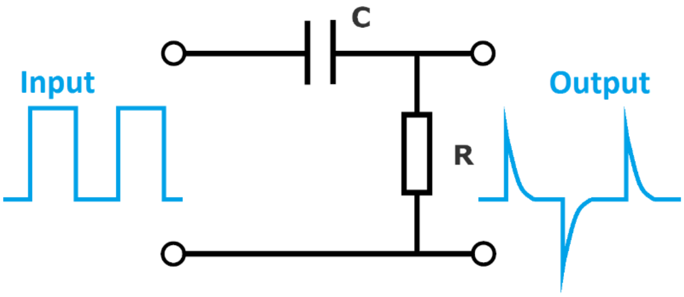

Figure 4.6 Effect of RC differentiator on an electrical signal.

4.5.2. TREFISH

Electric Field Induced Second Harmonic (EFISH) generation is commonly used in various fields of research for the determination of molecular hyperpolarizability.[95–98] This technique is based on a nonlinear light interaction with a given material. Nonlinear material properties are described by expanding the polarization in a power series:

$$\vec{P} = \vec{P}^{(1)} + \vec{P}^{(2)} + \vec{P}^{(3)} + \cdots + \vec{P}^{(n)} + \cdots \qquad (22)$$

where $\vec{P}^{(1)}$ is linear in the electric field, $\vec{P}^{(2)}$ is quadratic in the electric field, $\vec{P}^{(3)}$ is cubic in the electric field and so on. One can then define nth-order nonlinear susceptibility, $\chi^{(n)}$ in terms of the nth-order polarization and the electric fields as:

$$P_i^{\omega_{n+1}} = \sum_{jk\ldots m} \chi_{ijk\ldots m}^{(n)}(-\omega_{n+1}; \omega_1, \ldots, \omega_n) E_j^{\omega_1} E_k^{\omega_2} \ldots E_m^{\omega_n} \qquad (23)$$

where $P_i^{\omega_{n+1}}$ is the i-component of the nth-order polarization field at frequency ω_{n+1}, $E_j^{\omega_1}$ is j-component of the electric field amplitude at frequency ω_1, and the $\chi_{ijk\ldots m}^{(n)}$ terms are components of the nth-order electric susceptibility of the medium. Second harmonic generation in a material is governed by 2nd-order susceptibility, which is equal to zero in any centrosymmetrical medium [99] :

$$P_i(2\omega) = \frac{1}{2}\chi_{ijk}^{(2)}(-2\omega; \omega, \omega) E_j(\omega) E_k(\omega) \qquad (24)$$

The Electric-Field-Induced Second-Harmonic Generation (EFISHG) technique makes it possible to generate second harmonic signal in unordered, centrosymmetrical materials. The centrosymmetry of the medium is broken by applying a DC electric field due to interactions of the permanent dipoles of the molecules and the electric field. By the interaction of the two optical fields, coming from a laser beam, and the static electric field we actually measure a third-order effect, related to $\chi^{(3)}$ through:

$$P_i(2\omega) = \frac{3}{2}\chi^{(3)}_{ijkl}(-2\omega; \omega, \omega, 0)E_j(\omega)E_k(\omega)E_l(0) \qquad (25)$$

where $\chi^{(3)}_{ijkl}$ is the macroscopic 3rd-order susceptibility. $E_j(\omega)$ and $E_k(\omega)$ are the optical electric field components at frequency ω, while $E_j(0)$ is the applied static electric field.

There is no need to go into detail in elucidating the combinations of the $\chi^{(3)}$ tensor components that contribute to the second harmonic signal in EFISH experimental geometry. It is sufficient for measuring dynamics to know that intensity of the second harmonic signal is proportional to the square of applied electric field [99] :

$$I(2\omega) \sim E_j(0)^2 \qquad (26)$$

In the context of organic solar cells, EFISH is implemented as follows. There is no current passing through a solar cell when it is negatively biased and not illuminated (figure 3.1b). One then can consider active layer of a solar cell to be an insulator sandwiched between two electrodes, forming a parallel plate capacitor with capacitance:

$$C = \frac{\varepsilon_0\varepsilon_r A}{d} \qquad (27)$$

where ε_0 is the vacuum dielectric constant, ε_r is the relative dielectric constant of the active layer, *A* is the area of the electrodes and *d* is thickness of the active layer. Electric field between two contacts is then given by:

$$E_j(0) = E = \frac{U_0}{d} + E_{built-in} \tag{28}$$

Or

$$E = \frac{Q}{\varepsilon_0 \varepsilon_r A} + E_0 \tag{29}$$

where U_0 is the applied (reverse bias) voltage, Q is charge on the contacts and $E_{built-in}$ is the built-in electric field due to different work functions of the electrodes. Upon optical excitation of the solar cell photo-generated charges drift in the applied electric field and discharge the cell-capacitor. It is important to note at this point that photo-generated charges should only reduce the electric field by a small amount (preferably less than 10%) in order to avoid any space-charge and bimolecular recombination effects.[100–103] Electric field variations in the device then can be estimated by measuring the intensity of the generated second harmonic (equation 26). Extracted charge can then be calculated using simple capacitor relation:

$$\Delta Q = C\Delta U \tag{30}$$

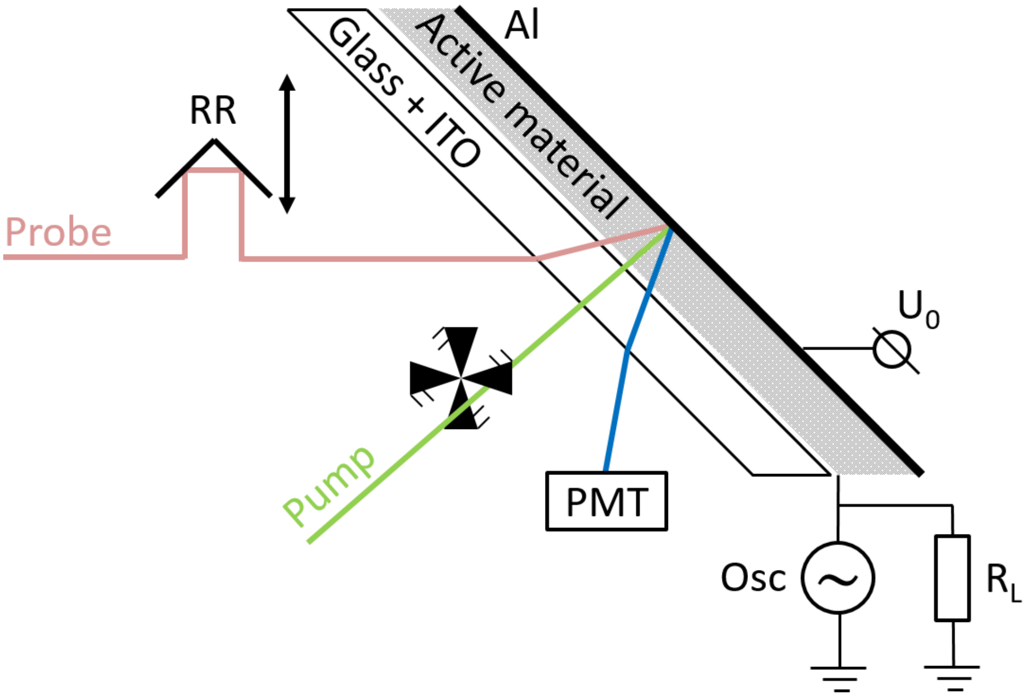

Figure 4.7 Schematic representation of TREFISH experiment.

Sub-picosecond time resolution can be added to EFISH measurements by implementing a setup similar to that of conventional pump-probe (figure 4.7). TREFISH measurements presented here were based on a Ti-Sapphire laser system (Integra-C, Quantronix) generating 130 fs long pulses at a frequency of 1 kHz. After passing a beam-splitter, part of the fundamental laser radiation of 810 nm was directed to an optical delay line and used as the probe to generate the second harmonic signal of 405 nm which them was detected by a photo multiplier tube (PMT). Depending on the experimental conditions, remainder of the fundamental radiation was either used to excite the sample directly or pumped collinear optical parametric amplifier of white-light continuum (TOPAS C, Light Conversion Ltd.) which then produced light pulses of desired wavelength. Every other excitation pulse was blocked by a chopper in order to measure the ratio of second harmonic generated with and without excitation of the sample at the particular delay. Reverse bias was applied through a load resistor of 10 kΩ. In order to extend lifetime of the samples the external voltage was applied to the sample in a pulsed mode by the square pulse generator synchronized with the laser. Duration of the voltage pulses was set to tens of microseconds.

It should be pointed out that TREFISH measurements require [in most cases] an applied voltage corresponding to an external electric field several times higher than that in an operating solar cell. The stronger field leads to faster charge separation, drift and extraction, implying that absolute durations of these events should not be taken as characterizing processes in operating solar cells. Nevertheless, the observed trends and material dependencies contain relevant information about the functioning of the solar cells.

4.5.3. TREFISH and IPC analysis

As was shown for previously [94,104] two components are responsible for the change of the electric field upon optical excitation: excitons $\Delta E_{exc}(t)$ and, charge carriers $\Delta E_{cc}(t)$. Exciton contribution results in ultrafast drop in electric field during the excitation pulse and a slower recovery when excitons decay.[94]

No ultrafast exciton-related field response was observed in most of the following TREFISH measurements, which confirms ultrafast and very efficient exciton dissociation.[94] Therefore, any change measured in electric field in the solar cells will be interpreted as a result of charge carrier migration. $\Delta E_{cc}(t)$ can be expressed by the average drift distance $\langle l(t)\rangle$ and the density of photogenerated charges $n_{cc}(t)$ (equation 29):

$$\Delta E_{cc}(t) = \frac{Q_{cc}}{\varepsilon_0 \varepsilon_r A} = \frac{n_{cc}(t) q \langle l(t)\rangle}{\varepsilon_r \varepsilon_0} \qquad (31)$$

Equation (30) then can be rewritten as:

$$\Delta Q(t) = C\Delta U(t) = Cd\Delta E_{cc}(t) = \frac{n_{cc}(t) q \langle l(t)\rangle}{\varepsilon_r \varepsilon_0} Cd \qquad (32)$$

In case of thin film with low optical density and bulk heterojunction morphology, charge carriers are generated homogeneously over the film thickness. Moreover, photogeneration of charges is much faster than their migration and extraction at the electrodes. Thus, the concentration of photogenerated charge carriers in the volume of the solar cell can be approximately written as:

$$n_{cc}(t) = n_{cc}^0 \left(1 - \frac{\langle l(t)\rangle}{d}\right) \qquad (33)$$

where n_{cc}^0 is the initial photogenerated carrier concentration. Substituting $n_{cc}(t)$ in the equation (32) with the above expression and sample capacitance with expression in equation (27) gives:

$$\Delta Q(t) = n_{cc}^0 q A \left(\langle l(t)\rangle - \frac{\langle l(t)\rangle^2}{d}\right) \qquad (34)$$

Solving quadratic equation for $\langle l(t)\rangle$ then produces:

$$\langle l(t)\rangle = d\left(1 \mp \sqrt{1 - \frac{4}{2dqAn_{cc}^0}\Delta Q(t)}\right) \qquad (35)$$

Now, $\Delta Q = n_{cc} q A \langle l(t)\rangle$ from above, can be rewritten as:

$$Aqn_{cc} = \frac{\Delta Q}{\langle l(t) \rangle} = \frac{C\Delta U}{\langle l(t) \rangle} \tag{36}$$

At long time scales, when all the charge has been extracted $n_{cc}(t) = n_{cc}^{0}$ the mean drift distance must be equal to the thickness of the device $\langle l(t) \rangle = d$. This gives:

$$An_{cc}^{0}e = \frac{\Delta Q^{0}}{d} \tag{37}$$

or

$$\Delta Q^{0} = \ Adn_{cc}^{0}q \tag{38}$$

which passes a quick sanity check (Ad is the volume of the cell, $n_{cc}^{0}q$ is the charge density, thus multiplying those terms should produce total charge in the cell Δq^{0}). At this point it is important to note one subtle yet very important quirk. Although solar cell generates charge ΔQ^{0} (corresponding to n_{cc}^{0}), this charge comes from both, electrons and holes. That means that the charge on each of the plates of capacitor decreases only by:

$$\Delta Q_{max} = \frac{Adn_{cc}^{0}q}{2} \tag{39}$$

And that is what is measured and what should be used when analyzing TREFISH and IPC data:

$$\langle l(t) \rangle = d\left(1 - \sqrt{1 - \frac{4}{2d}\frac{d}{2\Delta Q_{max}}\Delta Q(t)}\right) \tag{40}$$

Finally, substituting ΔQ for ΔU:

$$\langle l(t) \rangle = d\left(1 - \sqrt{1 - \frac{\Delta U(t)}{U_{max}}}\right) \tag{41}$$

where U_{max} is the maximum measured voltage (at the microsecond time scale). Average mobility is then easily obtained by calculating temporal derivative of $\langle l(t) \rangle$:

$$\mu = \frac{1}{E_0}\frac{d\langle l(t)\rangle}{dt} \tag{42}$$

4.6. Modeling of charge transfer dynamics

While presented experimental techniques alone are able to reveal swaths of insight into charge generation and migration in organic solar cells, computer modeling is invaluable on its own right. Various models not only allow to better explain most of the features observed in experiments but reveal the underlying reasons as well.

4.6.1. Mobility model $\mu(t) = \mu^0 t^{-\alpha}$

TREFISH and IPC data enables one to determine mobilities of several distinct charge species, i.e. to separate electron and hole mobilities. One of the easiest way is by using power-law mobility model. At the heart of this model lies the assumption that electron and hole mobilities decay over time as a function:

$$\mu_{e,h}(t) = \mu_{e,h}^0 t^{-\alpha} \tag{43}$$

where $\mu_{e,h}^0$ is initial electron or hole mobility and α is the power law constant. Considering charge contribution to the voltage drop measured by TREFISH and IPC as the integral of photocurrent $j(t)$ gives:

$$\Delta U_{e,h}(t) = \frac{\Delta Q_{e,h}(t)}{C} = \frac{1}{C}\int_0^t j_{e,h}(t')dt' \tag{44}$$

The photocurrent itself is proportional to the carrier concentration and their average drift speed:

$$\begin{aligned} j_{e,h}(t) &= Aqn_{e,h}(t)\frac{d\langle l(t)\rangle_{e,h}}{dt} = \\ &= Aqn_{e,h}^0\left[1 - \frac{< l(t) >_{e,h}}{d}\right]\frac{d < l(t) >_{e,h}}{dt} \end{aligned} \tag{45}$$

Substituting photocurrent in equation (44) with the expression above:

$$\Delta U_{e,h}(t) = \frac{Aen_{e,h}^0}{C}\int_0^t \left[1 - \frac{< l(t') >_{e,h}}{d}\right]\frac{d < l(t') >_{e,h}}{dt'}dt' \tag{46}$$

Using the expression (42) for average drift distance:

$$\Delta U_{e,h}(t) = \frac{Aen_{e,h}^{0}}{C} \int_{0}^{t} \left[1 - \frac{U_0 \int_0^{t'} \mu_{e,h}(t'')dt''}{d^2} \right] \mu_{e,h}(t') \frac{U_0}{d} dt' \quad (47)$$

First term of the above expression can be tied to the measurements via equations (30) and (39) with regard to the measured voltage drop at long time scales:

$$\Delta U^{max} = \frac{Aqn_{e,h}^{0}d}{C} \quad (48)$$

One now has a set of equations that describe the full dynamics of electric field (or voltage) variations after the photoexcitation in terms of two charge species with only four variables - μ_e^0, μ_h^0, α_e and α_h:

$$\Delta U(t) = \Delta U_e(t) + \Delta U_h(t) \quad (49)$$

$$\Delta U_e(t) = \frac{\Delta U^{max} U_0}{d^2} \int_{0}^{t} \left[1 - \frac{U_0}{d^2} \int_{0}^{t'} \mu_e(t'')dt'' \right] \mu_e(t')dt' \quad (49.1)$$

$$\Delta U_h(t) = \frac{\Delta U^{max} U_0}{d^2} \int_{0}^{t} \left[1 - \frac{U_0}{d^2} \int_{0}^{t'} \mu_h(t'')dt'' \right] \mu_h(t')dt' \quad (49.2)$$

4.6.2. Kinetic Monte-Carlo Model

Although most of the cases presented in this work are described well with the power-law mobility model explained above it falls short when the concentration of one of the materials is very low. It should not be very surprising, having in mind that at such concentrations one of the blended materials does not reach percolation limit. Moreover, as a top-down approach, power-law mobility model only uncovers time dependence of charge carrier mobilities, not the underlying reasons. Kinetic Monte-Carlo modeling, on the other hand, is a bottom-up approach to the same problem.

This model is implemented on a simple cubic grid, i.e. each site is six-fold coordinated. Nearest neighbor hopping distance a_{NN} then equals the lattice constant. In order to simulate transient response to a short light pulse, each simulation is started by creating an initial concentration c_0 of excitons on an otherwise empty calculation grid. Given the high photon energy employed in the experiments an equal excitation probability is assumed for all sites, in other words excitons are generated at fully random positions. Both in pulsed and steady-state simulations all charges are tracked in time, energy and position from the moment of generation till extraction or recombination.

Model used Miller-Abrahams expression to quantify the nearest-neighbor hopping rate of a charge carrier from an initial state i with energy E_i to a final state f with energy E_f:

$$\nu_{if} = \begin{cases} \nu_0 exp\left(-\dfrac{E_f - E_i \pm q\vec{r}_{if} \cdot \vec{F} + \Delta E_C}{k_B T}\right) = \nu_0 exp\left(-\dfrac{\Delta E}{k_B T}\right) & (\Delta E > 0) \\ \nu_0 & (\Delta E \leq 0) \end{cases} \quad (50)$$

where F is the external electric field, r_{if} – the vector connecting initial and final states, ν_0 – the attempt frequency and ΔE_C is the change in Coulomb energy. ± sign refers to electron *(+)* or hole *(-)* hopping. Site energies E_i as well as HOMO and LUMO energies are drawn from a Gaussian distribution and are assumed to be uncorrelated. The driving force for charge transfer is implemented via an on-site electron-hole repulsion with a magnitude that equals the LUMO level offset $\Delta E^{LUMO} = E^{LUMO}_{donor} - E^{LUMO}_{acceptor}$ between donor and acceptor.

Exciton diffusion by the Förster resonant energy transfer (FRET) mechanism is accounted for by the transition rate:

$$\nu^F_{if} = \nu_{ex}\left(\frac{R_0}{r_{if}}\right)^6 \Theta\left(E^{ex}_i - E^{ex}_f\right) \quad (51)$$

where R_0 is the Förster radius, ν_{ex} – the radiative exciton decay rate, Θ – the Heaviside step function and E^{ex}_i, E^{ex}_f the exciton energies at the initial and final sites. Dexter-type diffusion is implicitly accounted for as a double charge hopping process.

The waiting time before an event (hop or recombination) occurs is calculated as:

$$\tau = -\frac{\ln(r)}{\Sigma_\nu} \quad (52)$$

where r is a random number drawn from a homogeneous distribution between 0 and 1 and Σ_ν is the sum of the rates of all possible events. The event that occurs after τ is selected randomly, using the rates of all possible events as weight factors. Energies, rates, and waiting time are recalculated after each event.

Periodic boundary conditions in the x,y-directions were applied for both charge motion and Coulomb interactions; contact laying in the z-plane were implemented as perfect sinks. Independence of the results on the box size used in the calculations was assured.

Presented Kinetic Monte-Carlo model was developed in the research group led by Olle Inganäs in Linkoping University. All of the simulations presented here were carried out by Armantas Melianas.

4.6.3. Stochastic Schrödinger equation

Employing stochastic Schrödinger equation enables one to cover the void left by Kinetic Monte-Carlo model – ultrafast charge separation at the donor-acceptor interface. As is the case with exciton migration (described in chapter 2.2), initially transferred charge propagates coherently only to transition into incoherent hopping via interactions with the surrounding medium. Although Kinetic Monte-Carlo model describes charge transport via hopping quite well, it falls short when confronted with the coherent electron migration. To elucidate the role of electron delocalization and coherence in charge separation a full quantum mechanical description is necessary. The use of stochastic Schrödinger equation (SSE) allows one to evaluate the interplay between coherent dynamics and bath induced dephasing [105] and predict the importance of delocalization in systems with a wide range of intermolecular couplings – leading to different charge separation scenarios.

The model based on SSE and all of the calculations presented here were developed by V. Abramavicius and D. Abramavicius. The calculations were performed as follows. The acceptor medium with the donor site is described as a quantum system characterized by the lattice Hamiltonian:

$$\hat{H}_S = \sum_{n=1}^{N} \varepsilon_n |n\rangle\langle n| + \sum_{n\neq m}^{N} J_{nm} |n\rangle\langle m| \tag{53}$$

where ε_n is the electron energy on the n^{th} site and J_{nm} is the electron hopping energy between sites n and m (only one-particle states are included), state $|n\rangle$ denotes the electron on site n. The environment (heat bath) consists of harmonic oscillators:

$$\hat{H}_B = \sum_j \omega_j \hat{a}_j^\dagger \hat{a}_j \tag{54}$$

where ω_j is the frequency of the j^{th} oscillator, $\hat{a}_j^\dagger$ and $\hat{a}_j$ are the bosonic creation and annihilation operators (respectively) of j^{th} bath mode and $\hbar = 1$. Only linear coupling between the system and the environment is assumed.

The model is implemented on a 3D cubic lattice of 8×16×16 sites (figure 4.8) which corresponds to the expected size of a PCBM aggregate in a well intermixed BHJ solar cell active layer.[106] Each site (molecule) of the acceptor can be free or occupied by an electron. The CT state is obtained when the electron is transferred from the donor to the neighbouring acceptor site. The

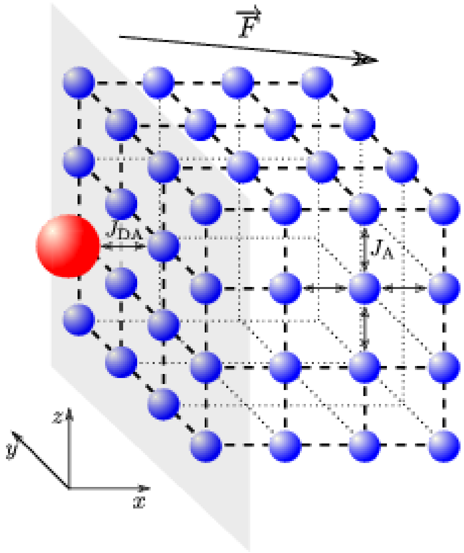

Figure 4.8 Schematic of the donor - acceptor interface model. Red sphere denotes the donor site; blue spheres denote the acceptor sites; F denotes the arbitrary direction of the external electric field; J_{DA} and J_A denote the interaction energies between the donor and the nearest acceptor site and between the nearest neighbor acceptor sites respectively.

donor site remains occupied by a hole at all times and thus only serves as the source of the electrostatic Coulomb field and the electron is described quantum mechanically using the SSE.

The donor/acceptor interface is characterized by the lattice constant a, the molecular dimension parameter b (in the Coulomb potential expression), the interaction energies between sites J_{DA} and J_A, the donor site excitation energy ε_D, the disorder σ and the system – bath coupling strength λ. However, we point out that absolute values of these parameters, such as for example the energetic disorder of the PCBM phase, are model dependent. In addition, the overall size of the lattice could be variable due to the complexity of interfacial domains at hierarchical morphologies of the blend. Differences in morphologies were mostly accounted for by a variation of couplings between the acceptor sites.

5. Investigated materials and devices

A total of five types of solar cells based on different active layer blends were investigated in order to capture the full picture of charge migration in BHJ devices. Device fabrication for the experiments presented in each chapter is described below. Full names of materials used in active layers, as interface materials, electrodes or as additives are:

$PC_{61}BM$
[6,6]-phenyl-C61-butyric acid methyl ester

$PC_{71}BM$
[6,6]-phenyl-C71-butyric acid methyl ester

N2200
poly(N,N’-bis(2-octyldodecyl)naphthalene-1,4,5,8-bis(dicarboximide)-2,6-diyl-alt-2,2’-bithiophene-5,5’-diyl)

P3TI
Poly[N,N′-bis(2-hexyldecyl)isoindigo-6,6′-diyl-alt-thiophene-2,5-diyl]

APFO3
poly[2,7-(9-di-octyl-fluorene)-alt-5,5-(4’,7’-di-2-thienyl-2’,1’,3’-benzothidiazole)]

TQ1
poly[2,3-bis-(3-octyloxyphenyl)quinoxaline-5,8-diyl-alt-thiophene-2,5-diyl]

PTB7
poly[[4,8-bis[(2-ethylhexyl)oxy]benzo[1,2-b:4,5-b’]dithiophene-2,6-diyl][3-fluoro-2-[(2-ethylhexyl)carbonyl]thieno[3,4-b]thiophenediyl]]

DIO
1,8-Diiodooctane

PFPA-1
poly(3,30-([(90,90-dioctyl-9H,90H-[2,20-bifluorene]-9,9-diyl)bis(4,1-phenylene)]bis(oxy))bis(N,N-dimethylpropan-1-amine))

PEDOT:PSS
poly(3,4-ethylenedioxythiophene) poly(styrenesulfonate)

CHAPTER 6 – ELECTRON TRANSFER AT ORGANIC INTERFACES

A monolayer of PFPA-1 interface material was deposited on ITO coated glass substrates that were TL-1 treated. P3TI and $PC_{71}BM$ (D/A 2:3 w/w) were then spin-coated from a 20 g/l o-dichlorobenzene (ODCB) solution with 2.5% (vol. %) of DIO. The thickness of the active layer (≈ 70 nm ± 10 nm) was determined by a Dektak surface profilometer. PEDOT:PSS PH1000 with a layer thickness of 110 nm was deposited from an aqueous solution mixed with 5% (vol. %) of dimethyl sulfoxide and 0.5% (vol. %) Zonyl® FS-300 as the surfactant, and then annealed at 60 °C to remove residual water. The device was then encapsulated by a glass lid.

CHAPTER 7 – INFLUENCE OF DONOR-ACCEPTOR RATIO ON CHARGE GENERATION AND EXTRACTION

Fabrication of the inverted solar cells has been previously described elsewhere,[107] therefore only a brief account is given here. An aluminum electrode was evaporated onto a clean glass substrate followed by a titanium layer, which was then exposed to air for 12 h to form TiO_x. The active layer was spin-coated on top of the Al/TiO_x bilayer cathode from a solution of either the polyfluorene copolymer APFO3, $PC_{61}BM$, or the APFO3:$PC_{61}BM$ blends of composition ratios 2:1, 1:1, and 1:4 (by weight). The anode electrode, PEDOT-PSS PH1000, was deposited on top of the active layer followed by the encapsulation of the cell with a glass cover. The thickness of the active layer was ≈ 100 nm, and the active area of the solar cells was ≈ 5 mm^2.

CHAPTER 8 – TIME DEPENDENT MOBILITY IN OPVS

Samples were fabricated inside a N_2-filled glovebox and encapsulated with epoxy glue. Samples were measured outside the glovebox in an ambient environment. BHJ active layer was spin-coated at the same settings as for the best-performing OPV devices: active layers of TQ1:$PC_{71}BM$ [108] (1:2.5 ratio by weight) were spin-coated from a 25 g/L (total) 1,2-dichlorobenzene solution yielding an active layer thickness of 70 nm, whereas active layers of TQ1:2200

(2:1 ratio by weight) were spin-coated from a 9 g/L (total) chloroform solution and then annealed for 10 min at 120 °C before top electrode deposition, yielding an active layer thickness of 85 nm. Time-resolved experiments were carried out on devices in inverted geometry: on semitransparent ITO/PFPA-1/TQ1:$PC_{71}BM$/PEDOT:PSS (Clevios PH1000) devices for TQ1:$PC_{71}BM$, and ITO/ZnO/TQ1:N2200/MoO3/Al for TQ1:N2200. Detailed information on OPV device preparation can be found elsewhere.[109,110] The neat TQ1 film for photo-CELIV measurements was blade-coated from an ODCB solution. Electron-only devices were fabricated in the following geometry: Al/TiO_x/TQ1:$PC_{71}BM$/LiF/Al, hole-only devices: ITO/PEDOT:PSS/TQ1:$PC_{71}BM$/PEDOT:PSS (PH1000). Active layers were spin-coated using identical settings as for the solar cell device.

CHAPTER 9 – INFLUENCE OF ACTIVE LAYER OPTIMIZATION

PTB7 and fullerene were dissolved in chlorobenzene (HPLC grade from Sigma Aldrich) at the ratios of 90:10, 40:60, 20:80 and 10:90 by weight and stirred at 50° C for 4-5 hours. These blends will be called [P90:F10], [P40:F60], [P20:F8] and [P10:F90], respectively, where the first number denotes the relative amount of the polymer. For the samples prepared with DIO, 3% of it by volume was added to the solution which was then stirred for a further 5 min. The blends were spin-coated on a ≈ 40 nm layer of PEDOT:PSS which was spin-coated on an indium-tin oxide coated glass substrate. The thickness of the PTB7:fullerene layer was ≈ 115 nm. The layers of calcium (≈ 20 nm) and aluminium (≈ 100 nm) were subsequently deposited by vacuum sublimation. The structure was encapsulated with a glass coverslip and epoxy.

6. Electron transfer at organic interfaces

Let's now consider the last steps in the chain of photo-physical processes leading to free charge generation in organic solar cells – charge transfer at organic interfaces. As was briefly mentioned in chapter 2.3 charge transfer occurs on picosecond time scale [111] – considerably faster than competing radiative and nonradiative recombination processes thus resulting in quantum efficiency close to 100%. Although several often-conflicting models have been proposed, to this day it remains unclear what kind of mechanism is responsible for high charge separation efficiencies in organic heterojunctions.

Some of the explanations suggested for this initial dissociation stage are: charge carrier delocalization over several polymer segments and/or fullerene molecules,[112] hot interfacial charge-transfer states with delocalized wave functions,[74,113] or, alternatively, with electron and/or hole wavefunctions localized on molecules situated at larger distances from the interface.[114] Recently, a partially coherent model, assuming electron delocalization over the entire aggregated fullerene domain,[66] and a hybrid model of a 1D polymer/fullerene lattice with semi-classical dynamics at short time scales and Redfield relaxation theory at long time scales,[115] have been proposed. Overall, charge separation on an ultrafast time scale is often considered to be predominantly coherent. However, carrier delocalization and coherent propagation, their extent and temporal evolution have only been qualitatively postulated. Although the later time scales of charge separation have been successfully described by incoherent hopping,[116] a consistent model at the earliest time scales, describing the coherent propagation of charge and the gradual transition into the classical hopping regime, is still absent.

To elucidate the role of delocalization and coherence in charge separation a full quantum mechanical description is necessary. In this chapter, the study of initial charge separation using TREFISH technique (described in detail in section 4.5.2) in combination with stochastic Schrödinger equation (described in detail in section 4.6.3) is presented. The sub-ps time resolution of the experiment enabled the calibration of the presented model. It is important to point out that current model does not include recombination, which although considered insignificant in efficient OSC systems, limits their efficiency. The extent of electron delocalization, as illustrated here, may be one of the key factors minimizing geminate recombination.[117]

6.1. Charge separation dynamics

Figure 6.1 shows the experimentally determined kinetic of the charge carrier drift distance after photo-excitation of the P3TI:$PC_{71}BM$ sample. This system is of particular interest due its high internal quantum efficiency (IQE) of 90% despite its exceptionally low charge separation driving force ΔE of approximately 0.1 eV.[106] The initial part of the transient (0-3 ns) was determined by the TREFISH technique, whereas the latter part of the kinetic (3-10000 ns) was determined by a transient photocurrent measurement with a high load (integrated photocurrent). Charge carrier separation distance along the direction of the applied electric field equals to the sum of electron and hole drift distances, thus full extraction corresponds to half of the sample thickness, i.e. 35nm in figure 6.1.

An immediately noticeable feature of the charge extraction kinetic is the two-step like function over time. Considering the fact that the first part of the measured charge extraction dynamics constitutes approximately half of the overall signal, in light of the known electron mobility in PCBM [118,119] and hole mobility in P3TI values,[120] it is reasonable to assume that the initial part of the kinetic is governed by the fast motion of the electrons. The latter part then would be attributed to the extraction of holes. Indeed, such distinction of the charge extraction is a compelling result in and of itself and thus will be addressed in much more detail in chapter 7.

For the current discussion, however, initial part of the charge separation is of the utmost importance. Thus, the first 100 ps after the photoexcitation (red shade in figure 6.1) were measured with the highest resolution and the trace is shown in

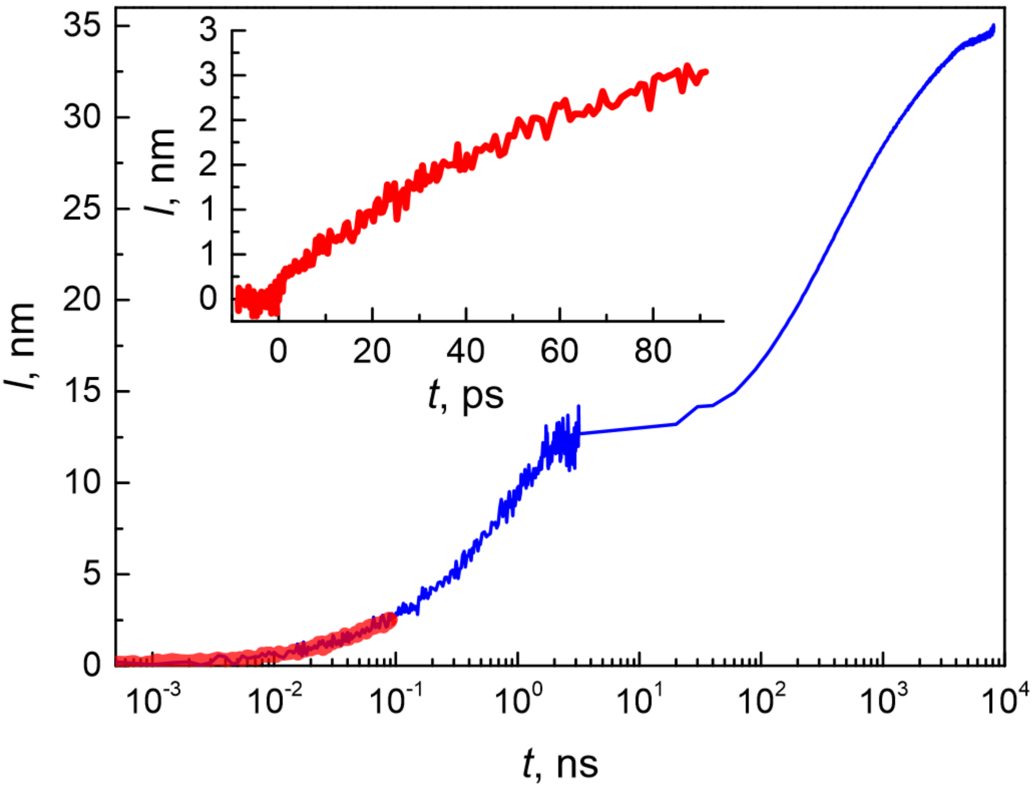

Figure 6.1 Time dependence of the average carrier drift distance at an electric field of $F = 5.7 \times 10^5$ V/cm. Inset shows the initial 100 ps of the kinetic which were measured with better accuracy and used as the basis for the model.

the inset of figure 6.1 (note the linear time scale as opposed to the log-scale in the main figure). Transient absorption measurements (not shown) indicated ultrafast < 100 fs photo-induced charge transfer with no signatures of delayed charge transfer due to exciton diffusion. Thus, the measured TREFISH data directly monitors the motion of the photogenerated charges away from the donor-acceptor interface.

6.2. SSE modeling

It has been recently experimentally demonstrated that mainly electron motion in PCBM is responsible for the initial evolution of the charge separation process – hole motion is significantly slower,[66,118–120] in agreement with the results of previous chapter. Thus holes can be considered immobile as was indeed done in this case. In order to model photo-excitation in the donor phase, both the electron and the hole were initially placed at the donor site in the simulation space (figure 4.8) and the electron was then allowed to propagate in the electrostatic field of the hole. Simulation parameters were chosen as those typical for polymer-PCBM systems: driving force $\Delta E = 0.1\ eV$ for P3TI:PC$_{71}$BM, CT exciton binding energy $\varepsilon_{CT} = -0.27\ eV$, and the energetic disorder σ of PCBM was set equal to $\sigma = 75\ meV$, corresponding to the experimentally determined value in [121] and J_{DA} is set equal to 12.5 meV leading to an electron transfer time of 100 fs, in agreement with experimental transient absorption data (not shown). The lattice constant was set to be equal to 1 nm. However, it was noticed that the most important parameter governing the dynamics of the electron is the inter-acceptor coupling J_A. Variations of other parameters: donor site excitation energy ε_D, CT state energy ε_{CT}, donor-acceptor interaction energy J_{DA} and system-bath interaction energy λ only slightly affect the evolution of the system. Hence, parameters were kept fixed in most cases presented, except for the inter-acceptor coupling J_A, which was varied.

Figure 6.2 shows the simulated temporal evolution of electron density perpendicular to the interface for the indicated values of inter-acceptor electron coupling J_A. External electric field was not applied in order to highlight the effects of delocalization. Results show that the electron is transferred from the donor site to a nearby pool of coherently coupled acceptor sites within ≈ 300 fs. The number of accessible sites in a given time interval grows with increasing intermolecular (inter-acceptor) coupling, allowing for the electron to transfer to more distant sites already at very early times. Electron transfer is quantitatively characterized in the rightmost column of fig. 6.2 where the kinetics of the absolute e-h separation distance, $d_{abs}(t)$ (fig. 6.2 red traces) and the electron delocalization radius, $I(t)$ (fig. 6.2 black traces), are shown. The extent of electron delocalization is also indicated by the blue circles. These results only weakly depend on the donor excitation energy ε_D, in agreement with experimental studies of charge separation efficiency versus excitation energy.[122]

The kinetics of both $d_{abs}(t)$ and $I(t)$, for different J_A exhibit a similarly rapid initial rise. For very weak coupling both electron delocalization and initial electron transfer distance are small, and thus the electron is only transferred from the donor to the nearest acceptor site. For intermediate coupling the initial transfer distance is increased and the electron is more, although still weakly, delocalized. In this regime at times > 500 fs the average electron distance increases while its delocalization remains constant. In case of strong coupling, the electron is strongly delocalized, resulting in the largest electron transfer distance at early times, whereas the later part of the transfer process is mainly determined by time-dependent localization. Note that for strong couplings electron delocalization is confined by the size of the acceptor lattice in the model, chosen to correspond to the expected PCBM domain size ($8 \times 16 \times 16$ nm^3). Despite similar probability distributions at long times in the second and third rows of figure 6.2, the extent of delocalization of individual electrons and, consequently, the character of their motion is very different.

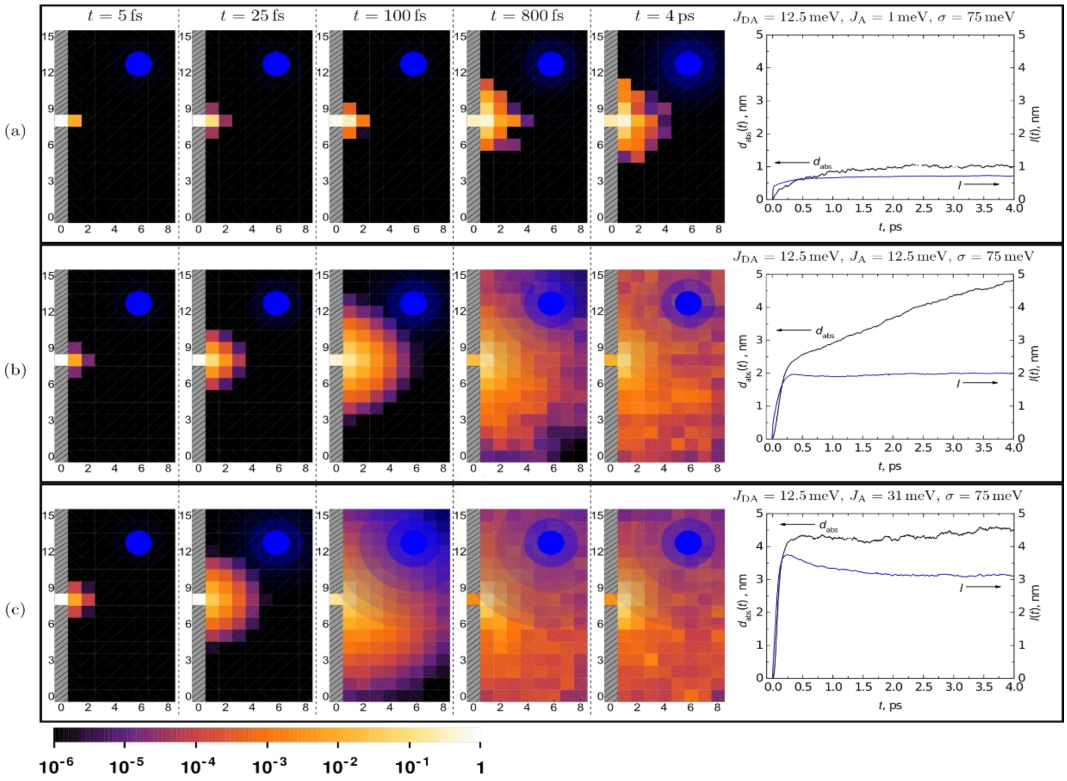

Figure 6.2 Ensemble-averaged evolution of electron probability density in the plane perpendicular to the interface of donor (grey area) and (16 x 16 x 8) nm^3 acceptor domain at different times following photoexcitation for the indicated values of inter-acceptor coupling J_A. The rightmost column shows the corresponding absolute charge separation distance d_{abs} (red traces) and delocalization radii I (black traces). Filled blue circles illustrate the extent of electron coherence at a given time.

6.3. Assessment of the model

To determine which regime corresponds to real polymer-PCBM blends, model predictions were compared to experimentally measured carrier drift dynamics of P3TI-PC$_{71}$BM solar cell. Figure 6.3 shows the experimental and simulated average e-h separation along the direction of the electric field of 5.7×10^5 V/cm, created by applied voltage and the built-in field of the OSC. The experiment shows a fast ≈ 500 fs initial rise to a distance of 0.4 nm. The later part of the process is considerably slower – charge separation distance gradually rises up to 0.9 nm in 3.5 ps.

In order to replicate the experiment conditions, external electric field was added to the model. The random orientation of the heterojunction with respect to the applied field was accounted for by performing multiple simulations with a randomly oriented electric field and averaging the obtained e-h separation

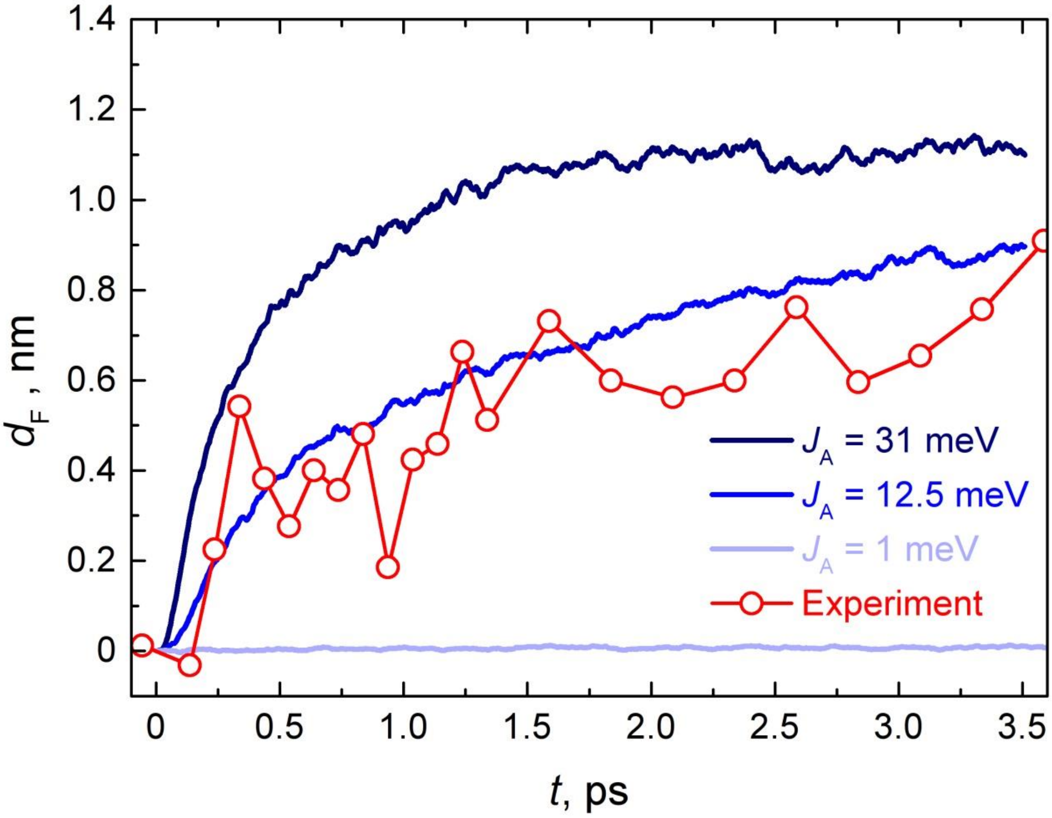

Figure 6.3 Time dependence of the charge separation distance d_F along the direction of the electric field F of 5.7×10^5 V/cm for the indicated inter-acceptor coupling values J_A. Symbols - experiment, solid colored lines – simulations at different values of J_A.

distance projected along the direction of the field. The model reproduces the experiment with J_A = 12.5 meV (intermediate coupling) (see fig. 6.3) which corresponds to an absolute carrier separation distance of 2.5 nm in 500 fs as shown in fig. 6.2. It is considerably smaller than the 4 nm distance evaluated in [66] for PCDTBT-PC$_{61}$BM. The later corresponds to the model prediction in the strong coupling regime where carrier separation distance of 4 nm is obtained (Fig. 6.2c). However, at least for the case of P3TI-PC$_{71}$BM, comparison with the experiment indicates that such coupling and initial separation are overestimated. Given that P3TI-PC$_{71}$BM operates at an IQE of 90%, intermediate couplings, leading to electron delocalization over two lattice sites (fig. 6.2), are already sufficient to facilitate efficient charge separation at organic interfaces.

To further support model results electron mobilities were calculated using the same set of parameters. The obtained values are 0.03, 0.37 and 1.26 cm^{2}V^{-1}s^{-1} for J_A = 1, 12.5 and 31.5 meV respectively. The predicted mobility at J_A = 12.5 meV is in excellent agreement with the experimentally measured electron mobility value of 0.3 cm^{2}V^{-1}s^{-1} in PCBM at the ps time scale.[119]

6.4. Transition to incoherent transport

Initial part of the measured charge transfer in combination with the modeling results seem to indicate that coherent electron transfer lasts up to 500 fs and is responsible for shaping the “initial” electron-hole distance distribution. Following the coherent propagation stage charge separation kinetics gradually switch to the slower incoherent-hopping phase, as indicated by the two-phase evolution of separation distance (figure 6.3). Thus, 500 fs marks the transition from coherent electron propagation to incoherent hopping where the classical hopping models become valid. Figure 6.4 shows the temporal evolution of e-h distance distribution without external electric field in the intermediate coupling regime. The electron gets completely transferred from the donor site to the acceptor lattice in ≈ 800 fs, however, it is still strongly bound to the hole. According to Van Eersel,[123] further charge separation is facilitated by incoherent electron hopping. Considering the above in conjunction with previous work by

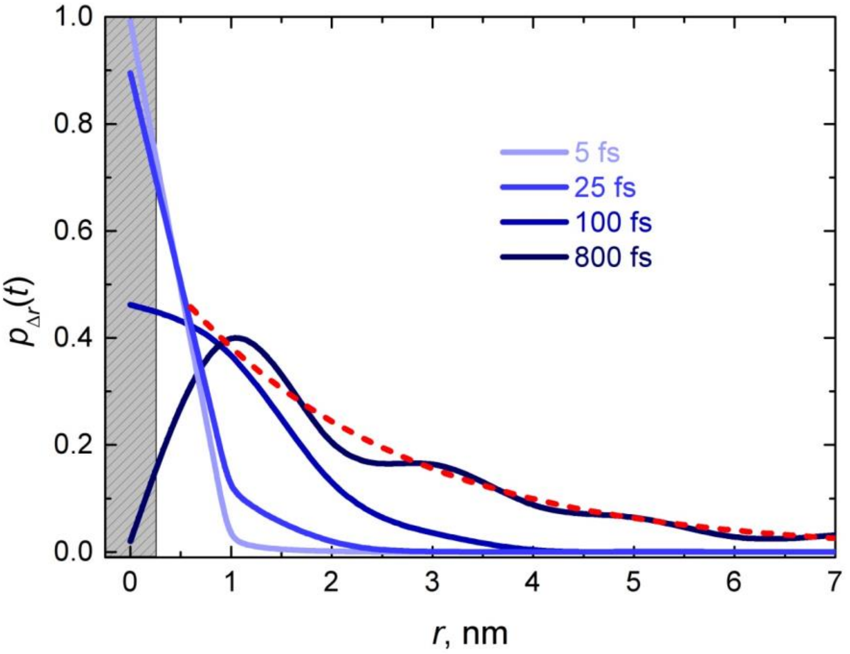

Figure 6.4 Radial distribution of e-h separation distance at early times. The position of the donor site is indicated by the shaded grey area. Dashed red line represents the exponential character of the e-h distance distribution after 800 fs.

D. H. K. Murthy et al.,[117] the 800 fs e-h distance distribution (which can be approximated as an exponential – red dashed line in fig. 6.4) could be used in classical hopping models as the initial distribution.

Although presented analysis is performed for charge separation at the heterojunction of a conjugated polymer and an aggregate of the fullerene derivative PCBM, results are also applicable to small molecule donors and pristine fullerenes.

7. Donor-Acceptor ratio significance

Whereas coherent electron propagation describes well the initial part of the charge migration, incoherent hopping is responsible for the majority of the distance covered by the photogenerated charges. Charge transport through the active layer and extraction at the electrodes constitutes a significant problem in solar cell optimization and has received profuse attention.[124] The key parameter for charge transport is, of course, mobility – it determines the time needed by the photo-generated charges to be extracted from the device by the effective electric field, and govern how fast electrons and holes meet to recombine.

The ability of holes to move rapidly through conjugated polymer chains was believed to be one of the major advantages of conjugated polymers over small molecules for their use in BHJ solar cells. However, efficiencies of solar cells based on various polymers and on small molecules are surprisingly similar, suggesting that polymer conjugation may not be that crucial for good solar cell performance. This leads to the conclusion that the large charge delocalization in conjugated polymers, which was previously believed to be of major importance for the charge carrier photo-generation, may not play a dominant role. On the other hand, attempts to substitute fullerene derivatives with other electron accepting molecules have been less successful. Moreover, high efficiency solar cells need a high fullerene content of 50% or more, significantly exceeding percolation threshold for the electron motion.[125] Many factors, such as dielectric permittivity, phase segregation, morphology, positions of electronic levels etc.,[126–128] may play an important role for the performance of the solar cell, but the electron mobility in the fullerene phase is apparently among the most important.

Charge carrier mobilities in conjugated polymers and fullerenes under equilibrium or near-equilibrium conditions have been widely investigated before. Hole mobilities were found to be of the order of 10^{-3}-10^{-6} cm^2/Vs in conjugated polymers,[129–132] while electron mobility in PCBM is higher, reported to be on the order of 10^{-2}-10^{-1} cm^2/Vs.[133–136] However, there are several problems with this approach: (a) mobilities determined for neat materials may be significantly different from those in BHJ blends, because of different molecule packing and of boundaries between polymer and fullerene domains, which may create major obstacles for the carrier motion; (b) mobilities measured in equilibrium conditions might not be applicable to the processes in operating solar cells on short time and distance scales – before carriers undergo relaxation; (c) conventional measurement techniques cannot distinguish between electron and hole mobilities in blended BHJ devices but rather give an average value, which might be misleading.

7.1. Photovoltaic performance

The photovoltaic performance of neat APFO3, neat $PC_{61}BM$ and APFO3:$PC_{61}BM$ solar cells under AM 1.5 illumination is characterized in table 7.1. The charge generation efficiency in neat polymer films at low light intensities and in the absence of applied electric field is known to be very low,[64,137] in agreement with the solar cell performance measured for a neat APFO3 cell. The low current density and open circuit voltage of a neat $PC_{61}BM$ device are due to the poor absorbance of $PC_{61}BM$ in the visible spectral region and apparently low carrier generation efficiency leading to very low charge concentration. Open circuit voltage and fill factors of the different blending ratio devices are rather comparable, which, according to [138] indicate that the built-in potential and charge recombination are not drastically different for different donor-acceptor ratios. Geminate recombination was also shown to be the dominating recombination process in APFO3:$PC_{61}BM$ films at low excitation

Table 7.1 Photovoltaic performance and modeled mobility parameters of different devices:

APFO3:$PC_{61}BM$ ratio in device	J_{sc} (mA/cm^2)	V_{oc} (V)	FF	PCE (%)	Modeled mobility [μ_0 (cm^2/Vs), α]	
					Electron	Hole
Neat APFO3	0.0998	0.757	0.243	0.018	1.1×10^{-5} , 0.25	5.5×10^{-6} , 0.2
2:1	2.28	0.818	0.355	0.662	8×10^{-9} , 0.5	4×10^{-6} , 0.25
1:1	4.28	0.894	0.318	1.22	2.5×10^{-6} , 0.35	4.3×10^{-9} , 0.6
1:4	4.91	0.878	0.374	1.61	4.5×10^{-5} , 0.3	3.8×10^{-8} , 0.45
Neat $PC_{61}BM$	0.171	0.301	0.40	0.021		

fluencies, and that its rate is quite independent of the blending ratio.[139] Current density in the APFO3:$PC_{61}BM$ cells increases with the blending ratio in the order (2:1) < (1:1) < (1:4) indicating improved charge transport.[138]

7.2. Electric field dynamics

Underlying processes of the observed cell performance trends can be better understood from the results of TREFISH and IPC measurements (described in more detail in sections 4.5.1 and 4.5.2). Figure 7.1 shows the electric field dynamics caused by the photo-generated charges in neat APFO3 and blend films, normalized to the total voltage drop at long times when all charge carries were extracted. Assuming homogeneous charge generation across the thickness of the sample, the normalized voltage drop at some particular delay time approximately gives the fraction of extracted charge carriers at this time. It should be noted that much higher excitation fluence was used for the neat APFO3 film than for all the blends, because of lower carrier generation efficiency. The electric field kinetics for the APFO3 device is similar to what has been observed previously for other conjugated polymers and it has contributions from both excitons and mobile charges.[94] The exciton contribution is the very fast resolution-limited voltage drop at zero delay time (see inset in figure 7.1) caused by the increased polarizability of the polymer chains in the excited state, which decays with the exciton lifetime of 175 ps.[140] The relative amplitude of the exciton contribution depends on the carrier generation efficiency. Given that the exciton contribution disappears on a sub-nanosecond time scale, the ensuing dynamics is mainly due to the motion of charges. Almost half of charge carriers are extracted during first 3 ns, while extraction of the remaining half takes hundreds of nanoseconds.

APFO3 is an ambipolar material with comparable steady-state electron and hole mobilities.[141] On the ps to sub-ns time scale the THz conductivity is, however, dominated by hole mobility.[142] Thus it is reasonable to conclude that holes on the polymer contribute significantly to the photocurrent on this time scale, but the exact ratio of electron and hole contribution, or their time dependencies cannot be derived.

No ultrafast exciton-related field response was observed for all blend devices (see inset in figure 7.1), which confirms ultrafast exciton dissociation leading to efficient quenching of the polymer excited states and formation of randomly oriented charge pair (CP) states.[139] The absence of an ultrafast response also indicates that the polarizability of the CP state is relatively low, which may be interpreted as an indication of weak electron and hole delocalization in these blends.

The time evolution of the field strength in the (2:1) device is slightly slower than that in the neat APFO3 film both on sub-nanosecond and sub-microsecond time scales suggesting that both electron and hole mobilities are slightly lower. Decrease in the hole mobility may be expected because of the presence of $PC_{61}BM$ domains, which perturb the hole motion. Electron transport properties

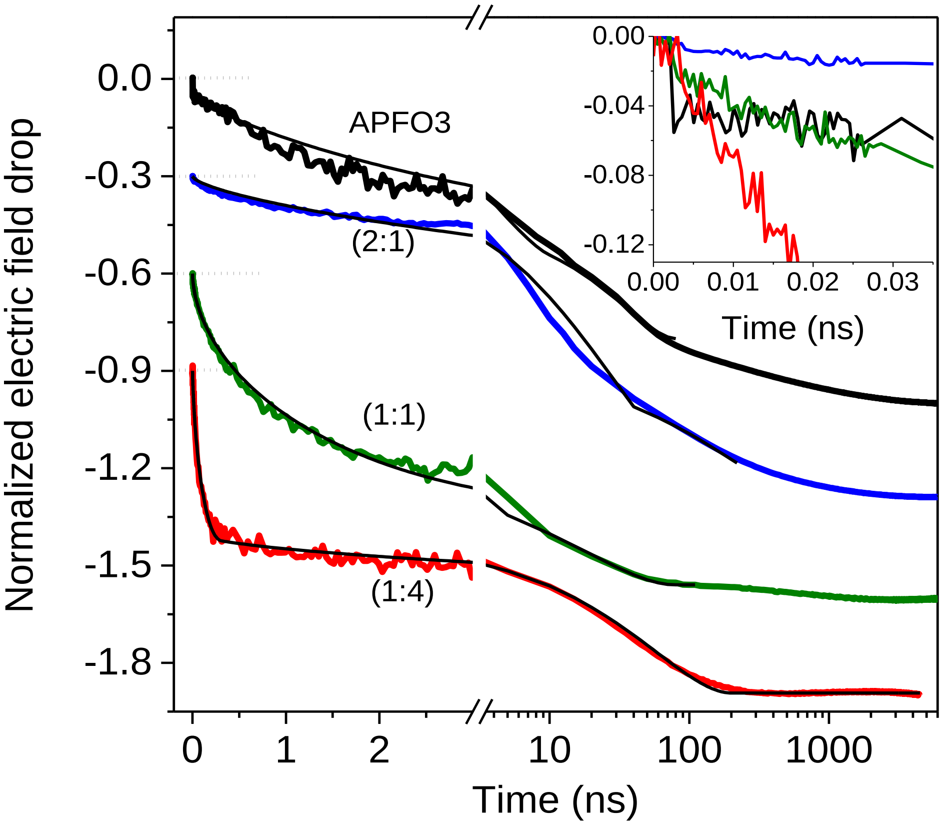

Figure 7.1 Normalized electric field kinetics of different blending ratio APFO3:$PC_{61}BM$ cells and of the neat APFO3 film (the curves are vertically shifted). The cells were reverse biased at 4 V. Thin black lines show modeled kinetics. The inset shows the initial part of the kinetics, revealing the exciton contribution in neat polymer film.

in the blend are expected to be significantly different from that in pure polymer since electrons now are transported over the $PC_{61}BM$ domains. Electron mobility in $PC_{61}BM$ is quite high, on the order of 10^{-2}-10^{-1} cm^2/Vs.[133–136] Simple estimates show that with such a mobility, electron extraction should take place on a sub-nanosecond time scale suggesting that the initial field dynamics should be attributed to electrons. However, the electron mobility in blends may be significantly lower, particularly at low $PC_{61}BM$ content when $PC_{61}BM$ molecules are dispersed in the polymer matrix or form small weakly percolating clusters. The percolation threshold depends on particle shape and appears at a concentration of about 20% $PC_{61}BM$.[125] Thus, the 33% $PC_{61}BM$ concentration in the (2:1) blend should be sufficient for percolation, but the presence of isolated single $PC_{61}BM$ molecules, or weakly percolating clusters, which may act as electron traps reducing their mobility cannot be excluded. For these reasons assignment of the time dependent field dynamics in the (2:1) device is not straightforward, but similarly to neat APFO3 polymer sub-ns dynamics have significant contribution from hole extraction and both holes and electrons contribute to the slower time scale.

The electric field kinetics are much faster in the (1:1) blend. Both $PC_{61}BM$ and polymer concentrations in this blend should be sufficient for extensive percolation between $PC_{61}BM$ and polymer domains, leading to high mobilities of both electrons and holes. Assuming that the hole mobility in the (1:1) blend decreases or remains similar to that in the (2:1) blend, the increase in the amplitude of the fast (<3 ns) field drop can be attributed to electrons. Almost all remaining charge carriers, are extracted during less than 30 ns, indicating that the carrier extraction from this sample is close to balanced. The presence of a weak tens to hundreds of nanoseconds decay component, indicates that some low concentration of trapped carriers are present.

By further increasing the $PC_{61}BM$ concentration, large percolating $PC_{61}BM$ clusters are formed and the electron mobility is expected to increase even more, approaching that observed in neat $PC_{61}BM$ films or crystals. The hole mobility, on the other hand, is expected to decrease even further. The time evolution of the electric field strength in the (1:4) device is consistent with these expectations and shows a strong and rapid decay on the tens and hundreds of ps time scale; a similar ultrafast electric field drop on the tens of ps time scale was observed in

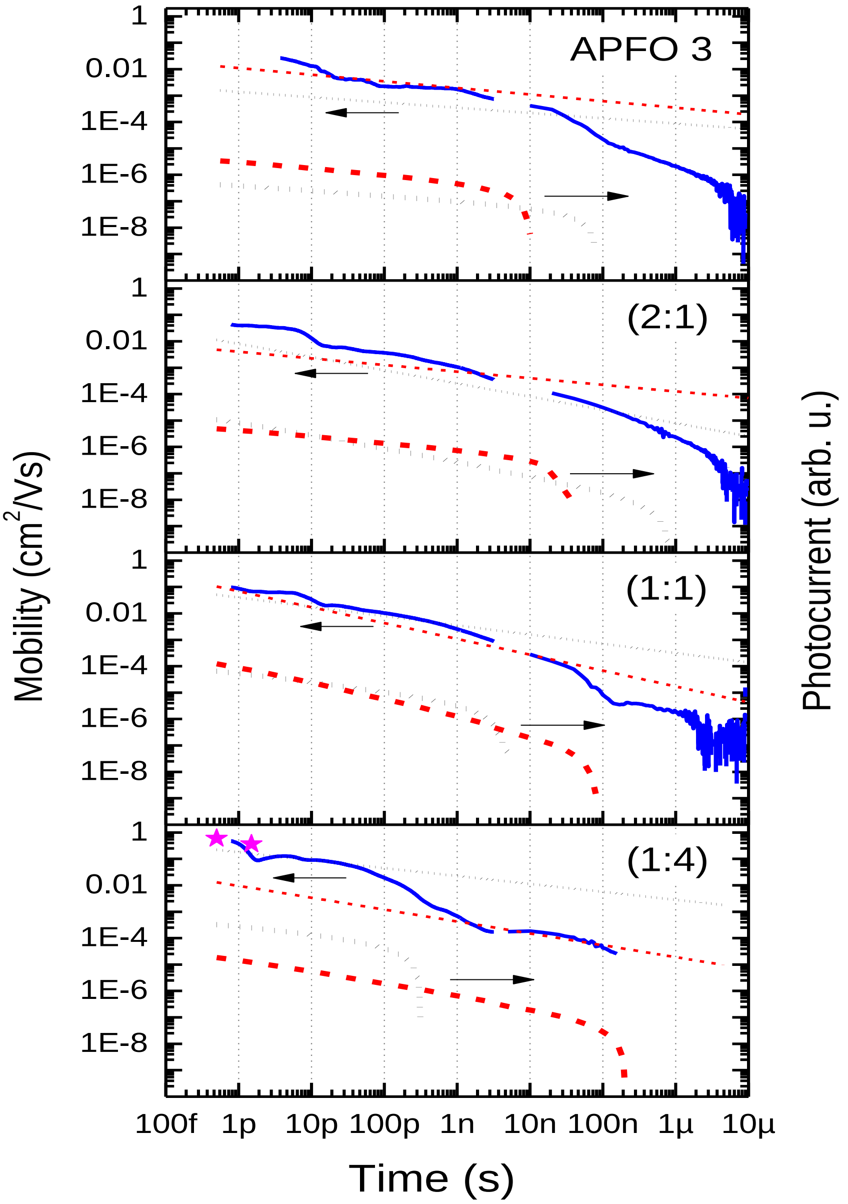

Figure 7.2 Experimentally measured average carrier mobility kinetics at 4 V applied voltage ($E \approx 4.8 \cdot 10^5$ V/cm) in neat APFO3 and in blends with different blending ratio (solid blue curves). Red stars show average carrier mobility of (1:4) device obtained from terahertz spectroscopy measurements.[138] Dashed lines show modeling results. Thin dashed black and red lines are electron and hole mobilities, respectively, while corresponding thick lines show electron and hole photocurrents.

neat $PC_{61}BM$.[118] Therefore, the extraction of about 50% of the charge carriers from the (1:4) blend within 1 ns can be quite confidently related to the fast electron motion. The final carrier extraction from this device is about two times slower compared to the cell with equal donor-acceptor concentrations, most likely as a consequence of lower hole mobility at the low (20%) polymer concentration.

7.3. Electron and hole contributions to photocurrent

In order to better characterise the electron and hole transport, field dynamics have been modelled by approximating electron and hole mobilities by power-law functions $\mu(t) = \mu_0 t^{-\alpha}$, typical for carrier mobilities in disordered materials.[141] Thin lines in figure 7.1 show the calculated electric field kinetics and figure 7.2 presents photocurrents created by the two types of carriers as well as their calculated mobilities. Quite good agreement between experimental and calculated electric field kinetics show that this approach is indeed valid, although slightly lower modelled mobilities on the picosecond time scale (figure 7.2) show that the power-law functions cannot describe the fine details of the initial mobility decay.

The bending points of the current curves in figure 7.2 indicate the end of carrier extraction. It is clear, especially for (1:4) sample, that electrons and holes exhibit different dynamics – one type of charge carrier extraction is more than 100 times faster than that of the opposite sign. Increase in the electron mobility and decrease in the hole mobility in devices with higher $PC_{61}BM$ concentration was indeed expected as discussed above. Results of the time-dependent mobility modelling supports this expectation and allows the attribution of black curves to electrons and red curves to holes. This assignment is also in agreement with the carrier extraction in pure polymer: the hole extraction time is slightly shorter than in blends while electron extraction is several times slower, in agreement with 5 times higher steady state hole mobility.[141] Consequently, the hole extraction slows down several times when $PC_{61}BM$ concentration increases. This weak dependence is a consequence of good percolation on long polymer chains, even at low polymer concentration. The electron extraction rate, on the contrary, changes by almost four orders of magnitude in going from the (2:1) to the (1:4) blend. Electron mobility at 80% $PC_{61}BM$ concentration in the (1:4) blend approaches that in pure $PC_{61}BM$, while at low concentration the electron mobility is apparently determined by spatial traps formed by single $PC_{61}BM$ molecules or weakly percolating domains, drastically reducing electron mobility. Additional reasons for the lower hole sensitivity to stoichiometry can probably be found in the smaller variation of hole mobility in polymer than of electron mobility in $PC_{61}BM$ upon going from isolated molecules to neat phase. In the amorphous APFO3 polymer, hole transport between chains is characterized by significant potential barriers implying that it does not increase as dramatically

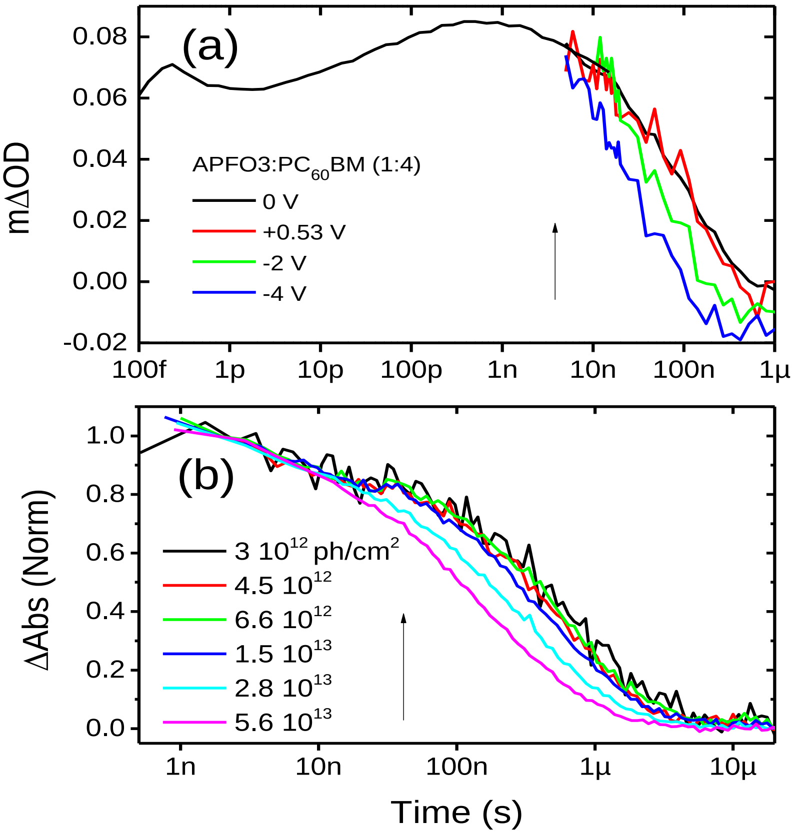

Figure 7.3 **(a)** Transient absorption of a (1:4) blend device at short circuit (0 V) condition (black) and at forward (+) and reverse (-) biases. The negative TA signal at long times under applied field is due to the extraction of equilibrium carriers. **(b)** Transient absorption of (1:1) blend at different excitation photon densities. Excitation was performed at 532 nm by 1 ns duration pulses.

as the electron mobility going from single fullerene molecule to crystalline $PC_{61}BM$ domains.

The relatively slow, of about a hundred ns, hole extraction in the (1:4) blend is supported by the transient absorption (TA) kinetics shown in figure 7.3a. At 900 nm the TA signal is due to absorption of holes,[66] which at zero applied field have fully decayed through recombination by 1 µs, while at applied voltage the decay was faster because of the hole extraction. TA kinetics during initial 10 ns were independent of the applied voltage. According to the previous investigations the non-geminate recombination in APFO3:$PC_{61}BM$ films is negligible on a ps-ns time scale, below an excitation intensity of about 10^{13} photon/cm^2.[138] Intensity dependence of the recombination dynamic on a longer time scale is shown in figure 7.3b. The increase of the recombination rate due to non-geminate recombination becomes apparent only at $1.5\cdot10^{13}$ photon/cm^2 i.e. at an excitation intensity one order of magnitude higher than used in the present investigations. The influence of the non-geminate recombination at applied voltage is in addition expected to be lower than under the field-free conditions of figure 7.3b, because of faster carrier extractions. Thus, non-geminate recombination can be safely neglected in the data analysis for the present materials, under the experimental conditions used. Consequently, the hole decay at zero applied field should be attributed to the geminate recombination. The carrier decay time decreases to tens of nanoseconds at 4 V applied voltage (figure 7.3b) as a result of charge extraction, in perfect agreement with the charge extraction kinetics of figure 7.1. This confirms that the slow charge extraction phase on the tens of ns time scale in the electric field kinetics of the (1:4) blend device (figure 7.2) is indeed due to hole extraction.

7.4. Traps in weakly percolating devices

Figure 7.4 shows the voltage dynamics at longer times measured at different applied voltages by an oscilloscope. The observed voltage drop increases with the applied voltage, and the increase is particularly strong for the (2:1) device indicating that efficient carrier generation or extraction requires strong electric field. In contrast, carrier extraction from the (1:4) device at 4 V is only about twice as large as at the build-in electric field. Kinetics in figure 7.4 become progressively faster at higher voltages; this is particularly clear in case of the (1:1) sample, transients of the other two samples show much weaker dependences on the applied voltage. Such behaviour can be interpreted as an indication that the carrier extraction in the (2:1) device on tens and hundreds of ns time scale is governed by thermal release of electrons from traps, in agreement with the conclusion above that a fraction of electrons in the (2:1) sample and holes in the (1:4) sample are trapped in weakly percolating PC$_{61}$BM or polymer clusters. Only in case of the sample with equal parts of APFO3 and

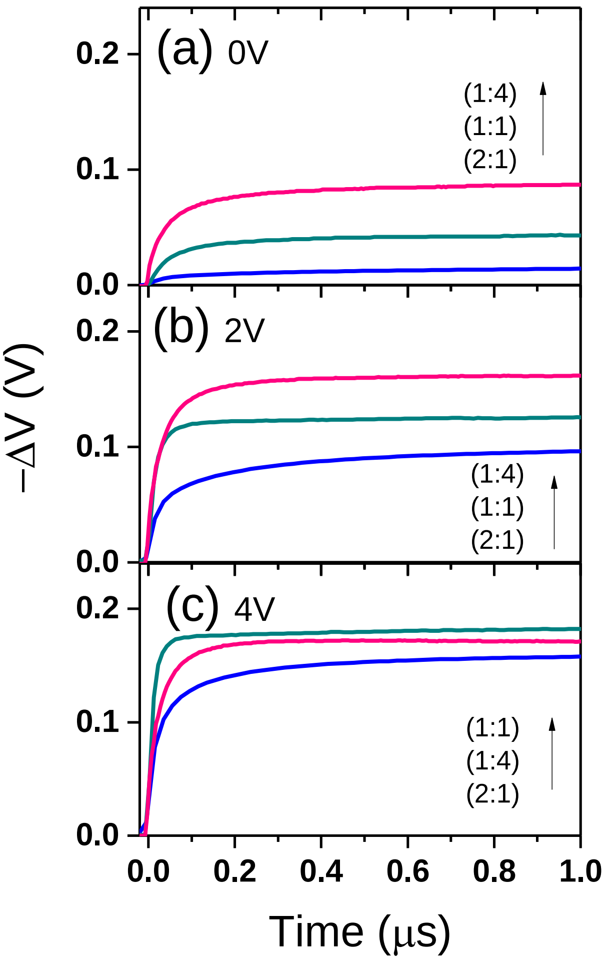

Figure 7.4 Transient voltage kinetics on different stoichiometry devices at different applied voltages. The transient voltage was corrected for the equal number of absorbed photons.

$PC_{61}BM$ (1:1), where percolative motion of both carrier types is optimized (for this material), the extraction rate significantly increases with the applied voltage, which is expected if carrier extraction is limited by mobility. Figure 7.5 summarises the carrier extraction results from all samples presenting dependences of the internal quantum efficiency (IQE) on applied voltage measured at the same excitation conditions. The IQE at 550 nm was evaluated as the number of generated charge carriers determined from the total voltage drop at long time divided by the number of absorbed light quanta. Carrier extraction from the (1:4) sample saturates at 2 V suggesting that the majority of excitons split into charge carriers, which are efficiently extracted. For the (1:1) and particularly the (2:1) samples, on the other hand, higher applied voltages are required for efficient carrier extraction.

The voltage drop at long times at 0 V applied voltage is expected to be proportional to the short circuit current in an operating solar cell. The short circuit current under steady state excitation (see table 7.1) in the (2:1), (1:1) and (1:4) devices (normalized to the signal recorded for the 2:1 device) increases as 1, 1.86, 2.15 whereas the relative voltage drop (from figure 7.4) increases somewhat more 1, 2.3, 4.1. The discrepancy is probably mainly caused by different sample excitation conditions. For pulsed excitation, not all electrons are extracted from the samples with low $PC_{61}BM$ concentration during the measurement time of several microseconds – some of them remain trapped on single $PC_{61}BM$ molecules or in weakly percolating domains. For CW excitation a stationary state with filled trapping sites is established and their influence is therefore reduced.

7.5. Carrier mobility: THz vs. TREFISH

The time dependent carrier mobility, averaged over electrons and holes, can be also obtained directly from the TREFISH and transient photocurrent measurements (equations 41 and 42). Figure 7.2 shows the experimental averaged mobilities. At short times the averaged mobilities correspond to the mean values between electron and hole mobilities, while at longer times, when fast carriers are already extracted, the average mobilities approach those of slower carriers. The averaged carrier mobilities in all samples decrease by about 4 orders of magnitude during approx. ten nanoseconds to reach long time values similar to those previously reported in the literature.[142,143] It should be noted, that the carrier mobility dynamics is expected to be free of influence of changing charge carrier concentration. This is because geminate recombination can be ruled out at strong electric field, while non-geminate recombination, as was discussed, is not substantial at our excitation intensities.

Carrier mobility and its time dependence can also be obtained from time resolved THz conductivity measurements.[142–145] For APFO3/$PC_{61}BM$ blends such measurements resulted in a mobility for the (1:4) blend remarkably similar to the averaged mobility obtained here with the TREFISH technique (figure 7.2) at early delay times of around 1 ps. However, from the measurements of blends with varying polymer chain lengths (APFO3 monomer to various molecular weight polymers) it was concluded that THz mobility of holes on the polymer chain is approximately five times higher (on the few ps time scale) than of electrons in $PC_{61}BM$.[143] This discrepancy in relative electron/hole mobility obtained by the two techniques can be understood as a difference in how they "sense" the carrier mobility. It was concluded that at a frequency of ≈ 1 THz this spectroscopy probes the motion of charges over a distance of ≈ 2-10 nm, corresponding to only a few polymer units.[146] Thus TREFISH and THz seem to probe somewhat different aspects of charge mobility – THz conductivity measures charge mobility over short nm-distances, whereas TREFISH measurements, based on the drift of charges, can be expected to measure mobility over longer distances. This implies that the TREFISH mobility is probably more closely related to the extraction kinetics, at least on longer time scale. In a way, THz photo-conductivity measurements reflect mainly an ability of charges to move, whereas TREFISH better reflects transport of charge carriers. Yet, on the shorter time and distance scale, both THz and TREFISH mobilities may be closely correlated. It is important to note that precisely this time scale is of critical importance for separation of charges initially generated at the place of photon absorption, to distances where their Coulomb attraction is overcome. In any case, both TREFISH and THz measurements for the (1:4) blend in figure 7.2 shows that the carrier mobility is high irrespective of the method of measurement. Figure 7.2 also shows that the carrier mobility is strongly time dependent, as expected, and shown before to be a result of relaxation in the density of states.[116,147] However, considering that the measured mobility has contributions from both electron and hole mobilities, and that these most likely have differing time dependencies, only modeling helps to determine the ratio of electron and hole mobility at an arbitrary time.

By correlating TREFISH mobility and extraction kinetics for the (1:4) blend one could conclude that the early-time mobility of ≈ 1 cm^2/Vs (figure 7.2) can be mainly correlated to electrons. At times > 1 ns in this blend most of the electrons are extracted (figure 7.1), implying that the measured TREFISH mobility (10^{-3} cm^2/Vs) beyond this point in time can be attributed to holes on the polymer. As concluded above, the hole mobility is relatively weakly dependent of the polymer:fullerene blending ratio. This is expected to be particularly true at short times, when intra-chain transport dominates. Hole mobility decreases by a factor of ≈ 100 over the first nanosecond. This is a somewhat stronger time dependence of hole mobility in APFO3 than suggested by time resolved THz measurements,[142,143] but is in line with the discussion above of differences in how THz and TREFISH measurements probe carrier mobility.

7.6. Donor-Acceptor ratio impact on solar cell performance

The saturation of IQE at 2 V in the (1:4) sample with 80% $PC_{61}BM$ (figure 7.5) shows that both generation and extraction of free charges saturate above this value, suggesting that both of these processes approach 100% efficiency. The fact that the carrier extraction efficiency in cells with lower $PC_{61}BM$ concentration is several times lower and shows no saturation indicates that at least one of these processes requires much stronger electric field to reach high efficiency. Since, non-geminate recombination in presented experiments is negligible, the voltage dependence of extracted charge is determined by the generation efficiency of free charges. Thus, for the non-optimal (2:1 and 1:1) blends an external electric field is required to separate electrons and holes and convert them into free mobile charges that can then be extracted.

For effective free carrier generation and extraction, high carrier mobility is essential [148,149] although in the literature there is no agreement which, electron [72,121,150] or hole [151,152] mobility is higher and plays a more important role. Results presented above provide a quantitative characterization of mobilities of both types of carriers and show that the electron mobility plays a crucial role in this type of polymer/fullerene blends. Since electron transport is governed by the properties of fullerene that should not experience any major alteration when blended with another polymer, such behaviour could be a general feature of all polymer/fullerene blends.

The extracted charge and the solar cell efficiency increase with $PC_{61}BM$ concentration when the electron mobility increases.[72,121,130,150–152] Balanced charge motion, when both electrons and holes have approximately equal mobility does not necessarily ensure the best cell performance – high mobility over large distances of one type of the charge carriers is more important for efficient solar cell operation. As has been demonstrated recently, the initial charge separation at weak electric field is mostly governed by diffusion,[116] which is directly proportional to carrier mobility. Thus, at high $PC_{61}BM$ concentrations, electrons diffuse sufficiently far from the hole to avoid fast geminate recombination, and even a weak electric field is sufficient to prevent geminate recombination at long times. Access to delocalized π electron states in ordered regions of the fullerene acceptor material within 40 fs after light absorption in an OPV model system could be another aspect of these observations.[66]

In case of low $PC_{61}BM$ concentration, fast electron motion is either restricted to small $PC_{61}BM$ domains or not possible at all if the CP state is formed on a single $PC_{61}BM$ molecule. If electron localization domain is smaller than the Coulomb

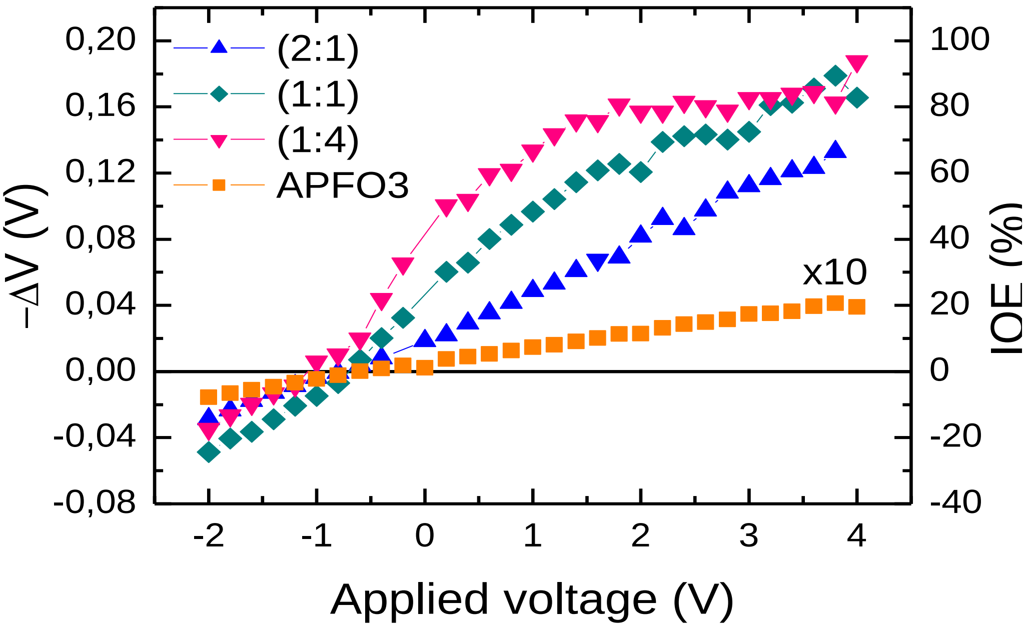

Figure 7.5 Total voltage drop corrected for the number of absorbed photons as a function of applied voltage. The right axis shows the calculated internal quantum efficiency (IQE).

radius (10-15 nm), then carrier separation depends on behaviour of the hole. Apparently the relatively restricted and slow hole motion in APFO3 is not sufficient to separate the charge carriers before their geminate recombination. IQE of the cells with low $PC_{61}BM$ concentration approaches that of the (1:4) device only if a strong external electric field is applied (figure 7.4). This can be understood as a result of a combined action of restricted hole diffusion and electric field induced drift over polymer segments separated by potential barriers.

Fast and balanced carrier extraction from the (1:1) device does not ensure its best solar energy conversion, which shows that it is not the carrier extraction which limits its performance efficiency. The generation efficiency of mobile charges at low electric field strongly increases with the $PC_{61}BM$ concentration and correlates with the carrier separation rate illustrated by TREFISH kinetics. Since fast carrier separation in blends with high $PC_{61}BM$ concentration mainly relies on the electron mobility, fast electron motion is essential for efficient charge carrier separation preventing their geminate recombination ensuring the best performance of the (1:4) solar cell despite of slow hole extraction.

8. Time dependent mobility in OPVs

It is common to make the implicit assumptions that mobilities of electrons and holes (a) correspond to the values in a near-equilibrium situation and (b) can be determined from many different kinds of experiments. Mobilities are thus considered a material constant (apart from a possible density or field dependence that are considered unimportant at the fields and densities encountered in OPV devices).[77,80,153] In fact, assumptions (a) and (b) convey a view on OPV cells as near-equilibrium devices that are at least in local thermal equilibrium. Empirically such a view seems at least partly justified by the success of drift-diffusion models in describing OPV current-voltage characteristics [77,154–156] and of Shockley-type models in describing the light intensity dependence of the open circuit voltage V_{OC}.[155,157–160] These assumptions, however, do not hold up to experimental scrutiny.

Analysis of the results presented in the previous chapter used power-law mobility models to describe charge transport. Good agreement of experimental data and modelled electric field kinetics following photo-excitation casts a strong shadow on the picture of constant mobility in organic solar cells. However, power-law mobility model does not implicitly explain the reasons why is mobility time-dependent. In this chapter, a much more powerful tool – Kinetic Monte Carlo modeling was employed to answer this question.

8.1. Time dependent vs constant mobility

Figure 8.1a shows the amount of charge extracted from TQ1:PC$_{71}$BM cell after pulsed laser excitation (550 nm) vs. time (solid lines). Initial dynamics, up to 3 ns after photo-excitation, were measured with TREFISH technique (explained in detail in section 4.5.2.) while charge extracted during ns-µs time window was captured with an oscilloscope. The indicated (reverse) bias is corrected for the built-in field of approximately -1 V.

In order to interpret the experimental data in figure 8.1a it is instructive to compare these to what would have been obtained in case charge transport were non-dispersive and governed by near-equilibrium mobilities. Colored areas in figure 8.1a correspond to electron and hole extraction if all charges move at near-equilibrium mobilities of $\mu_e = 4 \times 10^{-4}$ cm^2/Vs and $\mu_h = 6 \times 10^{-6}$ cm^2/Vs.[80]

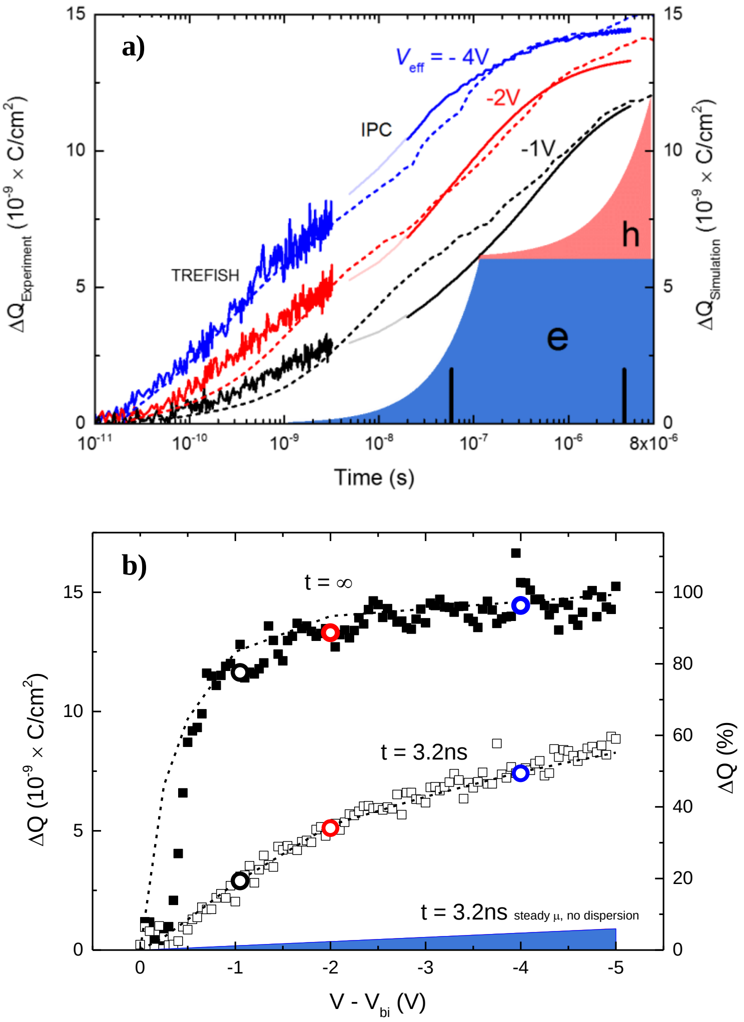

Figure 8.1 Charge extraction kinetics after pulsed excitation and its field dependence. (a) Combined TREFISH/TOF transients at different effective bias (solid lines) together with those obtained from Monte Carlo simulations (dashed lines). Due to limitations of electrical TOF measurements the initial ≈ 20 ns might be unreliable and are marked by thinner lines. Shaded areas illustrate extraction in case of non-dispersive transport and steady-state mobilities; in this case mean extraction times for electrons and holes are ≈ 0.06 µs and ≈ 4 µs, respectively (black vertical bars). The inset schematically shows the same on a linear time scale. (b) Bias dependence of the amount of extracted charge after 3.2 ns (open squares) and of the total extracted charge (filled squares). The amount of extracted charge obtained in the time-resolved experiment in panel (a) (open circles) is in good agreement with the field dependence measurement and Monte Carlo simulations (dashed lines). The shaded area again indicates the estimated behavior for steady-state mobilities.

Assuming a homogeneous generation profile, which is a reasonable approximation for the semitransparent devices used for the experiment, constant mobilities would translate into linear extraction profiles (exponential profile in logarithmic scale of fig. 8.1a). The linearity follows from the homogeneous electron and hole distributions being extracted at constant velocities. The first and the second step correspond to the electrons and holes being fully swept out of the device at an extraction time $t_{ex} = d^2/\mu_{e,h}V_{eff}$ with d the layer thickness and V_{eff} = -1 V the effective voltage. The mobilities mentioned above give rise to mean electron and hole extraction times of 0.06 µs and 4 µs, respectively. On basis of the large difference in t_{ex} it may be expected that the vast majority of electrons will have been extracted from the device before significant hole extraction takes place.

Two crucial features are evident when comparing the colored area to the actual experiment. First, charge collection starts orders of magnitude faster than the near-equilibrium mobilities allow, i.e. they do not give a relevant estimate of the actual extraction time. Second, apart from underestimating how rapid extraction is also the shape of the extraction curve is completely different from that of the non-dispersive (linear) prediction; the experimental trace is log-linear. Since the horizontal axis may also be read as an extraction time this indicates that there is a wide distribution of extraction times. This can be attributed to dispersion or a time-dependent mean mobility. It will be shown later, that both effects are important. In either case, the near-equilibrium mobility is a poor measure of the actual charge motion in operational solar cells; it not only underestimates the actual charge velocity by several orders of magnitude but also misses the wide spread in extraction times.

Deeper insight into the dispersive motion of photo-created charge carriers in organic solar cells can be gained from the simulation of experimental data in figure 8.1 by a kinetic Monte Carlo model. The model accounts for the hopping charge motion in the energetically disordered donor-HOMO and acceptor-LUMO levels in the bulk heterojunction and keeps track of all Coulomb interactions as well as exciton recombination and diffusion; see section 4.6.2 for more details. Monte Carlo simulations (dashed lines in fig. 8.1) reproduce well the two key features of the experiment: the dispersive shape of the charge extraction curve and the fact that charge extraction is much faster than would be expected on basis of near-equilibrium mobilities.

The field dependence of the amount of extracted charge is plotted in figure 8.1b. It is indicated for the characteristic time of 3.2 ns, where the TREFISH measurement ends (open squares), and when all charge is extracted (filled squares). At 3.2 ns significant hole extraction has not yet taken place, so only electron kinetics are probed. Clearly the simulation (dashed lines) captures the field dependence of the extraction kinetics very well. Apart from some deviations at low effective field also the total amount of extracted charge is well reproduced by the model, suggesting a reasonable description of recombination kinetics in this field regime. Recombination kinetics is, however, not the main purpose of the present work. The fact that equilibrium mobilities are a poor measure of the actual kinetics is once more highlighted by the colored area, which has been calculated while ignoring recombination and thereby forms an upper limit.

As discussed above, the large spread in extraction times of photo-created charges in OPV cells can be either due to dispersion or a time-dependent mean mobility or a combination thereof. In contrast to the experiments, the MC calculations can easily separate the two effects. Figure 8.2 (right y-axis) displays the transient mean total mobility, i.e. the sum of the mean electron and mean hole mobilities, extracted from Monte Carlo simulations with the same hopping parameters as used above. In line with the results in fig. 8.1 the mobility is far from constant; only beyond the µsec-range does it level off. The noise in the simulation at these times stems from the fact that by then the vast majority of charges have either been extracted or recombined, making it virtually impossible to reach converged results in this manner. Nevertheless, the predicted steady-state total mobility, which is entirely dominated by the larger electron mobility, agrees quite well with the near equilibrium value for $\mu_e = 4 \times 10^{-4}$ cm^2/Vs and, more importantly, with the values obtained from the photo-CELIV (charge extraction by linearly increasing voltage; see chapter 4.3) experiment (blue squares).

The simulation results in figure 8.2 are essentially independent of the initial concentration, i.e. light intensity. That means that on the time and energy scales relevant to charge extraction in OPV devices carrier kinetics and relaxation are not significantly affected by state filling effects; this is in stark contrast to the corresponding near-equilibrium situation where state filling is important at much lower concentrations.[161] It also allows to translate these results to OPV cells under steady state (CW, 1 Sun) operation.

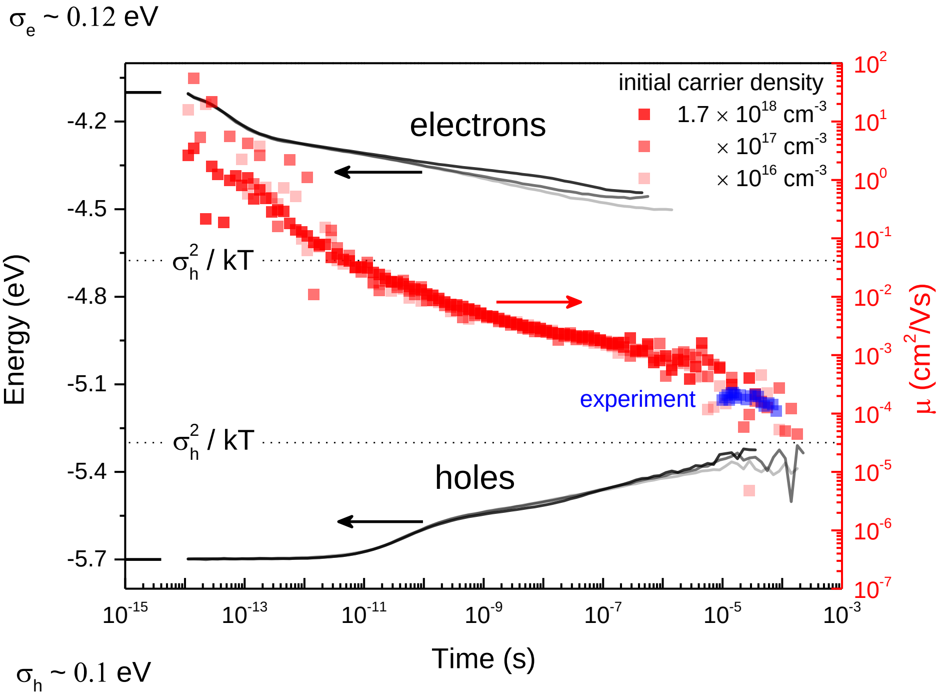

Figure 8.2 Simulated relaxation of photo-created charges and transient mobilities. Left y-axis shows electron and hole relaxation for the indicated initial concentrations. Relaxation starts at the HOMO -5.7 eV and LUMO -4.1 eV centers (black horizontal bars); Right y-axis shows the corresponding mean total mobility (red squares) and the transient mobility measured by photo-CELIV (blue squares). Simulations where carried out with periodic boundary conditions in all directions (i.e. no contacts) in the presence of a small electric field to enable determining the mobility without affecting it (1 V/100 nm).

8.2. Charge carrier relaxation

What is the physical reason for the fast charge carrier motion and its dispersion? It has been previously shown that dispersion of mobilities is of relevance to OPVs.[162,163] Also in a few recent papers the importance of fast, mainly diffusive motion of photo-generated charges was again highlighted.[116,123] This motion is driven both by entropic effects and by the ability of the charges to relax in the disordered density of states (DOS): white light excitation leads to electron and hole populations with mean energies at the center of the donor HOMO and donor LUMO (if significant exciton diffusion takes place this may cause some relaxation). However, as electron transfer to the acceptor is an energetically downward process this will, for statistical reasons, again lead to an electron population that is centered around the (acceptor) LUMO – assuming the electron is the charge that gets transferred; the hole population remains unchanged (and partially relaxed in case exciton diffusion is significant) upon charge transfer. Hence, the electron and the hole can substantially relax in their respective DOS after charge transfer. This motion (a) is energetically downward even though the remaining CT binding energy of ≈ 0.2 eV needs to be overcome [123,164] and (b) is therefore very fast. In contrast, near-equilibrium motion is governed by hops that are energetically upward (from the equilibrium energy to some transport energy) and is therefore much slower.[165]

The relaxation curves in figure 8.2 (left y-axis) quantify the picture sketched above. Although exciton diffusion is incorporated in the MC simulations, it does not lead to substantial relaxation before charge transfer takes place – it would give rise to simultaneous relaxation of the mean electron and hole energies, which is not observed. Hence both the electron and the hole relax by hopping motion, starting at the acceptor LUMO energy (-4.1 eV) and the donor HOMO energy (-5.7 eV), respectively. Due to their faster hopping, electron relaxation starts before hole relaxation. As relaxation continues, the number of ‘easy’ hops, i.e. energetically downward or only slightly up, decreases and therefore the mobility decreases. Note also that especially the electron population does not reach equilibrium (at an energy of $-\sigma^2/k_BT$ below the LUMO center) – the line stops where poor statistics due to the vanishing population set in. The last remaining holes do reach near-complete relaxation which is due to the lesser disorder in the donor HOMO than in the acceptor LUMO (σ_h = 0.1 eV vs. σ_e = 0.12 eV) which greatly affects the relaxation speed.[166] This does not mean that *all* holes have relaxed before leaving the device, as will be extensively discussed in the following text.

The energies and mobilities discussed so far are statistical means for the populations surviving at the indicated time. Hence, variations *within* these populations are not shown. In fact, such variations are an important cause for dispersion. As hopping charge motion is a statistical process, charges that happen to hop to a (very) low-lying state will take (very) long to be extracted. Conceptually it is tempting to consider such deep states as traps;[167] however, there is no fundamental difference between deeper and less deep states in the (Gaussian) DOS. In all cases charge motion, and concomitant relaxation is by hopping between localized states in a disordered energy landscape.

The dispersive motion of photo-created electrons and holes is characterized in figure 8.3. The top panel of figure 8.3a shows the transient mean electron and hole mobilities calculated for the TREFISH/IPC experiment in figure 8.1a at V_{eff} = -1 V. As expected, at long times both relax to the steady-state values indicated by the horizontal bars. These confirm that the measured photo-CELIV mobilities (filled and open symbols) reflect a near-equilibrium value for electrons and holes. The middle panel shows the distribution functions (per unit log-time) of the electron and hole extraction times (blue and red shaded areas, respectively), i.e. the time needed for each charge to be extracted after its photo-creation. As these histograms have an approximately log-normal shape, their means sit on the right-hand side of the mode (maximum) as indicated by the vertical bars. The normalized integrals of the distribution functions are presented in the bottom panel and reflect the fraction of charges that have been extracted after a certain time. Importantly, at the mean extraction time, about 80-90% of

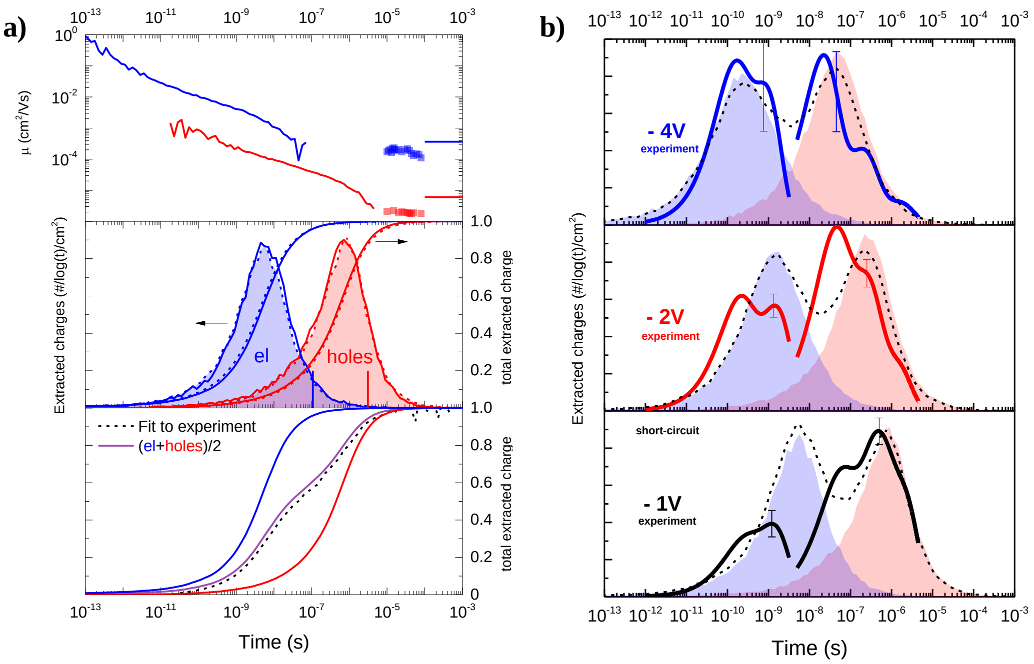

Figure 8.3 Dispersion in mobility and charge extraction time. (a) Top panel: simulated charge carrier mobility relaxation with time for electrons (blue) and holes (red) during a TREFISH experiment at V_{eff} = -1 V. Horizontal bars are corresponding steady-state mobilities, symbols are measured photo-CELIV mobilities of the TQ1:PC$_{71}$BM device (blue squares) and of a TQ1 film (red squares). Middle panel: extraction time distribution functions for the TREFISH simulations (dashed lines and shaded area, left y-axis); dashed lines match the steady-state device simulations at short circuit and ≈ 1 Sun. Solid and dashed lines (right y-axis) are the corresponding log-integrals. Vertical bars indicate mean extraction times. Bottom panel: comparison of an explicit TREFISH simulation (V_{eff} = -1 V, dashed black curve) with the average of the integrated electron and hole extraction time distributions under steady state (solid lines). (b) Experimental charge carrier extraction time distributions (thick solid lines) obtained as the log-time derivate of the experiment in fig. 8.1a. Dashed lines are the same procedure applied to the simulation curves. Shaded areas are the corresponding simulated extraction time distributions.

all photo-created charges have been extracted already. In fact, about 50% of all charges are more than an order of magnitude faster than the mean. This shows, once more, that mean extraction times are a very poor measure of the actual kinetics in OPV devices.

8.3. Relevance to typical operation of OPV cells

A crucial question is whether the TREFISH/IPC results, obtained after pulsed excitation, can be directly translated to operational solar cells that are CW excited with lower light intensity and concomitant lower charge densities. The affirmative answer to this question lies in the comparison of the above discussed results with simulations carried out with exactly the same parameters and (homogeneous) generation profile as in the TREFISH/IPC simulations but using continuous excitation with approximately 1 Sun intensity.

The solid lines in figure 8.3a (middle panel) show the extraction time distribution functions obtained from device simulations under steady state, which now reflect the time lag between carrier photo-generation and extraction. Good agreement between distribution functions is obtained from simulations under pulsed and CW (steady state) illumination conditions. This shows that pulsed excitation adequately reflects processes under CW excitation. Consequently, the averaged sum of the integrated electron and hole distributions as obtained from simulation under CW excitation perfectly reproduces carrier extraction kinetics obtained from simulations under pulsed excitation (solid and dashed lines in bottom panel of figure 8.3a). This is a key result as it allows to make statements about the dispersive charge kinetics during normal (CW, ≈ 1 Sun) solar cell operation on basis of pulsed (laser) measurements.

The bottom panel of figure 8.3a shows that, at least for sufficiently thin devices, the shape of the TREFISH/IPC response curve (dashed line) is equal to the sum of the integrated distribution functions during steady-state operation (solid line). The important consequence is that by calculating the log-time derivative of the TREFISH/TOF curve the distribution of extraction times in the solar cell under CW (1 Sun) operation can be obtained. This is shown in the b panel of figure 8.3 where the thick solid lines are now the experimental extraction time distribution functions obtained as $d(\Delta Q)/d(\log t)$ of the (smoothed) experimental data in figure 8.1a. Smoothing was accomplished by separately fitting TREFISH and IPC data by a sum of exponentials and is the cause of the small additional bumps in the experimental curves. Fitting converged at 2 and 3 exponentials for the TREFISH and IPC respectively. Error bars indicate the largest error if a different number of exponentials (3 and 2 respectively) would have been used instead. The dashed curves show the distributions obtained by applying the same method to the corresponding MC simulations. Given the noise in the experiments the agreement between distributions obtained from experimental and simulated data is rather satisfactory: a double peak structure is clearly visible, confirming the previously assumed time lag between electron and hole extraction. Moreover, the simulations do follow the experiments both in the magnitude of the dispersion, as can be measured by the shape and width of the separate peaks, and in the position and field dependence of the peak maxima.

8.4. Energy resolved current density

The strong dispersion in extraction times shown in fig. 8.3 suggests that in operational solar cells most of the photocurrent is carried by the fastest charges, i.e. the charges that do not get stuck in a deep site. On the other hand, charges that make up most of the density of occupied states (DOOS) are those that do get stuck and cause a build-up of space charge. The left panel of figure 8.4a shows that this intuitive distinction between more and less mobile charges can indeed be made. Plotted are the simulated steady-state electron and hole DOOS during ≈ 1 Sun operation at V_{eff} = -0.2 V (≈ MPP, solid lines) and at V_{eff} = -1 V (short-circuit, dashed lines). Due to the higher electron mobility the electron DOOS is lower than the hole DOOS; both decrease with field as expected. Note that the DOOS peaks do not lay at σ^2/k_BT below the LUMO or above the HOMO center, indicating incomplete thermalization of charge carrier distributions under steady-state conditions. This reflects the fact that charges typically leave the device, either by extraction or recombination, before they have thermalized in the DOS. In this context it is crucial to keep in mind the difference between thermalization by hopping around in an energetically disordered landscape, which is considered here, and on-site thermalization in, for instance, a vibrational manifold.[67]

More surprising is the energy-resolved current density in the right panel of fig. 8.4a; $j(E)$ is a distribution function of the current density over energy; integrating $j(E)$ gives the total current density that is positive and equal for both

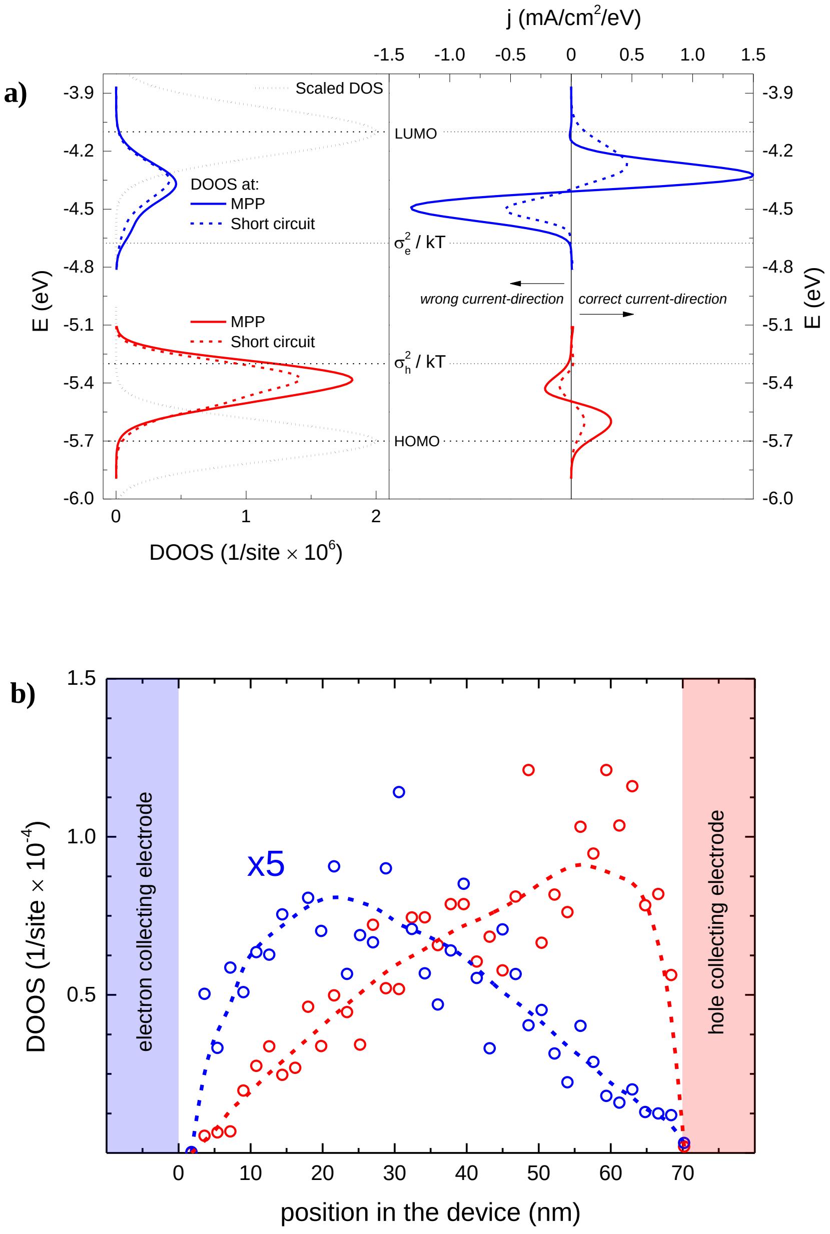

Figure 8.4 Energy distribution of charge and current density. (a) Left panel: DOOS distributions of electrons (blue) and holes (red) simulated during steady-state operation at the indicated V_{eff} and ≈ 1 Sun. HOMO and LUMO DOS are indicated as dotted lines (not to scale). Right panel: corresponding energy-resolved current density (top x-axis) showing the contributions to photocurrent from charge carriers at different energies. (b) Corresponding charge density profiles at short circuit (symbols). Long-dashed lines are a guide to the eye.

electrons and holes. Both the electrons and the holes show a positive contribution to the total current from lesser relaxed carriers and a smaller, negative contribution from more relaxed carriers. The positive and negative current peaks are due to, respectively, the drift and net diffusion contributions to the total current. The drift contribution simply follows the direction of the electric field and is therefore positive. The negative sign of the net diffusion contribution can be understood as follows: taking the holes as an example, the hole current density increases towards the hole extracting contact which follows from the fact that charges generated in an increasingly large fraction of the total film thickness contribute to the (local) current density. From this and the fact that charges that traveled longer distances will be further relaxed it follows that also the hole density increases towards the hole extracting contact as shown in fig. 8.4b. This leads to a charge density gradient (a) that is mostly directed away from the extracting contact and (b) that consists mainly of ‘relaxed’ holes. Hence the sign of the net diffusion current is negative and the peak in the hole DOOS coincides with the negative peak in $j(E)$. Similarly, the same can be explained for electrons. Hence, further relaxed charges do not only contribute less to the net current, they in fact counteract the net current due to the negative density gradient that gives rise to diffusion away from the contact. It should be kept in mind that drift and diffusion currents running in opposite directions are a well-understood characteristic of Ohmic contacts in general.[168] The distinct feature of the situation in fig. 8.4 is that these currents flow at different energies, once more highlighting that the system is far from equilibrium.

8.5. Polymer acceptors

The description of the behaviour of the photogenerated charges presented in the previous chapters is not limited to the devices investigated or even to polymer:PCBM solar cells. Insights drawn from the measurements and calculations presented here can be applied to a wide range of organic photovoltaic systems constituting of a disordered mixture of donor-acceptor materials, including PCBM-free devices or those based on small molecules.

Although devices employing fullerenes as the acceptor material currently demonstrate the best results in term of power conversion efficiency, there has long been a wish to replace PCBM with high electron mobility polymer. Fullerenes are not ideal acceptor materials. Major drawbacks include weak light absorption and fixed energy levels, limiting the number of possible electron donor pairs. So-called all-polymer or polymer-polymer devices consisting of polymer-donor and polymer-acceptor materials, not only overcome these issues, but possess many advantages over polymer-fullerene solar cells, including tunable chemical and electronic properties as well as enhanced stabilities.[110,169]

Figure 8.5 shows the time-resolved extraction of photo generated carriers at the indicated applied reverse bias in complete solar devices based on TQ1:N2200 compared to those of TQ1:$PC_{71}BM$. These traces represent the cumulative collected charge at the electrodes following excitation by a laser pulse.[94] Both types of devices show a similar charge extraction profile which is log-linear in shape and represents a wide spread of extraction times. As was previously shown in section 8.2 for the case of TQ1:$PC_{71}BM$ the first half of these transients is mainly dominated by the motion of electrons, whereas the second half

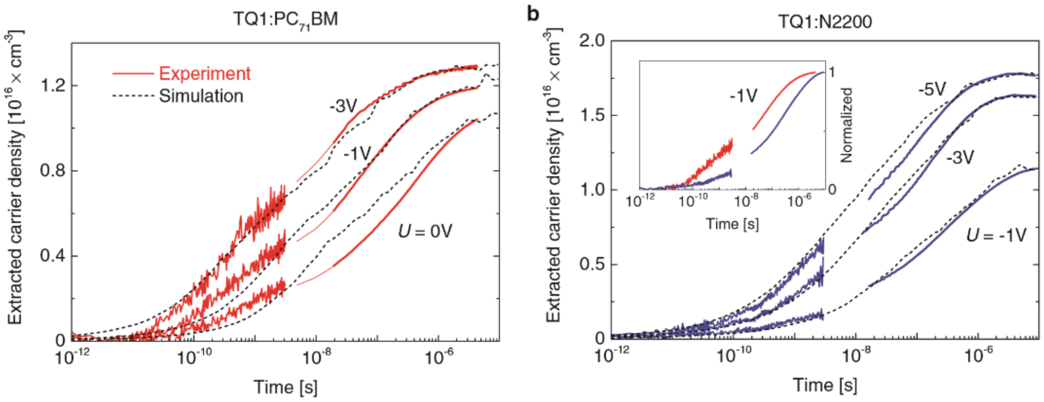

Figure 8.5 Time-resolved extraction of photogenerated charge carriers. (a) – TQ1:$PC_{71}BM$ solar cell excited at 550 nm with a pump fluence of 0.18 μJcm^{-2}. (b) – TQ1:N2200 solar cell excited at 810 nm with a pump fluence of 3.67 μJcm^{-2} (TQ1:N2200 absorbs weakly at this wavelength). Colored traces indicate experimental results, dashed black traces show results of kinetic Monte Carlo simulations. Inset in (b) shows that photogenerated carrier extraction in TQ1:$PC_{71}BM$ is significantly faster than in TQ1:N2200.

Table 8.1 Monte Carlo simulation parameters.

	Electrons		Holes	
	TQ1:PC$_{71}$BM	TQ1:N2200	TQ1:PC$_{71}$BM	TQ1:N2200
Energetic disorder, σ [meV]	125	141	113	127
Attempt-to-hop frequency, ν_0 [s^{-1}]	1.8×10^{13}	1.2×10^{13}	5×10^{10}	1×10^{11}

corresponds to the motion of holes. As in TQ1:N2200 blends only the acceptor has been replaced, the first half of the extraction kinetics is expected to be dominated by the motion of electrons in the N2200 phase. A side-by-side comparison of the extraction kinetics in both blends (Figure 8.5b, inset) suggests that the transport of photogenerated carriers in TQ1:PC$_{71}$BM is faster than in TQ1:N2200, yet the difference arises during the first half of the extraction phase, hinting at a lower electron mobility. Monte Carlo simulations were used to double-check this result. The experimental data in figure 8.5 was used to obtain the simulation parameters responsible for hopping carrier motion: a_{nn} is the inter-site distance, ν_0 is the attempt-to-hop frequency, and σ is the energetic disorder. In principle, the values of these parameters do not form a unique set - a large σ can be compensated by increasing ν_0. To avoid ambiguous fits to experiment, a_{nn} was fixed at a reasonable value of $a_{nn} = 1.8\,nm$.[123] This allowed for the fit of the experiment by a unique set of four parameters. The energetic disorder σ for holes/electrons defines dispersion, whereas hole/electron ν_0 defines the onset of charge motion. Reasonably good fits to the experiment could be obtained (figure 8.5, black dashed traces) using the parameter set in table 8.1.

Figure 8.6 shows the simulated photogenerated carrier mobility for both blends at an electric field strength of 1 V/100 nm. Time dependence of the photogenerated carrier mobility $\mu_{photo}(t)$ arises from the relaxation of the free charge carriers in the DOS. Rather similar hole mobility kinetics in both blends indicates that the transport of photogenerated holes in the donor phase is comparable when TQ1 is blended with either acceptor. Comparable hole transport is expected, as in both blends the TQ1 phase remains quite amorphous.[110,170] In contrast, the time-dependent electron mobility is significantly higher when TQ1 is blended with $PC_{71}BM$ instead of N2200, as suggested by experiments; see the inset of Figure 8.5b. As such, $PC_{71}BM$ is superior to N2200 as an electron transport material due to its higher time-dependent electron mobility. After a sufficiently long time delay following photoexcitation, the photogenerated carriers will reach quasi-equilibrium and have a constant (time-independent) mobility. In principle, in this regime the transport of photogenerated carriers is indistinguishable from that of injected carriers, as both are transported at similar energies in the DOS.

A practical implication of the above results is that mobilities found in one experiment are not necessarily relevant to the other, even if both are in the same density regime. The strong time dependence of the mobility of photo-created charges in combination with the fact that the vast majority of these charges gets extracted before full thermalization occurs makes mobilities from ”slow”

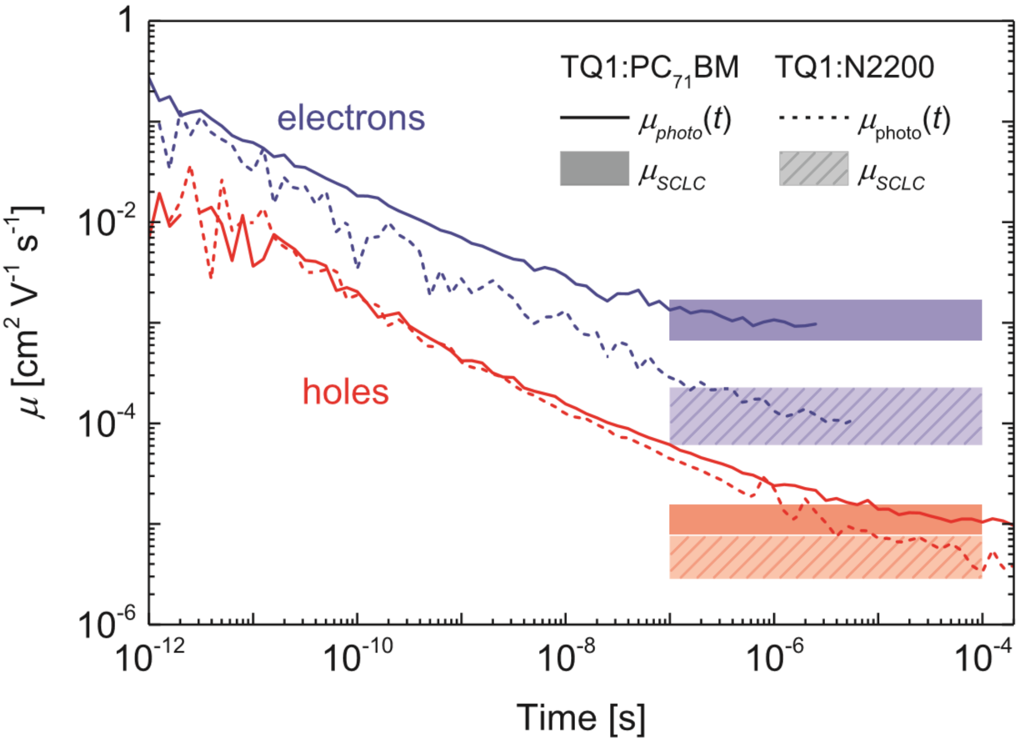

Figure 8.6 Simulated photogenerated carrier mobility for $TQ1:PC_{71}BM$ (solid lines) and TQ1:N2200 (dashed lines) comparison to SCLC mobility (solid fill and dashed fill respectively). Blue corresponds to electrons, red corresponds to holes.

experiments, that effectively probe the mobility of (almost) completely relaxed charges, like space charge limited currents (SCLC) and photo-CELIV are of limited relevance for understanding operational OPV cells. Mobilities extracted from dark current-voltage characteristics of OPV devices are therefore not particularly suited to make statements about the kinetics underlying the corresponding light current-voltage curve. Likewise, expressing recombination rates in operational OPV in terms of equilibrium mobilities seems of limited use. Even the relevance of properly defined and measured time-dependent mean mobilities is limited in view of the strong dispersion in extraction times.

9. Influence of active layer optimization

As the results presented in the previous chapters show, mobility of the photo-generated charges plays a crucial role in ensuring efficient charge extraction. Although employing bulk hetero-junction device architecture allowed for more efficient exciton dissociation, this approach, by its nature, hinder charge migration. High disorder in the active layer gives rise to a negative contribution to the total current from more relaxed charge carriers, while isolated donor or acceptor domains produces traps. It should then come as no surprise that optimisation of morphology of the active layer might, at least partially, help to address these issues.

Some rather simple methods of morphology optimization, such as blending ratio, solvent optimization and thermal annealing, have been successfully performed in the past.[53–57] Solvent additives, on the other hand, are a relatively new development.

One of the most efficient OPV blends is of the polymer PTB7 and the soluble fullerene $PC_{71}BM$ and it achieves high efficiency using a high-boiling-point solvent additive 1,8diiodooctane – (DIO) for processing the active layer.[26,128,171–174] The influence of DIO on morphology of PTB7:$PC_{71}BM$ blends has previously been investigated in detail, which indicated that the blends prepared without additive show pure fullerene clusters of 20-60 nm in size which form large agglomerates embedded in a polymer-rich matrix with about 30 wt.% fullerene in it.[175–178] The addition of DIO to the casting solvent improves the miscibility of $PC_{71}BM$ with PTB7, dramatically shrinks the size of the clusters to several nanometers and forms interpenetrating polymer-rich and fullerene rich phases of tens of nanometers in size.[175,177] Fluorescence quenching was found to be of similar efficiency in blends prepared with additive and without, suggesting that the increase of power conversion efficiency is not due to more efficient charge generation.[177] This is consistent with the power conversion efficiency enhancements occurring in both the polymer and fullerene absorption regions, suggesting that the improvement results from reduced carrier recombination instead.[175,177] The origin of reduced recombination is not known; possible explanations include improved charge separation, higher carrier mobility or reduced charge trapping.[177,179–181] It is therefore clear that a detailed understanding of the free carrier generation, transport and extraction in this important high performance blend is lacking.

9.1. Solar cell characterization

Figure 9.1 shows the current-voltage characteristics of the solar cells at the optimum blend ratio [P40:F60], prepared with and without DIO and measured at AM 1.5 conditions using a solar simulator from Sciencetech and the intensity calibrated with an ORIEL reference cell with KG5 filter. The spectral mismatch factor was close to unity (0.995) for PTB7:PC$_{71}$BM. An aperture of the same size as the pixel was used to avoid contribution from stray light outside the device area. The device prepared with DIO shows about two times higher short-circuit current J_{SC} and fill factor FF. Open circuit voltage V_{OC} does not depend on the solvent additive. The power conversion efficiency (PCE) of the device prepared with DIO was 5.4% at AM 1.5 conditions. It is important to note that the stack of the devices presented here has identical active layer properties

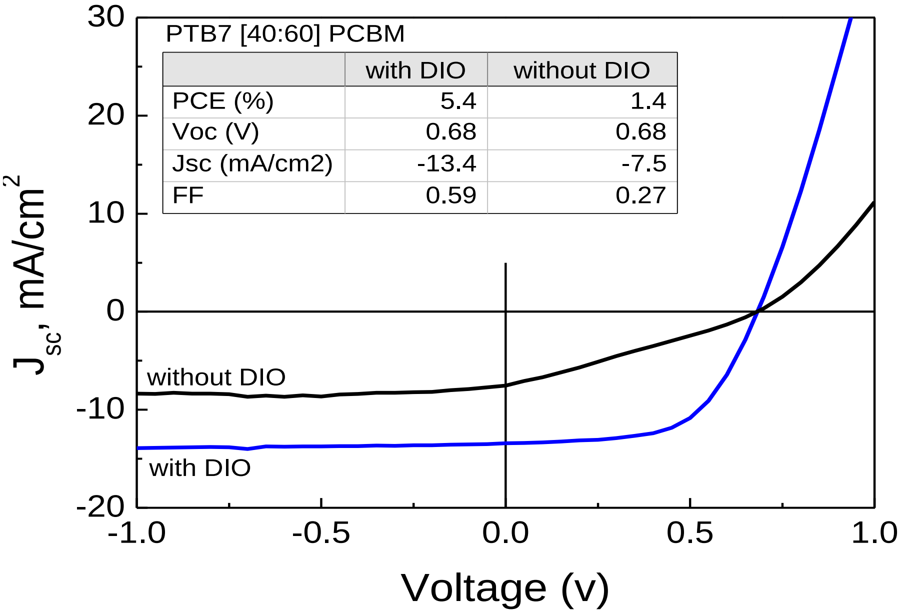

	with DIO	without DIO
PCE (%)	5.4	1.4
Voc (V)	0.68	0.68
Jsc (mA/cm2)	-13.4	-7.5
FF	0.59	0.27

Figure 9.1 Current-voltage characteristics of the PTB7:PC$_{71}$BM [40:60] solar cells under 1 Sun illumination.

(blend ratio, solution concentration, spin coating deposition parameters, thickness, deposition onto PEDOT) as the best reported devices, but suffers from lower overall performance owing to non-optimized contacts, resulting in efficiencies comparable to those which others report with similar non-optimized contacts.[171,175,177] None the less, the same dramatic improvement in overall device performance with the addition of DIO can still be seen and used as a basis for understanding on how the changes in morphology, that are known to be occurring, influence the electronic properties of the device.

9.2. Charge separation and extraction dynamics in optimized cells

Figure 9.2 shows the photo-induced voltage drop ΔU in the devices with 60 wt.% $PC_{71}BM$ which have the highest power conversion efficiency. It is measured by TREFISH in the time range from 0 to 3 ns. The long-time data are obtained from the integral-mode photocurrent (IPC) measurements.

The voltage drop at long times is proportional to the total amount of extracted charge from the device. At 1000 ns it is two times bigger in devices prepared with DIO which agrees well with about two times higher photocurrent observed in current-voltage characteristics at the short circuit condition and at reverse bias (fig. 9.1). In order to more clearly compare the extraction kinetics, figure 9.2 presents the voltage kinetics for the sample without DIO normalized to that for the sample with DIO as black dotted curves. They show that charge extraction at the 3 V bias is only marginally faster from the cell prepared with DIO. The difference is slightly stronger at 0 V bias. This indicates that the extraction efficiency of free carriers with a strong internal field is not particularly sensitive to morphology and suggests that the increased short circuit photocurrent in devices prepared with DIO is mainly due to more efficient charge separation rather than extraction. Combining this with previous observations that the charge generation efficiency is similar in blends prepared with additive and without,[177] leads to conclusion that the increase of photocurrent in devices prepared with DIO occurs mainly because of a higher dissociation efficiency of photogenerated charge pairs. The charge extraction at 0 V bias is faster in a device prepared with DIO as the time taken to extract a half of the charge decreases from 60 ns without DIO to 40 ns with DIO. In this case the internal electric field in the cell is lower than at the short circuit condition because the total voltage drop on the load resistor comes to nearly a half of the built-in voltage. A faster charge extraction from DIO-prepared devices at low built-in field reduces recombination losses and can explain the higher fill factor of solar cells prepared with DIO.

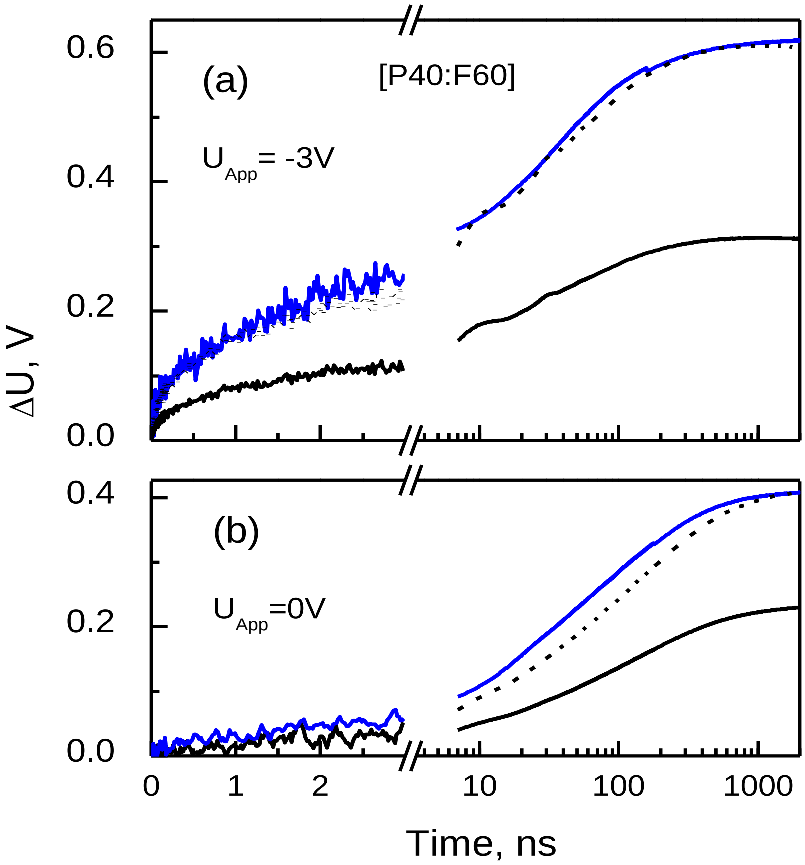

Figure 9.2 Photo-induced voltage drop in devices with 60 wt.% $PC_{71}BM$ at 3 V reverse bias **(a)** and at the built-in field only **(b)** as a function of time after the pump pulse. The results are derived from TREFISH measurements up to 3 ns and from the integral-mode photocurrent at longer times (note log scale after the axis break). Black curves correspond to devices without DIO, blue to devices with DIO. Black dotted curves show the kinetics from devices without DIO which are scaled to match the voltage drop in devices with DIO at late times. Pump density was $4 \cdot 10^{11}$ absorbed photons/cm^2 at the peak of polymer absorption (680 nm).

9.3. Charge generation in devices of different donor-acceptor ratio

The amount of charge extracted in 1 µs reveals the influence of electric field, blend ratio and the use of DIO on the charge separation efficiency (figure 9.3). The amount of extracted charge from the cell with 10 wt.% fullerene shows approximately linear dependence on the reverse bias with no saturation even at -4 V. At its maximum, ΔU from this cell is still about 20 times lower than from the cells with high fullerene content. This indicates that charge pairs are strongly bound and can only be separated by strong electric fields in the blend with low fullerene content. It is interesting to note that the additive DIO decreases the amount of extracted charge from the polymer-rich blend, which is opposite to what is observed in the fullerene-rich blends, and the reduction factor is independent of the applied bias. In contrast, the amount of charge extracted from other three blends is much higher and shows a weak dependence on the bias between -1 and -4 V indicating that a weaker electric field is sufficient to drive charge separation in fullerene-rich blends.

This result is consistent with previous observations of efficient free carrier generation in fullerene-rich blends [66] and much higher initial electron mobility in the fullerene than the hole mobility in the electron donors observed by means of THz spectroscopy.[182] The amount of charge extracted from the blends with 80 and 90 wt.% fullerene increases by about 30% with the increase of the negative bias between -1 and -4 V. This can be attributed to carrier generation from excitons deep inside $PC_{71}BM$ domains, a process which is assisted by an electric field. At high $PC_{71}BM$ concentrations the absorption by fullerene at the excitation wavelength (680 nm) is comparable to that of the polymer and many excitons are generated deep inside the fullerene phase. The three-dimensional exciton diffusion length in $PC_{71}BM$ can be estimated as $\sqrt{6D\tau}$ where D is exciton diffusion coefficient and τ is the exciton lifetime (described in more detail in chapter 2.2). Using the reported D and τ values,[177] exciton diffusion length of about 7 nm in the bulk $PC_{71}BM$ should be expected. With polymer concentrations at only 10-20 wt.% not all excitons created in fullerene domains reach the heterojunction – charge carriers can also be generated inside the fullerene domains with the assistance of an electric field as observed previously.[119,183] Such generation path can explain why the free carrier yield is bias-dependent. This suggests that carrier generation mechanism in the fullerene-rich blends could be different, depending if photon is absorbed by the polymer or by $PC_{71}BM$.

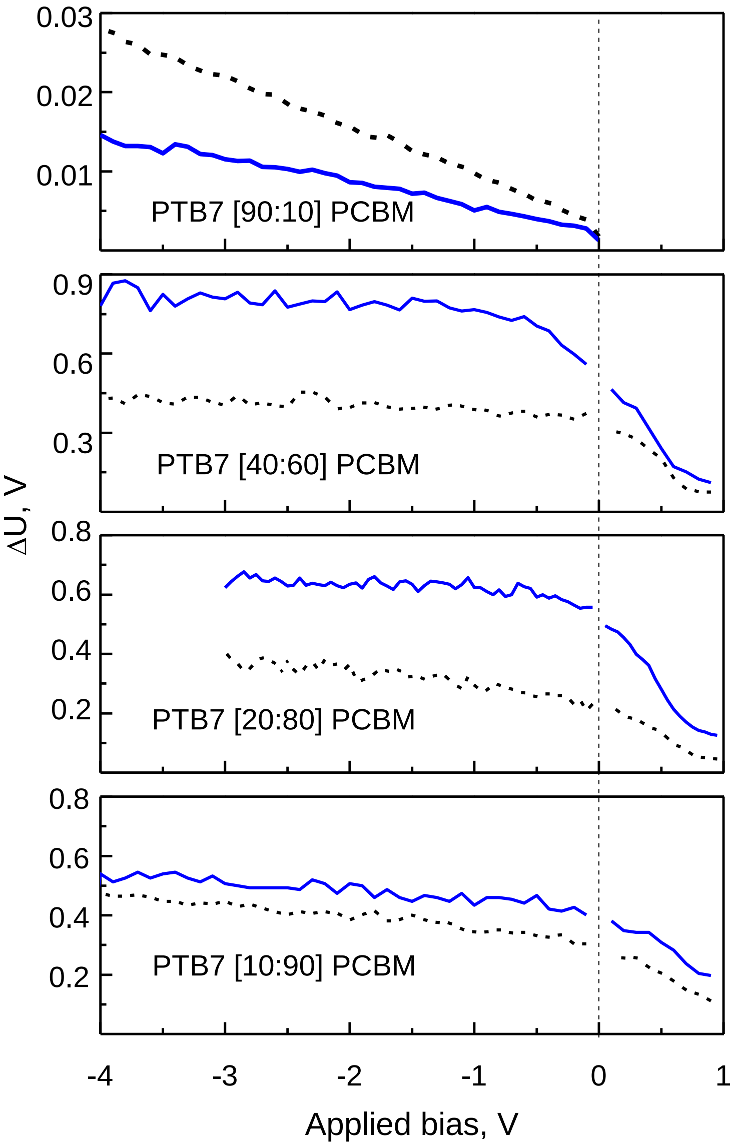

Figure 9.3 Photo-induced voltage drop at 1 μs from the integral-mode photocurrent measurements vs an applied external voltage in devices with different blend ratios for the excitation density of $4 \cdot 10^{11}$ absorbed photons/cm^2. Doted black and blue curves correspond to the devices without and with DIO respectively.

9.4. Effect of blend ratio and solvent additive on carrier mobility

In order to understand the role of electron and hole motion in charge separation and the effect of morphology, time-dependence of carrier extraction from devices prepared with different blend ratios (figure 9.4) was studied. The blends with high fullerene content show an enhancement of the amount of extracted charge when prepared with DIO, although the enhancement factor is slightly lower than that observed in a blend with 60 wt.% fullerene (figure 9.2). All fullerene-rich blends show a fast extraction phase within 10 ns which gets faster with increasing fullerene content and is followed by a slow phase on the 10-100 ns time scale. In the blend with 60 wt.% fullerene, half of the mobile carriers are extracted in ≈ 10 ns at a 3 V reverse bias (figure 9.2) whereas in the blend with 80 wt.% fullerene this happens in ≈ 2 ns (figure 9.4). Even faster carrier extraction is observed in the blend with 90 wt.% fullerene which is complete in ≈ 0.5 ns. This is similar to previous observations of very fast electron extraction from neat $PC_{61}BM$ films.[183] In contrast, carrier extraction from the polymer-rich blend is much slower and occurs on a 100-1000 ns time scale. This trend allows for the assignation of the fast extraction phase in fullerene-rich blends to electrons and the slow phase to holes. The additive DIO enhances the electron extraction rate from the fullerene-rich blends, yet slightly slows down carrier extraction from the polymer-rich blend.

In order to evaluate the electron and hole mobilities and their dependence on the blend ratio, power-law mobility model was employed (described in detail in section 4.6.1). Figure 9.5 presents the fits to the voltage kinetics as well as the electron and hole contributions to it. The insets show the simulated electron and hole mobilities. The simulations reproduce the experimental results well for the [P40:F60] and [P20:F80] samples, whilst the fits for the two extreme blend ratios are much worse. It is apparent that the power law functions cannot adequately describe the time dependences of the carrier mobilities at very low donor or acceptor concentrations. This is not surprising because these concentrations are at the percolation limit, and one type of carriers will inevitably encounter dead ends of charge transporting domains.[125] The simulated electron and hole contributions to integrated current show that only about 50% of electrons are extracted from the blend with 10 wt.% fullerene in 1 μs, and that extraction of holes from the blend with 90 wt.% fullerene is very inefficient. In solar cells with the optimal blend ratio of 60 wt.% fullerene electrons are extracted in

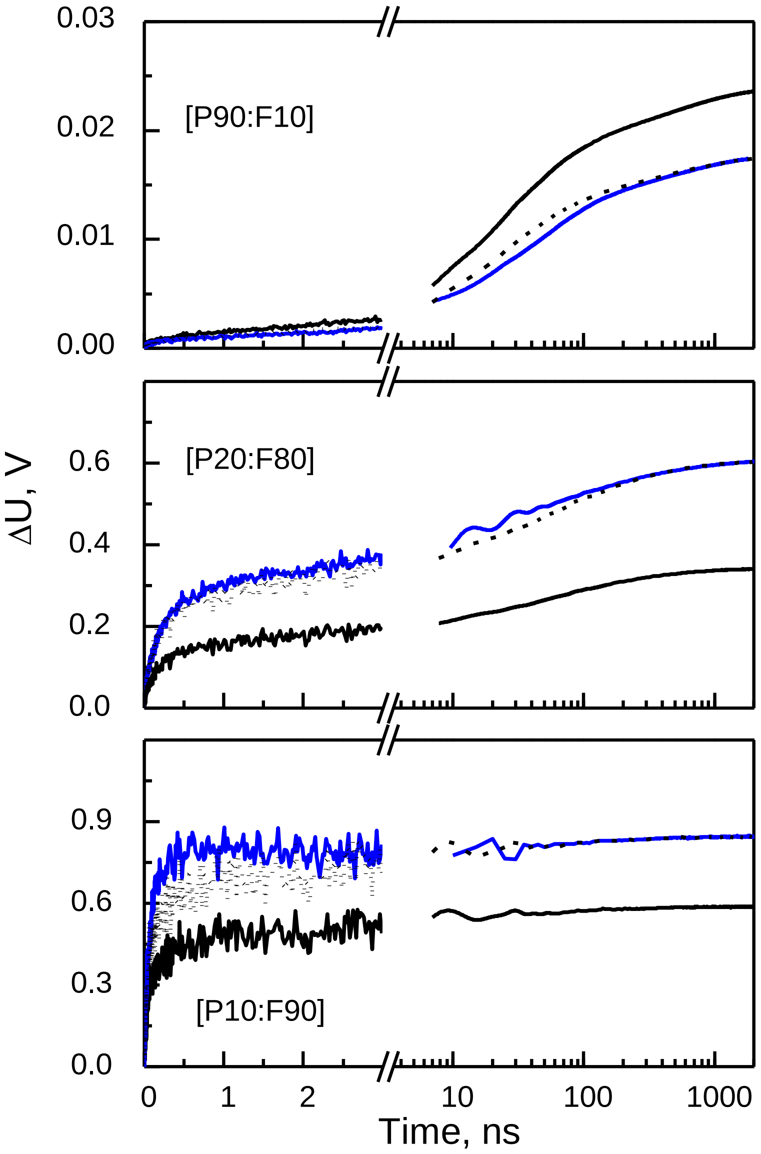

Figure 9.4 Photo-induced voltage drop for the pump density of $4 \cdot 10^{11}$ absorbed photons/cm^2 in PTB7:PC$_{71}$BM devices with very low and high fullerene content at 3 V reverse bias. Black curves correspond to devices without DIO, blue to devices with DIO. Black dotted curves show the kinetics from devices without DIO which are scaled to match the voltage drop in devices with DIO at long times.

≈ 40 ns at a -3 V bias, whereas the hole extraction takes ≈ 200 ns. This indicates that carrier extraction is slightly unbalanced in optimized devices. In the blends with the fullerene content of 60, 80 and 90 wt.%, the electron mobility in the first 10 ps after the pump pulse is > 0.1 $cm^2V^{-1}s^{-1}$ (see inset of figure 9.5). The electron mobility in the device optimized with DIO is only slightly higher. High

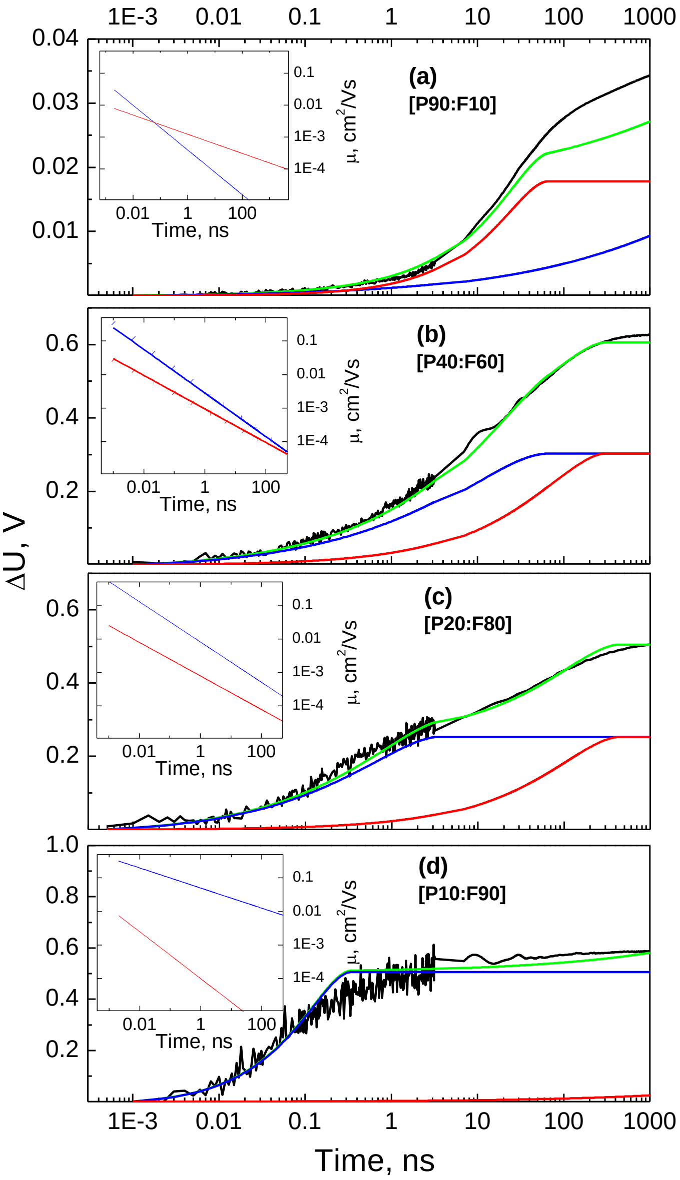

Figure 9.5 Modelling results of the carrier extraction kinetics from the cells prepared with different blend ratios without DIO at 3 V reverse bias. Black lines are the experimental data, green lines are the modelled kinetics, blue and red lines show electron and hole contributions respectively. Insets show time-dependent electron (blue lines) and hole (red lines) mobility obtained from the fits. Symbols in the inset to plot (b) show electron and hole mobility in the [P40:F60] cell prepared with DIO.

electron mobility drives fast dissociation of generated charge pairs into free carriers. The blend with 90 wt.% fullerene shows a weak $\mu_e \propto t^{-0.3}$ time dependence which can be explained by electron trapping at low energy sites. For comparison, the electron mobility in blends with 60 and 80 wt.% fullerene shows a stronger time dependence $\mu_e \propto t^{-0.6}$ suggesting that there might be another mechanism allowing for the drop in mobility in addition to relaxation to low energy sites (chapter 8). It is natural to assume that the electron mobility decreases when electrons reach the boundaries of fullerene clusters and fullerene-rich domains. This assumption is supported by an about ten times lower initial electron mobility in the blend with 10 wt.% fullerene and its rapid decrease with time as $\mu_e \propto t^{-0.7}$, both showing that the electron transport is at a percolation limit in this blend. The highest initial hole mobility is observed in the optimized blend with 40 wt.% polymer and not in the blend with 90 wt.% polymer indicating that the slow dissociation of bound electron-hole pairs limits the hole mobility in the polymer-rich blend. The time-dependence of hole mobility is very similar to that of electrons and follows $\mu_h \propto t^{-0.3}$ in the polymer-rich blend which changes to $\mu_h \propto t^{-0.7}$ in the blend with 10 wt.% of the polymer. The hole mobility at times > 1 ns agrees well with the steady state values of hole mobility reported in blends of PTB7 with the fullerene $PC_{61}BM$ which showed a decrease by three orders of magnitude when the fullerene concentration increased to 90 wt.%.[184] Results presented above suggest that the mobility of both types of carriers is controlled by low energy and spatial traps in the blends. The initial values of hole mobility, however, are not strongly dependent on the blend ratio. This can be explained by the faster hole transport along the conjugated polymer chains as compared to transport between chains.[185]

9.5. Effects of DIO on device morphology

In the most efficient blend of [P40:F60] with DIO, an optimum morphology of a finely interpenetrating network of PTB7 and $PC_{71}BM$ is formed and the total amount of extracted charge is double that of a blend prepared without DIO. Experimental results presented above indicate that this enhancement is based on a higher dissociation efficiency of generated charge pairs into free carriers which is independent of the applied electric field. An internal quantum efficiency of > 0.9 has been demonstrated in PTB7:PC$_{71}$BM solar cells prepared with DIO [26,171,172,177] implying that the free carrier generation efficiency is close to unity in optimized blends. Since the charge generation efficiency was found to be similar in blends prepared with additive and without,[177] this indicates that about a half of generated charge pairs in the blends prepared without DIO never dissociate into free charge carriers. Previous studies of morphology and photo-physics of PTB7:PC$_{71}$BM blends prepared without the additive showed large pure fullerene clusters of 20-60 nm in size which were embedded in a polymer-rich phase with about 30 wt.% fullerene mixed in it.[175–178] Based on the observations of the pair dissociation efficiency being low in polymer-rich blends, one can assume that the geminate charge pairs generated between polymer and dispersed fullerene molecules in the polymer-rich phase never dissociate, as illustrated in figure 9.6. This happens because the hole mobility in PTB7 is inherently low and fullerene molecules in the polymer-rich phase are too far from each other. PTB7:PC$_{71}$BM blends prepared using the additive DIO have been shown to consist of interpenetrating polymer-rich and fullerene-rich domains of tens of nanometers in size and large pure domains were no longer observed.[175–177] These polymer- and fullerene-rich domains imply that there is a concentration gradient of donor and acceptor molecules between these domains. In such a morphology charge separation can be thermodynamically driven as the entropy increases with carrier motion from the lower to higher concentration of acceptor molecules. For efficient charge separation all fullerene molecules have to be well connected to provide unperturbed electron motion. An insight into the development of a well-connected fullerene network in blends of PTB7 with a fullerene PC$_{61}$BM processed with DIO has been given by in situ measurements of the grazing incidence small-angle X-ray scattering during solvent evaporation.[175] These studies showed rapid formation of crystalline PTB7 aggregates driven by rapid evaporation of chlorobenzene but spontaneous phase separation was not observed presumably because of very slow evaporation of DIO which is a good

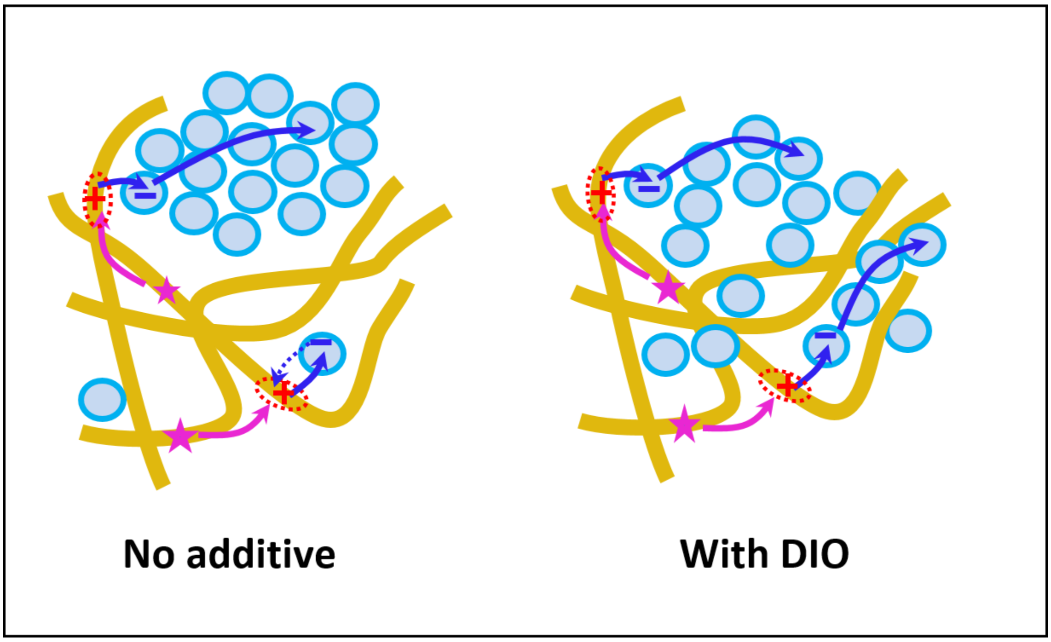

Figure 9.6 Schematic of the proposed charge separation mechanism in PTB7:PC$_{71}$BM solar cells. According to previous morphology studies, the blends prepared without additive form pure fullerene clusters of 20-60 nm in size which are embedded in a polymer-rich phase with about 30 wt.% fullerene mixed in it.[175–178] The charge pairs generated at the dispersed fullerene molecules do not dissociate because of low hole mobility and only charge pairs generated at the fullerene clusters give photovoltaic response. The addition of DIO to the casting solvent improves the miscibility of PC$_{71}$BM with PTB7 and forms interpenetrating polymer-rich and fullerene-rich phases of tens of nm in size.[175,177] Charge separation in these blends is driven by fast electron motion in the fullerene-rich phase. Small scale phase separation also improves charge transport at low built-in field.

solvent for fullerene molecules. Shrinkage of the fullerene domains in PTB7:fullerene blends with addition of DIO is different from DIO's role in altering the morphology in other photovoltaic blends where it promotes phase separation of two intimately mixed materials.[186]

The increase of free carrier yield with DIO is also observed in blends with 80 and 90 wt.% fullerene but the effect is less pronounced presumably because the fullerene molecules are better connected at higher concentration even without the additive. DIO also increases the carrier extraction velocity at weak electric field which can be explained by improved connectivity of nanostructured polymer-rich and fullerene-rich domains providing faster percolation channels for extraction of both types of carriers. The DIO enhances the performance of all fullerene-rich blends but it reduces the amount of extracted charge from the polymer-rich blend. Even though the charge separation in the polymer-rich blend shows strong electric field dependence, the reduction factor of extracted charge with DIO is field-independent, suggesting that DIO changes the morphology of this non-optimum polymer-rich blend too.

10. Conclusions and outlook

As we have seen, charge carrier mobility is one the key parameters determining power conversion efficiency of organic solar cells. Thus, understanding the full picture of charge migration in the active layer is of the upmost importance. Work presented above investigated multiple segments of this picture from the initial electron transfer at the donor-acceptor interface to the identification of the most relaxed charge carriers as the negative contributors to the overall photocurrent of the device.

10.1. Conclusions

Following electron transfer at organic interfaces electron delocalization occurs on a femtosecond time scale, during which the electron wavefunction spreads in the acceptor phase. Although the extent of the electron wavefunction in PCBM is limited to only several molecules, it is already sufficient to facilitate an average electron-hole separation distance of ≈ 2.5 nm on a femtosecond time scale. Coherent propagation also shapes the “initial” e-h distance distribution, which can be implemented in classical hopping models that are valid at time scales > 500 fs – the transition time from coherent propagation to incoherent hopping. Stochastic Schrödinger equation modelling, used to obtain these results, is not specific to OSCs and may be generalized to explain charge transfer not only at any molecular interface but also in other collectively coupled molecular system.

IQE and PCE for polymer-fullerene cells are strongly dependent on fullerene concentration; fullerene concentrations of ≥ 50% (w/w) is required for the best performance of the solar cell. This conclusion can be traced to the very strong dependence of electron mobility in the fullerene phase on the polymer-fullerene ratio, giving rise to a variation of extraction times by a factor of more than 1000 when the fullerene content is varied from 33% to 80%. Simultaneously, hole mobility alters much less (approximately ten times), making the precise nature of the polymer phase and its hole mobility less critical for the solar cell performance. Therefore, fast electron motion between fullerene molecules is essential, enabling efficient separation of geminate charge pairs in low electric field of the devices. Carrier separation via hole motion when electrons are immobile is much slower and requires strong electric field not present in operating solar cells. It is worth noting that similar electron and hole mobility dependences on the blending ratio has been observed in other efficient blends of fullerenes with polymers and small molecules. This also explains why different polymer and small molecule donors show similar performance in solar cells based on bulk heterojunctions with fullerene derivatives.

Charge extraction was experimentally shown to be highly dispersive, with which it is meant that (a) the mobility depends very strongly on time after photo-creation and that (b) there is a large spread in charge extraction times, covering multiple orders of magnitude. Using the experimental data to define parameters for kinetic Monte Carlo modelling, the dispersion was shown to be due to relaxation of photo-generated charges in the disordered density of states; on the length scale of the device thickness charge motion is completely dominated by this relaxation. In fact, due to the (deliberate) simplicity of the Monte Carlo model, which excludes potential additional sources of dispersion in blends due to e.g. non-perfect percolation of PCBM (and polymer) domains creating spatial rather than energetical traps, the calculated dispersions should, for the used parameters, be considered as a lower limit.

It was also shown that the extraction time distribution of photo-generated charges, which is a relevant measure of the dispersion of an OPV device under operational conditions, can be determined from measured pulse responses. Moreover, charge kinetics are orders of magnitude faster than what would be expected on basis of near-equilibrium mobilities. The strong time dependence of the mobility of photo-created charges in combination with the fact that the vast majority of these charges gets extracted before full thermalization occurs makes mobilities from ”slow” experiments, that effectively probe the mobility of (almost) completely relaxed charges, like space charge limited currents

(SCLC) and photo-CELIV are of limited relevance for understanding operational OPV cells. Even the relevance of properly defined and measured time-dependent mean mobilities is limited in view of the strong dispersion in extraction times. These results hold true not only for particular polymer-PCBM solar cells but are rather a common feature of disordered BHJ systems.

Short circuit current in PTB7:PC$_{71}$BM organic solar cells is determined by the separation of charge pairs into free carriers. This separation is found to be efficient in fullerene-rich blends and inefficient in the polymer-rich blends suggesting that high mobility of one type of carriers is essential for efficient charge separation. The free carrier yield is higher by a factor of two in devices prepared with DIO than without at the optimal blend ratio. Half of the generated charge pairs in the blends prepared without DIO never dissociate into free charge carriers, which can be attributed to charge pairs generated in the polymer-rich domains with molecularly dispersed fullerene molecules. DIO only weakly influences the carrier mobility. The carrier extraction rate slightly increases with morphology optimization with DIO, but only at low built-in electric fields. These findings explain the higher photocurrent and fill factor of devices prepared with DIO. These results also show that carrier extraction is unbalanced in optimized devices with electron extraction being about ten times faster than the hole extraction.

10.2.Outlook

Even though polymer-fullerene solar cells have recently achieved the famed and long-established goal of 10% power conversion efficiency, immense work in this area still awaits. Manufacturing price of conventional silicone solar cells steadily decreases, calling for even higher efficiency of organic solar cells in order to compete on the same W/€ level. What is more, shifting from spin-coating manufacturing in the lab to the industrial roll-to-roll processing inflicts its toll on the performance of such devices. A combination of non-toxic solvents and additives with the manageable processing and post-processing techniques which does not corrupt the morphology of the active layer is yet to be found.

Stability and longevity of the polymer-based compounds have been left on the back burner as well. All of these issues should be addressed in due time if organic solar cells are to compete with the established technologies. Inventing new materials, applying new processing methods, developing new models for analyzing and understanding the photophysics are in high demand to further advance the field.

Recent discovery and subsequent soar in perovskite solar cell efficiency has captured much of the photovoltaic academic world by surprise. However, it should not be viewed as a prophet of demise of polymer-PCBM solar cells but rather as a demonstration that disordered heterojunction approach is indeed viable and could be advanced further than previously imagined. Close collaboration between the two fields is essential for the progress of both technologies.

11. References

(1) Hermann, W. A. Quantifying Global Exergy Resources. *Energy* **2006**, *31* (12), 1349–1366 DOI: 10.1016/j.energy.2005.09.006.

(2) Tsoutsos, T.; Frantzeskaki, N.; Gekas, V. Environmental Impacts from the Solar Energy Technologies. *Energy Policy* **2005**, *33* (3), 289–296 DOI: 10.1016/S0301-4215(03)00241-6.

(3) Adams, W. G.; Day, R. E. The Action of Light on Selenium. *Proc. R. Soc. London* **1877**, *A25*, 113.

(4) Chapin, D. M.; Fuller, C. S.; Pearson, G. L. A New Silicon P-N Junction Photocell for Converting Solar Radiation into Electrical Power [3]. *J. Appl. Phys.* **1954**, *25* (5), 676–677 DOI: 10.1063/1.1721711.

(5) Murray Hill, N. J. Vast Power of the Sun Is Tapped by Battery Using Sand Ingredient. *New York Times* **1954**, 1.

(6) Razykov, T. M.; Ferekides, C. S.; Morel, D.; Stefanakos, E.; Ullal, H. S.; Upadhyaya, H. M. Solar Photovoltaic Electricity: Current Status and Future Prospects. *Sol. Energy* **2011**, *85* (8), 1580–1608 DOI: 10.1016/j.solener.2010.12.002.

(7) Green, M. A.; Zhao, J.; Wang, A.; Wenham, S. R. Progress and Outlook for High-Efficiency Crystalline Silicon Solar Cells. *Sol. Energy Mater. Sol. Cells* **2001**, *65* (1), 9–16 DOI: 10.1016/S0927-0248(00)00072-6.

(8) Kosten, E. D. E.; Atwater, J. H. J.; Parsons, J.; Polman, A.; Atwater, H. A. Highly Efficient GaAs Solar Cells by Limiting Light Emission Angle. *Light Sci. Appl.* **2013**, *2* (1), 1–6 DOI: 10.1038/lsa.2013.1.

(9) Krogstrup, P.; Jørgensen, H. I.; Heiss, M.; Demichel, O.; Holm, J. V; Aagesen, M.; Nygard, J.; Fontcuberta i Morral, A. Single-Nanowire Solar Cells beyond the Shockley–Queisser Limit. *Nat. Photonics* **2013**, *7* (March), 1–5 DOI: 10.1038/nphoton.2013.32.

(10) Dimroth, F.; Grave, M.; Beutel, P.; Fiedeler, U.; Karcher, C.; Tibbits, T. N. D.; Oliva, E.; Siefer, G.; Schachtner, M.; Wekkeli, A.; Bett, A. W.; Krause, R.; Piccin, M.; Blanc, N.; Drazek, C.; Guiot, E.; Ghyselen, B.; Salvetat, T.; Tauzin, A.; Signamarcheix, T.; Dobrich, A.; Hannappel, T.; Schwarzburg, K. Wafer Bonded Four-Junction GaInP/GaAs//GaInAsP/GaInAs Concentrator Solar Cells with 44.7% Efficiency. *Prog. Photovoltaics Res. Appl.* **2014**, *22* (3), 277–282 DOI: 10.1002/pip.2475.

(11) Tobin, S. P.; Vernon, S. M.; Wojtczuk, S. J.; Bajgar, C.; Sanfacon, M. M.; Dixon, T. M. Advances in High-Efficiency GaAs Solar Cells. In *IEEE Conference on Photovoltaic Specialists*; IEEE, 1990; pp 158–162.

(12) Kayes, B. M.; Nie, H.; Twist, R.; Spruytte, S. G.; Reinhardt, F.; Kizilyalli, I. C.; Higashi, G. S. 27.6% Conversion Efficiency, a New Record for Single-Junction Solar Cells under 1 Sun Illumination. *Conf. Rec. IEEE Photovolt. Spec. Conf.* **2011**, 000004–000008 DOI: 10.1109/PVSC.2011.6185831.

(13) Barnes, T. M.; Rance, W. L.; Burst, J. M.; Reese, M. O.; Meysing, D. M.; Wolden, C. A.; Mahabaduge, H.; Li, J.; Beach, J. D.; Gessert, T. A.; Garner, S. M.; Cimo, P.; Metzger, W. K. High-Efficiency Flexible CdTe Superstrate Devices. *2014 IEEE 40th Photovolt. Spec. Conf. PVSC 2014* **2014**, 2289–2292 DOI: 10.1109/PVSC.2014.6925383.

(14) Jackson, P.; Hariskos, D.; Wuerz, R.; Wischmann, W.; Powalla, M. Compositional Investigation of Potassium Doped Cu(In,Ga)Se2 Solar Cells with Efficiencies up to 20.8%. *Phys. Status Solidi - Rapid Res. Lett.* **2014**, *8* (3), 219–222 DOI: 10.1002/pssr.201409040.

(15) Jackson, P.; Hariskos, D.; Lotter, E.; Paetel, S.; Wuerz, R.; Menner, R.; Wischmann, W.; Powalla, M. New World Record Efficiency for Cu(In,Ga)Se2 Thin-Film Solar Cells beyond 20%. *Prog. Photovoltaics Res. Appl.* **2011**, *19* (7), 894–897 DOI: 10.1002/pip.1078.

(16) Bagnall, D. M.; Boreland, M. Photovoltaic Technologies. *Energy Policy* **2008**, *36* (12), 4390–4396 DOI: 10.1016/j.enpol.2008.09.070.

(17) O'Regan, B.; Grätzel, M. A Low-Cost, High-Efficiency Solar Cell Based on Dye-Sensitized Colloidal TiO2 Films. *Nature* **1991**, *353* (6346), 737–740 DOI: 10.1038/353737a0.

(18) Nazeeruddin, M. K.; Baranoff, E.; Grätzel, M. Dye-Sensitized Solar Cells: A Brief Overview. *Sol. Energy* **2011**, *85* (6), 1172–1178 DOI: 10.1016/j.solener.2011.01.018.

(19) Mathew, S.; Yella, A.; Gao, P.; Humphry-Baker, R.; Curchod, B. F. E.; Ashari-Astani, N.; Tavernelli, I.; Rothlisberger, U.; Nazeeruddin, M. K.; Grätzel, M. Dye-Sensitized Solar Cells with 13% Efficiency Achieved through the Molecular Engineering of Porphyrin Sensitizers. *Nat. Chem.* **2014**, *6* (3), 242–247 DOI: 10.1038/nchem.1861.

(20) Krebs, F. C. Polymer Solar Cell Modules Prepared Using Roll-to-Roll Methods: Knife-over-Edge Coating, Slot-Die Coating and Screen Printing. *Sol. Energy Mater. Sol. Cells* **2009**, *93* (4), 465–475 DOI: 10.1016/j.solmat.2008.12.012.

(21) Zhao, W.; Qian, D.; Zhang, S.; Li, S.; Inganäs, O.; Gao, F.; Hou, J. Fullerene-Free Polymer Solar Cells with over 11% Efficiency and Excellent Thermal Stability. *Adv. Mater.* **2016**, 4734–4739 DOI: 10.1002/adma.201600281.

(22) Liu, Y.; Chen, C.-C.; Hong, Z.; Gao, J.; Yang, Y. M.; Zhou, H.; Dou, L.; Li, G.; Yang, Y. Solution-Processed Small-Molecule Solar Cells: Breaking the 10% Power Conversion Efficiency. *Sci. Rep.* **2013**, *3*, 3356 DOI: 10.1038/srep03356.

(23) Chen, J.; Cui, C.; Li, Y.; Zhou, L.; Ou, Q.; Li, C.; Li, Y.; Tang, J.-X. Single-Junction Polymer Solar Cells Exceeding 10 % Power Conversion Effi Ciency. *Adv. Mater.* **2014**, *27* (6), 1035–1041 DOI: 10.1002/adma.201404535.

(24) Liu, Y.; Zhao, J.; Li, Z.; Mu, C.; Ma, W.; Hu, H.; Jiang, K.; Lin, H.; Ade, H.; Yan, H. Aggregation and Morphology Control Enables Multiple Cases of High-Efficiency Polymer Solar Cells. *Nat. Commun.* **2014**, *5* (9), 5293 DOI: 10.1038/ncomms6293.

(25) He, Z.; Xiao, B.; Liu, F.; Wu, H.; Yang, Y.; Xiao, S.; Wang, C.; Russell, T. P.; Cao, Y. Single-Junction Polymer Solar Cells with High Efficiency and Photovoltage. *Nat. Photonics* **2015**, *9* (February), 174–179 DOI: 10.1038/nphoton.2015.6.

(26) Ouyang, X.; Peng, R.; Ai, L.; Zhang, X.; Ge, Z. Efficient Polymer Solar Cells Employing a Non-Conjugated Small-Molecule Electrolyte. *Nat. Photonics* **2015**, *9* (July), 520–524 DOI: 10.1038/nphoton.2015.126.

(27) Dvorak, M.; Wei, S. H.; Wu, Z. Origin of the Variation of Exciton Binding Energy in Semiconductors. *Phys. Rev. Lett.* **2013**, *110* (1), 1–5 DOI: 10.1103/PhysRevLett.110.016402.

(28) Knupfer, M. Exciton Binding Energies in Organic Semiconductors. *Appl. Phys. A Mater. Sci. Process.* **2003**, *77* (5), 623–626 DOI: 10.1007/s00339-003-2182-9.

(29) Deibel, C.; MacK, D.; Gorenflot, J.; Schöll, A.; Krause, S.; Reinert, F.; Rauh, D.; Dyakonov, V. Energetics of Excited States in the Conjugated Polymer poly(3-Hexylthiophene). *Phys. Rev. B - Condens. Matter Mater. Phys.* **2010**, *81* (8), 1–5 DOI: 10.1103/PhysRevB.81.085202.

(30) Егоров, В. В.; Алфимов, М. В. Теория J-Полосы: От Экситона Френкеля К Переносу Заряда. *Uspekhi Fiz. Nauk* **2007**, *177* (10), 1033 DOI: 10.3367/UFNr.0177.200710a.1033.

(31) Spano, F. C.; Clark, J.; Silva, C.; Friend, R. H. Determining Exciton Coherence from the Photoluminescence Spectral Line Shape in poly(3-Hexylthiophene) Thin Films. *J. Chem. Phys.* **2009**, *130* (7) DOI: 10.1063/1.3076079.

(32) Meskers, S. C. J.; Hübner, J.; Oestreich, M.; Bässler, H. Dispersive Relaxation Dynamics of Photoexcitations in a Polyfluorene Film Involving Energy Transfer: Experiment and Monte Carlo Simulations. *J. Phys. Chem. B* **2001**, *105* (38), 9139–9149 DOI: 10.1021/jp0113331.

(33) Kersting, R.; Mollay, B.; Rusch, M.; Wenisch, J.; Leising, G.; Kauffmann, H. F. Femtosecond Site-Selective Probing of Energy Relaxing Excitons in Poly(phenylenevinylene): Luminescence Dynamics and Lifetime Spectra. *J. Chem. Phys.* **1997**, *106* (7), 2850 DOI: 10.1063/1.473094.

(34) Grage, M. M. L.; Pullerits, T.; Ruseckas, A.; Theander, M.; Inganäs, O.; Sundström, V.

Conformational Disorder of a Substituted Polythiophene in Solution Revealed by Excitation Transfer. *Chem. Phys. Lett.* **2001**, *339* (1–2), 96–102 DOI: 10.1016/S0009-2614(01)00305-0.

(35) Grage, M. M. L.; Wood, P. W.; Ruseckas, A.; Pullerits, T.; Mitchell, W.; Burn, P. L.; Samuel, I. D. W.; Sundström, V. Conformational Disorder and Energy Migration in MEH-PPV with Partially Broken Conjugation. *J. Chem. Phys.* **2003**, *118* (16), 7644–7650 DOI: 10.1063/1.1562190.

(36) Grage, M.; Zaushitsyn, Y.; Yartsev, A.; Chachisvilis, M.; Sundström, V.; Pullerits, T. Ultrafast Excitation Transfer and Trapping in a Thin Polymer Film. *Phys. Rev. B* **2003**, *67* (20), 205207 DOI: 10.1103/PhysRevB.67.205207.

(37) Westenhoff, S.; Daniel, C.; Friend, R. H.; Silva, C.; Sundström, V.; Yartsev, A. Exciton Migration in a Polythiophene: Probing the Spatial and Energy Domain by Line-Dipole Förster-Type Energy Transfer. *J. Chem. Phys.* **2005**, *122* (9) DOI: 10.1063/1.1855292.

(38) Watkins, P. K.; Walker, A. B.; Verschoor, G. L. B. Dynamical Monte Carlo Modelling of Organic Solar Cells : The Dependence of Internal Quantum Efficiency on Morphology Dynamical Monte Carlo Modelling of Organic Solar Cells : The Dependence of Internal Quantum Efficiency on Morphology. *Nano Lett.* **2005**, *5* (9), 1814–1818 DOI: 10.1021/nl051098o.

(39) Cnops, K.; Rand, B. P.; Cheyns, D.; Verreet, B.; Empl, M. a; Heremans, P. 8.4% Efficient Fullerene-Free Organic Solar Cells Exploiting Long-Range Exciton Energy Transfer. *Nat. Commun.* **2014**, *5*, 3406 DOI: 10.1038/ncomms4406.

(40) Burlakov, V. M.; Kawata, K.; Assender, H. E.; Briggs, G. A. D.; Ruseckas, A.; Samuel, I. D. W. Discrete Hopping Model of Exciton Transport in Disordered Media. *Phys. Rev. B - Condens. Matter Mater. Phys.* **2005**, *72* (7), 1–5 DOI: 10.1103/PhysRevB.72.075206.

(41) Lunt, R. R.; Giebink, N. C.; Belak, A. A.; Benziger, J. B.; Forrest, S. R. Exciton Diffusion Lengths of Organic Semiconductor Thin Films Measured by Spectrally Resolved Photoluminescence Quenching. *J. Appl. Phys.* **2009**, *105* (5) DOI: 10.1063/1.3079797.

(42) Shao, Y.; Yang, Y. Efficient Organic Heterojunction Photovoltaic Cells Based on Triplet Materials. *Adv. Mater.* **2005**, *17* (23), 2841–2844 DOI: 10.1002/adma.200501297.

(43) Ohkita, H.; Ito, S. Transient Absorption Spectroscopy of Polymer-Based Thin-Film Solar Cells. *Polymer (Guildf).* **2011**, *52* (20), 4397–4417 DOI: 10.1016/j.polymer.2011.06.061.

(44) Xu, G.; Lu, N.; Wang, W.; Gao, N.; Ji, Z.; Li, L.; Liu, M. Universal Description of Exciton Diffusion Length in Organic Photovoltaic Cell. *Org. Electron.* **2015**, *23*, 53–56 DOI: 10.1016/j.orgel.2015.04.006.

(45) Toušek, J.; Toušková, J.; Remeš, Z.; Čermák, J.; Kousal, J.; Kindl, D.; Kuřitka, I. Exciton Diffusion Length and Concentration of Holes in MEH-PPV Polymer Using the Surface Voltage and Surface Photovoltage Methods. *Chem. Phys. Lett.* **2012**, *552*, 49–52 DOI: 10.1016/j.cplett.2012.09.052.

(46) Scharber, M. C.; Mühlbacher, D.; Koppe, M.; Denk, P.; Waldauf, C.; Heeger, A. J.; Brabec, C. J. Design Rules for Donors in Bulk-Heterojunction Solar Cells - Towards 10 % Energy-Conversion Efficiency. *Adv. Mater.* **2006**, *18* (6), 789–794 DOI: 10.1002/adma.200501717.

(47) Yao, Y.; Sun, X.; Ding, B.; Li, D.-L.; Hou, X.; Wu, C.-Q. A Combined Theoretical and Experimental Investigation on the Transient Photovoltage in Organic Photovoltaic Cells. *Appl. Phys. Lett.* **2010**, *96* (20), 203306 DOI: 10.1063/1.3431289.

(48) Song, Q. L.; Wu, H. R.; Ding, X. M.; Hou, X. Y.; Li, F. Y.; Zhou, Z. G. Exciton Dissociation at the Indium Tin Oxide-N,N[sup ′]-Bis(naphthalen-1-Yl)-N,N[sup ′]-Bis(phenyl) Benzidine Interface: A Transient Photovoltage Study. *Appl. Phys. Lett.* **2006**, *88* (23), 232101 DOI: 10.1063/1.2209203.

(49) Li, D. L.; Si, W.; Yang, W. C.; Yao, Y.; Hou, X. Y.; Wu, C. Q. Spike in Transient

Photocurrent of Organic Solar Cell: Exciton Dissociation at Interface. *Phys. Lett. Sect. A Gen. At. Solid State Phys.* **2012**, *376* (4), 227–230 DOI: 10.1016/j.physleta.2011.11.055.

(50) Chamberlain, G. A. Organic Solar Cells: A Review. *Sol. Cells* **1983**, *8* (1), 47–83 DOI: 10.1016/0379-6787(83)90039-X.

(51) Yu, G.; Gao, J.; Hummelen, J. C.; Wudl, F.; Heeger, A. J. Polymer Photovoltaic Cells - Enhanced Efficiencies Via a Network of Internal Donor-Acceptor Heterojunctions. *Science (80-.).* **1995**, *270* (5243), 1789–1791 DOI: 10.1126/science.270.5243.1789.

(52) Nicolet, C.; Deribew, D.; Renaud, C.; Fleury, G.; Brochon, C.; Cloutet, E.; Vignau, L.; Wantz, G.; Cramail, H.; Geoghegan, M.; Hadziioannou, G. Optimization of the Bulk Heterojunction Composition for Enhanced Photovoltaic Properties: Correlation between the Molecular Weight of the Semiconducting Polymer and Device Performance. *J. Phys. Chem. B* **2011**, *115* (44), 12717–12727 DOI: 10.1021/jp207669j.

(53) Shin, P.; Kumar, P.; Kumar, A.; Kannappan, S.; Ochiai, S. Effects of Organic Solvents for Composite Active Layer of PCDTBT / PC 71 BM on Characteristics of Organic Solar Cell Devices. *Int. J. photoenergy* **2013**, *2014*, 1–8 DOI: 10.1155/2014/786468.

(54) Kadem, B. Y.; Al-Hashimi, M. K.; Hassan, A. K. The Effect of Solution Processing on the Power Conversion Efficiency of P3HT-Based Organic Solar Cells. *Energy Procedia* **2014**, *50*, 237–245 DOI: 10.1016/j.egypro.2014.06.029.

(55) Tada, K. Optimization of Photovoltaic Device Based on poly(3-hexylthiophene):C 60 Bulk Heterojunction Composites Prepared with Halogen-Free Solvent. *Jpn. J. Appl. Phys.* **2014**, *53* (1S), 01AB01 DOI: 10.7567/JJAP.53.01AB01.

(56) Hoppe, H.; Niggemann, M.; Winder, C.; Kraut, J.; Hiesgen, R.; Hinsch, A.; Meissner, D.; Sariciftci, N. S. Nanoscale Morphology of Conjugated Polymer/fullerene-Based Bulk-Heterojunction Solar Cells. *Adv. Funct. Mater.* **2004**, *14* (10), 1005–1011 DOI: 10.1002/adfm.200305026.

(57) McNeill, C. R.; Halls, J. J. M.; Wilson, R.; Whiting, G. L.; Berkebile, S.; Ramsey, M. G.; Friend, R. H.; Greenham, N. C. Efficient Polythiophene/polyfluorene Copolymer Bulk Heterojunction Photovoltaic Devices: Device Physics and Annealing Effects. *Adv. Funct. Mater.* **2008**, *18* (16), 2309–2321 DOI: 10.1002/adfm.200800182.

(58) Gelinas, S.; Rao, A.; Kumar, A.; Smith, S. L.; Chin, A. W.; Clark, J.; van der Poll, T. S.; Bazan, G. C.; Friend, R. H. Ultrafast Long-Range Charge Separation in Organic Semiconductor Photovoltaic Diodes. *Science (80-.).* **2014**, *343*, 512–516 DOI: 10.1126/science.1246249.

(59) Troisi, A. How Quasi-Free Holes and Electrons Are Generated in Organic Photovoltaic Interfaces. *Faraday Discuss.* **2013**, *163*, 377 DOI: 10.1039/c3fd20142b.

(60) Strobel, T.; Deibel, C.; Dyakonov, V. Role of Polaron Pair Diffusion and Surface Losses in Organic Semiconductor Devices. *Phys. Rev. Lett.* **2010**, *105* (26), 266602 DOI: 10.1103/PhysRevLett.105.266602.

(61) Bredas, J.-L.; Norton, J. E.; Cornil, J.; Coropceanu, V. Molecular Understanding of Organic Solar Cells: The Challenges. *Acc. Chem. Res.* **2009**, *42* (11), 1691–1699 DOI: 10.1021/ar900099h.

(62) Peumans, P.; Forrest, S. R. Separation of Geminate Charge-Pairs at Donor-Acceptor Interfaces in Disordered Solids. *Chem. Phys. Lett.* **2004**, *398* (1–3), 27–31 DOI: 10.1016/j.cplett.2004.09.030.

(63) Offermans, T.; Meskers, S. C. J.; Janssen, R. A. J. Monte-Carlo Simulations of Geminate Electron-Hole Pair Dissociation in a Molecular Heterojunction: A Two-Step Dissociation Mechanism. *Chem. Phys.* **2005**, *308* (1–2), 125–133 DOI: 10.1016/j.chemphys.2004.08.015.

(64) Scheblykin, I. G.; Yartsev, A.; Pullerits, T.; Gulbinas, V.; Sundström, V. Excited State and Charge Photogeneration Dynamics in Conjugated Polymers. *J. Phys. Chem. B* **2007**, *111* (23), 6303–6321 DOI: 10.1021/jp068864f.

(65) Ohkita, H.; Cook, S.; Astuti, Y.; Duffy, W.; Tierney, S.; Zhang, W.; Heeney, M.; McCulloch, I.; Nelson, J.; Bradley, D. D. C.; Durrant, J. R. Charge Carrier Formation

in Polythiophene/fullerene Blend Films Studied by Transient Absorption Spectroscopy. *J. Am. Chem. Soc.* **2008**, *130* (10), 3030–3042 DOI: 10.1021/ja076568q.

(66) Gélinas, S.; Rao, A.; Kumar, A.; Smith, S. L.; Chin, A. W.; Clark, J.; van der Poll, T. S.; Bazan, G. C.; Friend, R. H. Ultrafast Long-Range Charge Separation in Organic Semiconductor Photovoltaic Diodes. *Science* **2014**, *343* (6170), 512–516 DOI: 10.1126/science.1246249.

(67) Clarke, T. M.; Durrant, J. R. Charge Photogeneration in Organic Solar Cells. *Chem. Rev.* **2010**, *110* (11), 6736–6767 DOI: 10.1021/cr900271s.

(68) Bässler, H. Charge Transport in Disordered Organic Photoconductors a Monte Carlo Simulation Study. *Phys. Status Solidi B* **1993**, *175* (1), 15–56 DOI: 10.1002/pssb.2221750102.

(69) Arkhipov, V.; Emelianova, E.; Adriaenssens, G. Effective Transport Energy versus the Energy of Most Probable Jumps in Disordered Hopping Systems. *Phys. Rev. B* **2001**, *64*, 125125 DOI: 10.1103/PhysRevB.64.125125.

(70) Limpinsel, M.; Wagenpfahl, A.; Mingebach, M.; Deibel, C.; Dyakonov, V. Photocurrent in Bulk Heterojunction Solar Cells. *Phys. Rev. B - Condens. Matter Mater. Phys.* **2010**, *81* (8), 1–6 DOI: 10.1103/PhysRevB.81.085203.

(71) Wojcik, M.; Tachiya, M. Accuracies of the Empirical Theories of the Escape Probability Based on Eigen Model and Braun Model Compared with the Exact Extension of Onsager Theory. *J. Chem. Phys.* **2009**, *130* (10) DOI: 10.1063/1.3082005.

(72) Veldman, D.; Ipek, O.; Meskers, S. C. J.; Sweelssen, J.; Koetse, M. M.; Veenstra, S. C.; Kroon, J. M.; van Bavel, S. S.; Loos, J.; Janssen, R. a J. Compositional and Electric Field Dependence of the Dissociation of Charge Transfer Excitons in Alternating Polyfluorene Copolymer/fullerene Blends. *J. Am. Chem. Soc.* **2008**, *130* (24), 7721–7735 DOI: 10.1021/ja8012598.

(73) Heeger, A. J. 25th Anniversary Article: Bulk Heterojunction Solar Cells: Understanding the Mechanism of Operation. *Adv. Mater.* **2014**, *26* (1), 10–28 DOI: 10.1002/adma.201304373.

(74) Bakulin, A. A.; Rao, A.; Pavelyev, V. G.; van Loosdrecht, P. H. M.; Pshenichnikov, M. S.; Niedzialek, D.; Cornil, J.; Beljonne, D.; Friend, R. H. The Role of Driving Energy and Delocalized States for Charge Separation in Organic Semiconductors. *Science* **2012**, *335* (6074), 1340–1344 DOI: 10.1126/science.1217745.

(75) Kaake, L. G.; Moses, D.; Heeger, A. J. Coherence and Uncertainty in Nanostructured Organic Photovoltaics. *J. Phys. Chem. Lett.* **2013**, *4* (14), 2264–2268 DOI: 10.1021/jz4010569.

(76) Miller, A.; Abrahams, E. Impurity Conduction at Low Concentrations. *Phys. Rev.* **1960**, *120* (3), 745–755 DOI: 10.1103/PhysRev.120.745.

(77) Koster, L. J. A.; Smits, E. C. P.; Mihailetchi, V. D.; Blom, P. W. M. Device Model for the Operation of Polymer/fullerene Bulk Heterojunction Solar Cells. *Phys. Rev. B - Condens. Matter Mater. Phys.* **2005**, *72* (8), 1–9 DOI: 10.1103/PhysRevB.72.085205.

(78) Garcia-Belmonte, G.; Boix, P. P.; Bisquert, J.; Sessolo, M.; Bolink, H. J. Simultaneous Determination of Carrier Lifetime and Electron Density-of-States in P3HT:PCBM Organic Solar Cells under Illumination by Impedance Spectroscopy. *Sol. Energy Mater. Sol. Cells* **2010**, *94* (2), 366–375 DOI: 10.1016/j.solmat.2009.10.015.

(79) Campbell, a J.; Bradley, D. D. C.; Lidzey, D. G. Space-Charge Limited Conduction with Traps in Poly(phenylene Vinylene) Light Emitting Diodes. *J. Appl. Phys.* **1997**, *82* (1997), 6326–6342 DOI: 10.1063/1.366523.

(80) Pasveer, W. F.; Cottaar, J.; Tanase, C.; Coehoorn, R.; Bobbert, P. A.; Blom, P. W. M.; De Leeuw, M.; Michels, M. A. J. Unified Description of Charge-Carrier Mobilities in Disordered Semiconducting Polymers. *Phys. Rev. Lett.* **2005**, *94* (20), 1–4 DOI: 10.1103/PhysRevLett.94.206601.

(81) Hoofman, R. J. O. M.; deHaas, M. P.; Siebbeles, L. D. a.; Warman, J. M. Highly Mobile Electrons and Holes on Isolated Chains of the Semiconducting Polymer Poly(phenylenevinylene). *Nature* **1998**, *392* (March), 54–56 DOI: 10.1038/32118.

(82) Warman, J. M.; De Haas, M. P.; Anthopoulos, T. D.; De Leeuw, D. M. The Negative Effect of High-Temperature Annealing on Charge-Carrier Lifetimes in Microcrystalline PCBM. *Adv. Mater.* **2006**, *18* (17), 2294–2298 DOI: 10.1002/adma.200600554.

(83) Tuladhar, S. M.; Poplavskyy, D.; Choulis, S. A.; Durrant, J. R.; Bradley, D. D. C.; Nelson, J. Ambipolar Charge Transport in Films of Methanofullerene and Poly(phenylenevinylene)/Methanofullerene Blends. *Adv. Funct. Mater.* **2005**, *15* (7), 1171–1182 DOI: 10.1002/adfm.200400337.

(84) Mozer, A. J.; Sariciftci, N. S.; Pivrikas, A.; Österbacka, R.; Juska, G.; Brassat, L.; Bässler, H. Charge Carrier Mobility in Regioregular poly(3-Hexylthiophene) Probed by Transient Conductivity Techniques: A Comparative Study. *Phys. Rev. B - Condens. Matter Mater. Phys.* **2005**, *71* (3), 1–9 DOI: 10.1103/PhysRevB.71.035214.

(85) Blom, P. W. M.; Tanase, C.; De Leeuw, D. M.; Coehoorn, R. Thickness Scaling of the Space-Charge-Limited Current in Poly (P -Phenylene Vinylene). *Appl. Phys. Lett.* **2005**, *86* (9), 1–3 DOI: 10.1063/1.1868865.

(86) Lorrmann, J.; Badada, B. H.; Inganäs, O.; Dyakonov, V.; Deibel, C. Charge Carrier Extraction by Linearly Increasing Voltage: Analytic Framework and Ambipolar Transients. *J. Appl. Phys.* **2010**, *108* (11) DOI: 10.1063/1.3516392.

(87) Mozer, A. J.; Dennler, G.; Sariciftci, N. S.; Westerling, M.; Pivrikas, A.; Asterbacka, R.; Juska, G. Time-Dependent Mobility and Recombination of the Photoinduced Charge Carriers in Conjugated Polymer/fullerene Bulk Heterojunction Solar Cells. *Phys. Rev. B - Condens. Matter Mater. Phys.* **2005**, *72* (3), 1–10 DOI: 10.1103/PhysRevB.72.035217.

(88) Offermans, T.; Meskers, S. C. J.; Janssen, R. A. J. Time Delayed Collection Field Experiments on Polymer: Fullerene Bulk-Heterojunction Solar Cells. *J. Appl. Phys.* **2006**, *100* (7), 74509 DOI: 10.1063/1.2356783.

(89) Kniepert, J.; Schubert, M.; Blakesley, J. C.; Neher, D. Photogeneration and Recombination in P3HT/PCBM Solar Cells Probed by Time-Delayed Collection Field Experiments. *J. Phys. Chem. Lett.* **2011**, *2* (7), 700–705 DOI: 10.1021/jz200155b.

(90) Mihailetchi, V. D.; Wildeman, J.; Blom, P. W. M. Space-Charge Limited Photocurrent. *Phys. Rev. Lett.* **2005**, *94* (12), 1–4 DOI: 10.1103/PhysRevLett.94.126602.

(91) Mihailetchi, V. D.; Koster, L. J. A.; Hummelen, J. C.; Blom, P. W. M. Photocurrent Generation in Polymer-Fullerene Bulk Heterojunctions. *Phys. Rev. Lett.* **2004**, *93* (21), 19–22 DOI: 10.1103/PhysRevLett.93.216601.

(92) Servaites, J. D.; Ratner, M. A.; Marks, T. J. Organic Solar Cells: A New Look at Traditional Models. *Energy Environ. Sci.* **2011**, *4* (11), 4410–4422 DOI: 10.1039/c1ee01663f.

(93) Cheyns, D.; Poortmans, J.; Heremans, P.; Deibel, C.; Verlaak, S.; Rand, B. P.; Genoe, J. Analytical Model for the Open-Circuit Voltage and Its Associated Resistance in Organic Planar Heterojunction Solar Cells. *Phys. Rev. B - Condens. Matter Mater. Phys.* **2008**, *77* (16), 1–10 DOI: 10.1103/PhysRevB.77.165332.

(94) Devižis, A.; Serbenta, A.; Meerholz, K.; Hertel, D.; Gulbinas, V. Ultrafast Dynamics of Carrier Mobility in a Conjugated Polymer Probed at Molecular and Microscopic Length Scales. *Phys. Rev. Lett.* **2009**, *103* (2), 27404 DOI: 10.1103/PhysRevLett.103.027404.

(95) Bosshard, C.; Knöpfle, G.; Prêtre, P.; Günter, P. Second-Order Polarizabilities of Nitropyridine Derivatives Determined with Electric-Field-Induced Second-Harmonic Generation and a Solvatochromic Method: A Comparative Study. *J. Appl. Phys.* **1992**, *71* (4), 1594–1605 DOI: 10.1063/1.351237.

(96) Moylan, C. R.; Twieg, R. J.; Lee, V. Y.; Swanson, S. a.; Betterton, K. M.; Miller, R. D. Nonlinear Optical Chromophores with Large Hyperpolarizabilities and Enhanced Thermal Stabilities. *J. Am. Chem. Soc.* **1993**, *115* (26), 12599–12600 DOI: 10.1021/ja00079a055.

(97) Kaatz, P.; Donley, E. A.; Shelton, D. P. A Comparison of Molecular Hyperpolarizabilities from Gas and Liquid Phase Measurements. *J Chem Phys* **1998**,

108 (3), 849–856 DOI: 10.1063/1.475448.

(98) Gulino, A.; Fragalà, I. L.; Lupo, F.; Malandrino, G.; Motta, A.; Colombo, A.; Dragonetti, C.; Righetto, S.; Roberto, D.; Ugo, R.; Demartin, F.; Ledoux-Rak, I.; Singh, A. Fascinating Role of the Number of F Electrons in Dipolar and Octupolar Contributions to Quadratic Hyperpolarizability of Trinuclear Lanthanides-Biscopper Schiff Base Complexes. *Inorg. Chem.* **2013**, *52* (13), 7550–7556 DOI: 10.1021/ic400558b.

(99) Asselberghs, I.; Pérez-Moreno, J.; Clays, K. Characterization Techniques of Nonlinear Optical Materials. In *Non-Linear Optical Properties of Matter*; Springer Netherlands: Dordrecht, 2006; pp 419–459.

(100) Schauer, F. Space-Charge-Limited Currents for Organic Solar Cells Optimisation. *Sol. Energy Mater. Sol. Cells* **2005**, *87* (1–4), 235–250 DOI: 10.1016/j.solmat.2004.07.020.

(101) Koster, L. J. A.; Mihailetchi, V. D.; Xie, H.; Blom, P. W. M. Origin of the Light Intensity Dependence of the Short-Circuit Current of Polymer/fullerene Solar Cells. *Appl. Phys. Lett.* **2005**, *87* (20), 1–3 DOI: 10.1063/1.2130396.

(102) Di Nuzzo, D.; Van Reenen, S.; Janssen, R. A. J.; Kemerink, M.; Meskers, S. C. J. Evidence for Space-Charge-Limited Conduction in Organic Photovoltaic Cells at Open-Circuit Conditions. *Phys. Rev. B - Condens. Matter Mater. Phys.* **2013**, *87* (8), 1–11 DOI: 10.1103/PhysRevB.87.085207.

(103) Lakhwani, G.; Rao, A.; Friend, R. H. Bimolecular Recombination in Organic Photovoltaics. *Annu. Rev. Phys. Chem.* **2014**, *65* (December 2013), 557–581 DOI: 10.1146/annurev-physchem-040513-103615.

(104) Gulbinas, V.; Zaushitsyn, Y.; Sundström, V.; Hertel, D.; Bässler, H.; Yartsev, A. Dynamics of the Electric Field-Assisted Charge Carrier Photogeneration in Ladder-Type Poly(Para-Phenylene) at a Low Excitation Intensity. *Phys. Rev. Lett.* **2002**, *89* (10), 107401 DOI: 10.1103/PhysRevLett.89.107401.

(105) Abramavicius, V.; Abramavicius, D. Excitation Transfer Pathways in Excitonic Aggregates Revealed by the Stochastic Schr??dinger Equation. *J. Chem. Phys.* **2014**, *140* (6) DOI: 10.1063/1.4863968.

(106) Vandewal, K.; Ma, Z.; Bergqvist, J.; Tang, Z.; Wang, E.; Henriksson, P.; Tvingstedt, K.; Andersson, M. R.; Zhang, F.; Inganäs, O. Quantification of Quantum Efficiency and Energy Losses in Low Bandgap Polymer:Fullerene Solar Cells with High Open-Circuit Voltage. *Adv. Funct. Mater.* **2012**, *22* (16), 3480–3490 DOI: 10.1002/adfm.201200608.

(107) Tang, Z.; Andersson, L. M.; George, Z.; Vandewal, K.; Tvingstedt, K.; Heriksson, P.; Kroon, R.; Andersson, M. R.; Inganäs, O. Interlayer for Modified Cathode in Highly Efficient Inverted ITO-Free Organic Solar Cells. *Adv. Mater.* **2012**, *24* (4), 554–558 DOI: 10.1002/adma.201104579.

(108) Wang, E.; Hou, L.; Wang, Z.; Hellström, S.; Zhang, F.; Inganäs, O.; Andersson, M. R. An Easily Synthesized Blue Polymer for High-Performance Polymer Solar Cells. *Adv. Mater.* **2010**, *22* (46), 5240–5244 DOI: 10.1002/adma.201002225.

(109) Tang, Z.; George, Z.; Ma, Z.; Bergqvist, J.; Tvingstedt, K.; Vandewal, K.; Wang, E.; Andersson, L. M.; Andersson, M. R.; Zhang, F.; Inganäs, O. Semi-Transparent Tandem Organic Solar Cells with 90% Internal Quantum Efficiency. *Adv. Energy Mater.* **2012**, *2* (12), 1467–1476 DOI: 10.1002/aenm.201200204.

(110) Xia, Y.; Musumeci, C.; Bergqvist, J.; Ma, W.; Gao, F.; Tang, Z.; Bai, S.; Jin, Y.; Zhu, C.; Kroon, R.; Wang, C.; Andersson, M. R.; Hou, L.; Inganäs, O.; Wang, E. Inverted All-Polymer Solar Cells Based on a Quinoxaline–thiophene/naphthalene-Diimide Polymer Blend Improved by Annealing. *J. Mater. Chem. A* **2016**, *4* (10), 3835–3843 DOI: 10.1039/C6TA00531D.

(111) Sariciftci, N. S.; Smilowitz, L.; Heeger, A. J.; Wudl, F. Photoinduced Electron Transfer from a Conducting Polymer to Buckminsterfullerene. *Science* **1992**, *258* (5087), 1474–1476 DOI: 10.1126/science.258.5087.1474.

(112) Deibel, C.; Strobel, T.; Dyakonov, V. Origin of the Efficient Polaron-Pair Dissociation in Polymer-Fullerene Blends. *Phys. Rev. Lett.* **2009**, *103* (3), 1–4 DOI: 10.1103/PhysRevLett.103.036402.

(113) Grancini, G.; Maiuri, M.; Fazzi, D.; Petrozza, a.; Egelhaaf, H.-J.; Brida, D.; Cerullo, G.; Lanzani, G.; Binda, M.; Criante, L.; Perissinotto, S. Hot Exciton Dissociation in Polymer Solar Cells. *Nat. Mater.* **2012**, *11* (12), 1–5 DOI: 10.1038/nmat3502.

(114) Jailaubekov, A. E.; Willard, A. P.; Tritsch, J. R.; Chan, W.-L.; Sai, N.; Gearba, R.; Kaake, L. G.; Williams, K. J.; Leung, K.; Rossky, P. J.; Zhu, X.-Y. Hot Charge-Transfer Excitons Set the Time Limit for Charge Separation at Donor/acceptor Interfaces in Organic Photovoltaics. *Nat. Mater.* **2013**, *11* (12), 66–73 DOI: 10.1038/nmat3500.

(115) Lee, M. H.; Aragó, J.; Troisi, A. Charge Dynamics in Organic Photovoltaic Materials: Interplay between Quantum Diffusion and Quantum Relaxation. *J. Phys. Chem. C* **2015**, *119* (27), 14989–14998 DOI: 10.1021/acs.jpcc.5b03989.

(116) Vithanage, D. A.; Devižis, a; Abramavičius, V.; Infahsaeng, Y.; Abramavičius, D.; Mackenzie, R. C. I.; Keivanidis, P. E.; Yartsev, a; Hertel, D.; Nelson, J.; Sundström, V.; Gulbinas, V. Visualizing Charge Separation in Bulk Heterojunction Organic Solar Cells. *Nat. Commun.* **2013**, *4*, 2334 DOI: 10.1038/ncomms3334.

(117) Murthy, D. H. K.; Melianas, A.; Tang, Z.; Juška, G.; Arlauskas, K.; Zhang, F.; Siebbeles, L. D. a.; Inganäs, O.; Savenije, T. J. Origin of Reduced Bimolecular Recombination in Blends of Conjugated Polymers and Fullerenes. *Adv. Funct. Mater.* **2013**, n/a-n/a DOI: 10.1002/adfm.201203852.

(118) Cabanillas-Gonzalez, J.; Virgili, T.; Gambetta, A.; Lanzani, G.; Anthopoulos, T. D.; de Leeuw, D. M. Photoinduced Transient Stark Spectroscopy in Organic Semiconductors: A Method for Charge Mobility Determination in the Picosecond Regime. *Phys. Rev. Lett.* **2006**, *96* (10), 106601 DOI: 10.1103/PhysRevLett.96.106601.

(119) Devižis, A.; Hertel, D.; Meerholz, K.; Gulbinas, V.; Moser, J.-E. Time-Independent, High Electron Mobility in Thin PC61BM Films: Relevance to Organic Photovoltaics. *Org. Electron.* **2014**, *15*, 3729–3734 DOI: 10.1016/j.orgel.2014.10.028.

(120) Ho, C.-C.; Chen, C.-A.; Chang, C.-Y.; Darling, S. B.; Su, W.-F. Isoindigo-Based Copolymers for Polymer Solar Cells with Efficiency over 7%. *J. Mater. Chem. A* **2014**, *2* (21), 8026 DOI: 10.1039/c4ta01083c.

(121) Mihailetchi, V. D.; van Duren, J. K. J.; Blom, P. W. M.; Hummelen, J. C.; Janssen, R. a. J.; Kroon, J. M.; Rispens, M. T.; Verhees, W. J. H.; Wienk, M. M. Electron Transport in a Methanofullerene. *Adv. Funct. Mater.* **2003**, *13* (1), 43–46 DOI: 10.1002/adfm.200390004.

(122) Vandewal, K.; Albrecht, S.; Hoke, E. T.; Graham, K. R.; Widmer, J.; Douglas, J. D.; Schubert, M.; Mateker, W. R.; Bloking, J. T.; Burkhard, G. F.; Sellinger, A.; Fréchet, J. M. J.; Amassian, A.; Riede, M. K.; McGehee, M. D.; Neher, D.; Salleo, A. Efficient Charge Generation by Relaxed Charge-Transfer States at Organic Interfaces. *Nat. Mater.* **2014**, *13* (1), 63–68 DOI: 10.1038/nmat3807.

(123) Van Eersel, H.; Janssen, R. A. J.; Kemerink, M. Mechanism for Efficient Photoinduced Charge Separation at Disordered Organic Heterointerfaces. *Adv. Funct. Mater.* **2012**, *22* (13), 2700–2708 DOI: 10.1002/adfm.201200249.

(124) Pivrikas, A.; Sariciftci, N. S.; Juška, G.; Österbacka, R. A Review of Charge Transport and Recombination in Polymer/fullerene Organic Solar Cells. *Prog. Photovoltaics Res. Appl.* **2007**, *15* (8), 677–696 DOI: 10.1002/pip.791.

(125) Bartelt, J. A.; Beiley, Z. M.; Hoke, E. T.; Mateker, W. R.; Douglas, J. D.; Collins, B. a.; Tumbleston, J. R.; Graham, K. R.; Amassian, A.; Ade, H.; Fréchet, J. M. J.; Toney, M. F.; McGehee, M. D. The Importance of Fullerene Percolation in the Mixed Regions of Polymer-Fullerene Bulk Heterojunction Solar Cells. *Adv. Energy Mater.* **2013**, *3* (3), 364–374 DOI: 10.1002/aenm.201200637.

(126) Geiser, A.; Fan, B.; Benmansour, H.; Castro, F.; Heier, J.; Keller, B.; Mayerhofer, K. E.; Nüesch, F.; Hany, R. Poly(3-hexylthiophene)/C60 Heterojunction Solar Cells: Implication of Morphology on Performance and Ambipolar Charge Collection. *Sol. Energy Mater. Sol. Cells* **2008**, *92* (4), 464–473 DOI: 10.1016/j.solmat.2007.11.001.

(127) Howard, I. A.; Mauer, R.; Meister, M.; Laquai, F. Effect of Morphology on Ultrafast Free Carrier Generation in Polythiophene:fullerene Organic Solar Cells. *J. Am. Chem.*

Soc. **2010**, *132* (42), 14866–14876 DOI: 10.1021/ja105260d.

(128) Zhang, F.; Jespersen, K. G.; Björström, C.; Svensson, M.; Andersson, M. R.; Sundström, V.; Magnusson, K.; Moons, E.; Yartsev, a.; Inganäs, O. Influence of Solvent Mixing on the Morphology and Performance of Solar Cells Based on Polyfluorene Copolymer/Fullerene Blends. *Adv. Funct. Mater.* **2006**, *16* (5), 667–674 DOI: 10.1002/adfm.200500339.

(129) Coropceanu, V.; Cornil, J.; Silva, D.; A, D.; Olivier, Y.; Silbey, R.; Bredas, J. L.; da Silva Filho, D. A.; Brédas, J.-L. J.-L.; Olivier, Y.; Silbey, R.; Brédas, J.-L. J.-L. Charge Transport in Organic Semiconductors. *Chem. Rev.* **2007**, *107* (4), 926–952 DOI: 10.1007/128_2011_218.

(130) Andersson, L. M.; Inganäs, O. Acceptor Influence on Hole Mobility in Fullerene Blends with Alternating Copolymers of Fluorene. *Appl. Phys. Lett.* **2006**, *88* (8), 82103 DOI: 10.1063/1.2177663.

(131) Yang, K.; Wang, Y.; Jain, A.; Samulson, L.; Kumar, J. Determination of Electron and Hole Mobility of Regioregular Poly(3-hexylthiophene) by the Time of Flight Method. *J. Macromol. Sci. Part A* **2007**, *44* (12), 1261–1264 DOI: 10.1080/10601320701606711.

(132) Choulis, S. A.; Kim, Y.; Nelson, J.; Bradley, D. D. C.; Giles, M.; Shkunov, M.; McCulloch, I. High Ambipolar and Balanced Carrier Mobility in Regioregular poly(3-Hexylthiophene). *Appl. Phys. Lett.* **2004**, *85* (17), 3890–3892 DOI: 10.1063/1.1805175.

(133) Anthopoulos, T. D.; Tanase, C.; Setayesh, S.; Meijer, E. J.; Hummelen, J. C.; Blom, P. W. M.; de Leeuw, D. M. Ambipolar Organic Field-Effect Transistors Based on a Solution-Processed Methanofullerene. *Adv. Mater.* **2004**, *16* (23–24), 2174–2179 DOI: 10.1002/adma.200400309.

(134) Waldauf, C.; Schilinsky, P.; Perisutti, M.; Hauch, J.; Brabec, C. J. Solution-Processed Organic N-Type Thin-Film Transistors. *Adv. Mater.* **2003**, *15* (24), 2084–2088 DOI: 10.1002/adma.200305623.

(135) Meijer, E. J.; de Leeuw, D. M.; Setayesh, S.; van Veenendaal, E.; Huisman, B. H.; Blom, P. W. M.; Hummelen, J. C.; Scherf, U.; Kadam, J.; Klapwijk, T. M. Solution-Processed Ambipolar Organic Field-Effect Transistors and Inverters. *Nat. Mater.* **2003**, *2* (10), 678–682 DOI: 10.1038/nmat978.

(136) Singh, T. B.; Marjanović, N.; Stadler, P.; Auinger, M.; Matt, G. J.; Günes, S.; Sariciftci, N. S.; Schwödiauer, R.; Bauer, S. Fabrication and Characterization of Solution-Processed Methanofullerene-Based Organic Field-Effect Transistors. *J. Appl. Phys.* **2005**, *97* (8), 83714 DOI: 10.1063/1.1895466.

(137) Arkhipov, V.; Bässler, H.; Emelyanova, E.; Hertel, D.; Gulbinas, V.; Rothberg, L. Exciton Dissociation in Conjugated Polymers. *Macromol. Symp.* **2004**, *212* (1), 13–24 DOI: 10.1002/masy.200450802.

(138) Shuttle, C.; Hamilton, R.; O'Regan, B. C.; Nelson, J.; Durrant, J. R. Charge-Density-Based Analysis of the Current–voltage Response of Polythiophene/fullerene Photovoltaic Devices. *Proc. Natl. Acad. Sci. U. S. A.* **2010**, *107* (38), 16448–16452 DOI: 10.1073/pnas.1004363107/-/DCSupplemental.www.pnas.org/cgi/doi/10.1073/pnas.1004363107.

(139) De, S.; Pascher, T.; Maiti, M.; Jespersen, K. G.; Kesti, T.; Zhang, F.; Inganäs, O.; Yartsev, A.; Sundström, V. Geminate Charge Recombination in Alternating Polyfluorene Copolymer/fullerene Blends. *J. Am. Chem. Soc.* **2007**, *129* (27), 8466–8472 DOI: 10.1021/ja068909q.

(140) De, S.; Kesti, T.; Maiti, M.; Zhang, F.; Inganäs, O.; Yartsev, A.; Pascher, T.; Sundström, V. Exciton Dynamics in Alternating Polyfluorene/fullerene Blends. *Chem. Phys.* **2008**, *350* (1–3), 14–22 DOI: 10.1016/j.chemphys.2007.11.018.

(141) Schubert, M.; Preis, E.; Blakesley, J.; Pingel, P.; Scherf, U.; Neher, D. Mobility Relaxation and Electron Trapping in a Donor/acceptor Copolymer. *Phys. Rev. B* **2013**, *87* (2), 24203 DOI: 10.1103/PhysRevB.87.024203.

(142) Ponseca, C. S.; Nemec, H.; Vukmirovic, N.; Fusco, S.; Wang, E.; Andersson, M. R.; Chabera, P.; Yartsev, A.; Sundström, V. Electron and Hole Contributions to the

Terahertz Photoconductivity of a Conjugated Polymer: Fullerene Blend Identified. *J. Phys. Chem. Lett.* **2012**, *3*, 2442–2446.

(143) Ponseca, C. S.; Yartsev, A.; Wang, E.; Andersson, M. R.; Vithanage, D.; Sundström, V. Ultrafast Terahertz Photoconductivity of Bulk Heterojunction Materials Reveals High Carrier Mobility up to Nanosecond Time Scale. *J. Am. Chem. Soc.* **2012**, *134* (29), 11836–11839 DOI: 10.1021/ja301757y.

(144) Esenturk, O.; Melinger, J. S.; Heilweil, E. J. Terahertz Mobility Measurements on Poly-3-Hexylthiophene Films: Device Comparison, Molecular Weight, and Film Processing Effects. *J. Appl. Phys.* **2008**, *103* (2), 23102 DOI: 10.1063/1.2828028.

(145) Cunningham, P. D.; Hayden, L. M. Carrier Dynamics Resulting from Above and Below Gap Excitation of P3HT and P3HT/PCBM Investigated by Optical-Pump Terahertz-Probe Spectroscopy †. *J. Phys. Chem. C* **2008**, *112* (21), 7928–7935 DOI: 10.1021/jp711827g.

(146) Vukmirović, N.; Ponseca, C. S.; Němec, H.; Yartsev, A.; Sundström, V. Insights into the Charge Carrier Terahertz Mobility in Polyfluorenes from Large-Scale Atomistic Simulations and Time-Resolved Terahertz Spectroscopy. *J. Phys. Chem. C* **2012**, *116* (37), 19665–19672 DOI: 10.1021/jp3055262.

(147) Jones, M. L.; Chakrabarti, B.; Groves, C. Monte Carlo Simulation of Geminate Pair Recombination Dynamics in Organic Photovoltaic Devices: Multi-Exponential, Field-Dependent Kinetics and Its Interpretation. *J. Phys. Chem. C* **2014**, *118* (1), 85–91 DOI: 10.1021/jp408063f.

(148) Pal, S. K.; Kesti, T.; Maiti, M.; Zhang, F.; Inganäs, O.; Hellström, S.; Andersson, M. R.; Oswald, F.; Langa, F.; Osterman, T.; Pascher, T.; Yartsev, A.; Sundström, V. Geminate Charge Recombination in Polymer/fullerene Bulk Heterojunction Films and Implications for Solar Cell Function. *J. Am. Chem. Soc.* **2010**, *132* (35), 12440–12451 DOI: 10.1021/ja104786x.

(149) Vithanage, D. A.; Wang, E.; Wang, Z.; Ma, F.; Inganäs, O.; Andersson, M. R.; Yartsev, A.; Sundström, V.; Pascher, T. Charge Carrier Dynamics of Polymer:Fullerene Blends: From Geminate to Non-Geminate Recombination. *Adv. Energy Mater.* **2014**, 1301706 DOI: 10.1002/aenm.201301706.

(150) van Duren, J. K. J.; Yang, X.; Loos, J.; Bulle-Lieuwma, C. W. T.; Sieval, a. B.; Hummelen, J. C.; Janssen, R. a. J. Relating the Morphology of Poly(p-Phenylene vinylene)/Methanofullerene Blends to Solar-Cell Performance. *Adv. Funct. Mater.* **2004**, *14* (5), 425–434 DOI: 10.1002/adfm.200305049.

(151) Andersson, L. M.; Zhang, F.; Inganäs, O. Stoichiometry, Mobility, and Performance in Bulk Heterojunction Solar Cells. *Appl. Phys. Lett.* **2007**, *91* (7), 71108 DOI: 10.1063/1.2771524.

(152) Savenije, T.; Kroeze, J.; Wienk, M.; Kroon, J.; Warman, J. Mobility and Decay Kinetics of Charge Carriers in Photoexcited PCBM/PPV Blends. *Phys. Rev. B* **2004**, *69* (15), 155205 DOI: 10.1103/PhysRevB.69.155205.

(153) Van Der Hofstad, T. G. J.; Di Nuzzo, D.; Van Reenen, S.; Janssen, R. A. J.; Kemerink, M.; Meskers, S. C. J. Carrier Recombination in Polymer Fullerene Solar Cells Probed by Reversible Exchange of Charge between the Active Layer and Electrodes Induced by a Linearly Varying Voltage. *J. Phys. Chem. C* **2013**, *117* (7), 3210–3220 DOI: 10.1021/jp306794j.

(154) Maturová, K.; Van Bavel, S. S.; Wienk, M. M.; Janssen, R. A. J.; Kemerink, M. Morphological Device Model for Organic Bulk Heterojunction Solar Cells. *Nano Lett.* **2009**, *9* (8), 3032–3037 DOI: 10.1021/nl901511a.

(155) Blakesley, J. C.; Neher, D. Relationship between Energetic Disorder and Open-Circuit Voltage in Bulk Heterojunction Organic Solar Cells. *Phys. Rev. B - Condens. Matter Mater. Phys.* **2011**, *84* (7) DOI: 10.1103/PhysRevB.84.075210.

(156) Tress, W.; Leo, K.; Riede, M. Optimum Mobility, Contact Properties, and Open-Circuit Voltage of Organic Solar Cells: A Drift-Diffusion Simulation Study. *Phys. Rev. B - Condens. Matter Mater. Phys.* **2012**, *85* (15), 1–11 DOI: 10.1103/PhysRevB.85.155201.

(157) Koster, L. J. A.; Mihailetchi, V. D.; Ramaker, R.; Blom, P. W. M. Light Intensity Dependence of Open-Circuit Voltage of Polymer:fullerene Solar Cells. *Appl. Phys. Lett.* **2005**, *86* (12), 1–3 DOI: 10.1063/1.1889240.

(158) Maurano, A.; Hamilton, R.; Shuttle, C. G.; Ballantyne, A. M.; Nelson, J.; O'Regan, B.; Zhang, W.; McCulloch, I.; Azimi, H.; Morana, M.; Brabec, C. J.; Durrant, J. R. Recombination Dynamics as a Key Determinant of Open Circuit Voltage in Organic Bulk Heterojunction Solar Cells: A Comparison of Four Different Donor Polymers. *Adv. Mater.* **2010**, *22* (44), 4987–4992 DOI: 10.1002/adma.201002360.

(159) Vandewal, K.; Tvingstedt, K.; Gadisa, A.; Inganäs, O.; Manca, J. V. On the Origin of the Open-Circuit Voltage of Polymer–fullerene Solar Cells. *Nat. Mater.* **2009**, *8* (11), 904–909 DOI: 10.1038/nmat2548.

(160) Giebink, N. C.; Lassiter, B. E.; Wiederrecht, G. P.; Wasielewski, M. R.; Forrest, S. R. Ideal Diode Equation for Organic Heterojunctions. II. the Role of Polaron Pair Recombination. *Phys. Rev. B - Condens. Matter Mater. Phys.* **2010**, *82* (15), 1–12 DOI: 10.1103/PhysRevB.82.155306.

(161) Coehoorn, R.; Pasveer, W. F.; Bobbert, P. A.; Michels, M. A. J. Charge-Carrier Concentration Dependence of the Hopping Mobility in Organic Materials with Gaussian Disorder. *Phys. Rev. B - Condens. Matter Mater. Phys.* **2005**, *72* (15), 1–20 DOI: 10.1103/PhysRevB.72.155206.

(162) Mattias Andersson, L.; Inganäs, O. From Short to Long - Optical and Electrical Transients in Photovoltaic Bulk Heterojunctions of Polyfluorene/fullerenes. *Chem. Phys.* **2009**, *357* (1–3), 120–123 DOI: 10.1016/j.chemphys.2008.11.011.

(163) Andersson, L. M.; Melianas, A.; Infahasaeng, Y.; Tang, Z.; Yartsev, A.; Inganäs, O.; Sundström, V. Unified Study of Recombination in Polymer: Fullerene Solar Cells Using Transient Absorption and Charge-Extraction Measurements. *J. Phys. Chem. Lett.* **2013**, *4* (12), 2069–2072 DOI: 10.1021/jz4009745.

(164) Kern, J.; Schwab, S.; Deibel, C.; Dyakonov, V. Binding Energy of Singlet Excitons and Charge Transfer Complexes in MDMO-PPV: PCBM Solar Cells. *Phys. Status Solidi - Rapid Res. Lett.* **2011**, *5* (10–11), 364–366 DOI: 10.1002/pssr.201105430.

(165) Cottaar, J.; Koster, L. J. A.; Coehoorn, R.; Bobbert, P. A. Scaling Theory for Percolative Charge Transport in Disordered Molecular Semiconductors. *Phys. Rev. Lett.* **2011**, *107* (13), 1–4 DOI: 10.1103/PhysRevLett.107.136601.

(166) Germs, W. C.; Van Der Holst, J. J. M.; Van Mensfoort, S. L. M.; Bobbert, P. A.; Coehoorn, R. Modeling of the Transient Mobility in Disordered Organic Semiconductors with a Gaussian Density of States. *Phys. Rev. B - Condens. Matter Mater. Phys.* **2011**, *84* (16), 1–7 DOI: 10.1103/PhysRevB.84.165210.

(167) Christ, N.; Kettlitz, S. W.; Züfle, S.; Valouch, S.; Lemmer, U. Nanosecond Response of Organic Solar Cells and Photodiodes: Role of Trap States. *Phys. Rev. B - Condens. Matter Mater. Phys.* **2011**, *83* (19), 1–5 DOI: 10.1103/PhysRevB.83.195211.

(168) Kemerink, M.; Kramer, J. M.; Gommans, H. H. P.; Janssen, R. A. J. Temperature-Dependent Built-in Potential in Organic Semiconductor Devices. *Appl. Phys. Lett.* **2006**, *88* (19), 1–4 DOI: 10.1063/1.2205007.

(169) Hwang, Y. J.; Ren, G.; Murari, N. M.; Jenekhe, S. A. N-Type Naphthalene Diimide-Biselenophene Copolymer for All-Polymer Bulk Heterojunction Solar Cells. *Macromolecules* **2012**, *45* (22), 9056–9062 DOI: 10.1021/ma3020239.

(170) Wang, E.; Bergqvist, J.; Vandewal, K.; Ma, Z.; Hou, L.; Lundin, A.; Himmelberger, S.; Salleo, A.; Müller, C.; Inganäs, O.; Zhang, F.; Andersson, M. R. Conformational Disorder Enhances Solubility and Photovoltaic Performance of a Thiophene-Quinoxaline Copolymer. *Adv. Energy Mater.* **2013**, *3* (6), 806–814 DOI: 10.1002/aenm.201201019.

(171) Liang, Y.; Xu, Z.; Xia, J.; Tsai, S. T.; Wu, Y.; Li, G.; Ray, C.; Yu, L. For the Bright Future-Bulk Heterojunction Polymer Solar Cells with Power Conversion Efficiency of 7.4%. *Adv. Mater.* **2010**, *22*, 1–4 DOI: 10.1002/adma.200903528.

(172) He, Z.; Zhong, C.; Su, S.; Xu, M.; Wu, H.; Cao, Y. Enhanced Power-Conversion

Efficiency in Polymer Solar Cells Using an Inverted Device Structure. *Nat. Photonics* **2012**, *6* (9), 593–597 DOI: 10.1038/nphoton.2012.190.

(173) Yao, Y.; Hou, J.; Xu, Z.; Li, G.; Yang, Y. Effects of Solvent Mixtures on the Nanoscale Phase Separation in Polymer Solar Cells. *Adv. Funct. Mater.* **2008**, *18* (12), 1783–1789 DOI: 10.1002/adfm.200701459.

(174) Lee, J. K.; Ma, W. L.; Brabec, C. J.; Yuen, J.; Moon, J. S.; Kim, J. Y.; Lee, K.; Bazan, G. C.; Heeger, A. J. Processing Additives for Improved Efficiency from Bulk Heterojunction Solar Cells. *J. Am. Chem. Soc.* **2008**, *130* (17), 3619–3623 DOI: 10.1021/ja710079w.

(175) Collins, B. A.; Li, Z.; Tumbleston, J. R.; Gann, E.; McNeill, C. R.; Ade, H. Absolute Measurement of Domain Composition and Nanoscale Size Distribution Explains Performance in PTB7:PC 71 BM Solar Cells. *Adv. Energy Mater.* **2013**, *3* (1), 65–74 DOI: 10.1002/aenm.201200377.

(176) Hammond, M. R.; Kline, R. J.; Herzing, A. a; Richter, L. J.; Germack, D. S.; Ro, H.; Soles, C. L.; Fischer, D. a; Xu, T.; Yu, L.; Toney, M. F.; Delongchamp, D. M. Molecular Order in High-Efficiency Polymer / Fullerene Bulk Heterojunction Solar Cells. *ACS Nano* **2011**, *5* (10), 8248–8257 DOI: 10.1021/nn202951e.

(177) Hedley, G. J.; Ward, A. J.; Alekseev, A.; Howells, C. T.; Martins, E. R.; Serrano, L. a; Cooke, G.; Ruseckas, A.; Samuel, I. D. W. Determining the Optimum Morphology in High-Performance Polymer-Fullerene Organic Photovoltaic Cells. *Nat. Commun.* **2013**, *4*, 2867 DOI: 10.1038/ncomms3867.

(178) Lou, S. J.; Szarko, J. M.; Xu, T.; Yu, L.; Marks, T. J.; Chen, L. X. Effects of Additives on the Morphology of Solution Phase Aggregates Formed by Active Layer Components of High-Efficiency Organic Solar Cells. *J. Am. Chem. Soc.* **2011**, *133* (51), 20661–20663 DOI: 10.1021/ja2085564.

(179) Yao, E.-P.; Chen, C.-C.; Gao, J.; Liu, Y.; Chen, Q.; Cai, M.; Hsu, W.-C.; Hong, Z.; Li, G.; Yang, Y. The Study of Solvent Additive Effects in Efficient Polymer Photovoltaics via Impedance Spectroscopy. *Sol. Energy Mater. Sol. Cells* **2014**, *130*, 20–26 DOI: 10.1016/j.solmat.2014.05.049.

(180) Wang, Z.; Zhang, F.; Li, L.; An, Q.; Wang, J.; Zhang, J. The Underlying Reason of DIO Additive on the Improvement Polymer Solar Cells Performance. *Appl. Surf. Sci.* **2014**, *305*, 221–226 DOI: 10.1016/j.apsusc.2014.03.041.

(181) Chang, S.-Y.; Liao, H.-C.; Shao, Y.-T.; Sung, Y.-M.; Hsu, S.-H.; Ho, C.-C.; Su, W.-F.; Chen, Y.-F. Enhancing the Efficiency of Low Bandgap Conducting Polymer Bulk Heterojunction Solar Cells Using P3HT as a Morphology Control Agent. *J. Mater. Chem. A* **2013**, *1*, 2447–2452 DOI: 10.1039/C2TA00990K.

(182) Lane, P. A.; Cunningham, P. D.; Melinger, J. S.; Esenturk, O.; Heilweil, E. J. Hot Photocarrier Dynamics in Organic Solar Cells. *Nat. Commun.* **2015**, *6* (May), 7558 DOI: 10.1038/ncomms8558.

(183) Burkhard, G. F.; Hoke, E. T.; Beiley, Z. M.; Mcgehee, M. D. Free Carrier Generation in Fullerene Acceptors and Its Effect on Polymer Photovoltaics. *J. Phys. Chem. C* **2012**, *116*, 26674–26678 DOI: 10.1021/jp310821f.

(184) Foster, S.; Deledalle, F.; Mitani, A.; Kimura, T.; Kim, K.-B.; Okachi, T.; Kirchartz, T.; Oguma, J.; Miyake, K.; Durrant, J. R.; Doi, S.; Nelson, J. Electron Collection as a Limit to Polymer:PCBM Solar Cell Efficiency: Effect of Blend Microstructure on Carrier Mobility and Device Performance in PTB7:PCBM. *Adv. Energy Mater.* **2014**, *4* (14), 1400311 DOI: 10.1002/aenm.201400311.

(185) Devižis, A.; Meerholz, K.; Hertel, D.; Gulbinas, V. Hierarchical Charge Carrier Motion in Conjugated Polymers. *Chem. Phys. Lett.* **2010**, *498* (4–6), 302–306 DOI: 10.1016/j.cplett.2010.08.071.

(186) Albrecht, S.; Schindler, W.; Kurpiers, J.; Kniepert, J.; Blakesley, J. C.; Dumsch, I.; Allard, S.; Fostiropoulos, K.; Scherf, U.; Neher, D. On the Field Dependence of Free Charge Carrier Generation and Recombination in Blends of PCPDTBT/PC70BM: Influence of Solvent Additives. *J. Phys. Chem. Lett.* **2012**, *3*, 640–645.